NEUTRON SCATTERING STUDIES TO CHARACTERIZE (QUANTUM) MAGNETIC BEHAVIOR IN (ZN)-BARLOWITE MINERALS

A DISSERTATION
SUBMITTED TO THE DEPARTMENT OF PHYSICS
AND THE COMMITTEE ON GRADUATE STUDIES
OF STANFORD UNIVERSITY
IN PARTIAL FULFILLMENT OF THE REQUIREMENTS
FOR THE DEGREE OF
DOCTOR OF PHILOSOPHY

Aaron T. Breidenbach
February 2026

I certify that I have read this dissertation and that, in my opinion, it is fully adequate in scope and quality as a dissertation for the degree of Doctor of Philosophy.

(Young S. Lee) Principal Adviser

I certify that I have read this dissertation and that, in my opinion, it is fully adequate in scope and quality as a dissertation for the degree of Doctor of Philosophy.

(David Goldhaber-Gordon)

I certify that I have read this dissertation and that, in my opinion, it is fully adequate in scope and quality as a dissertation for the degree of Doctor of Philosophy.

(Ian R. Fisher)

Approved for the Stanford University Committee on Graduate Studies

Abstract

The search for a quantum spin liquid (QSL) ground state remains one of the central challenges of condensed matter physics. A QSL is characterized by highly entangled spins on a frustrated lattice that evade magnetic order even as temperature approaches absolute zero. Realizing this exotic state requires both synthetic ingenuity to produce ideal model systems and extensive experimental characterization to rule out alternative ordered ground states. Because of their potential to host fractionalized excitations and topological order, kagome QSLs are also of significant interest for prospective applications in quantum computation.

To date, Herbertsmithite [$Cu_3Zn(OH)_6Cl_2$] has stood as the most promising kagome QSL candidate. However, its full characterization has been hampered by antisite disorder between interlayer Zn^{2+} and Cu^{2+}, complicating the interpretation of low-temperature measurements. The scarcity of viable kagome QSL materials has motivated the search for new compounds with fewer defects and alternative interlayer chemistries. This alone can go a long way to help separate out intrinsic kagome QSL physics from anything impurity related or material specific. In this work, I report the first growth of high-quality single crystals of Zn–Barlowite [$Cu_3Zn(OH)_6FBr$] using a novel hydrothermal technique, overcoming longstanding challenges posed by fluorine reactivity. These crystals enabled the first single-crystal inelastic neutron scattering measurements of Zn–Barlowite, revealing a broad magnetic continuum consistent with fractionalized spinon excitations. Comparative analysis demonstrates striking similarity between the dynamic correlations in Zn–Barlowite and Herbertsmithite, supporting the universality of the kagome QSL state.

In parallel, I present elastic neutron scattering studies on Barlowite II ($Cu_4(OH)_6FBr$), a polymorph with long-range magnetic order below $T_N \approx 6$ K. These measurements elucidate how interlayer coupling and lattice distortions lift frustration, providing a counterpoint to the QSL behavior of Zn–Barlowite. By situating these results alongside systematic comparisons within the Atacamite mineral family, I highlight the critical role of interlayer ions in mediating frustration, magnetic ordering tendencies, and spin-glass behavior in related compounds.

Finally, I reflect on the natural occurrence of Herbertsmithite- and Barlowite-type minerals across the world and specifically in the Atacama Desert of Chile, a landscape imbued with cultural and spiritual significance. Considering these materials not only as laboratory curiosities but also as

geological and cultural entities broadens the scope of inquiry, opening dialogue between condensed matter physics, geology, and indigenous cosmologies. In this way, the thesis not only advances the frontier of QSL physics but also gestures toward a more integrated understanding of matter, consciousness, and the living world.

Acknowledgments

This is a difficult section for me to write. I have been incredibly depressed during my time at Stanford, and finishing my degree was an immense struggle. I want to pay special acknowledgment to those few flickers of light that I was able to find here. Without any exaggeration, these people are just about all that kept me alive during my time at Stanford, and I truly could not have completed my thesis without them.

I would like to first thank Rebecca Smaha. When I was lost and cut adrift during my first year, she took me in and provided me with the closest scientific mentorship I ever received in my time at Stanford. In many ways, I feel like my thesis rides off of the coat-tails of her groundbreaking work in crystal growth and characterization, particularly of the Barlowite series. She is just about as determined and brilliant of a scientist as you will ever meet and an absolute queen of crystallography.

I would also like to thank Wei He. He has always been a very kind and intelligent collaborator, and he is one of the most knowledgeable and detail oriented neutron scatterers that I know. His help towards the end of my PhD has been absolutely vital to getting me across that finish line. I hope that we can continue to work together in my post-graduate work on these very special minerals.

Finally, I would like to thank Young Lee. His hands-off mentorship style allowed me the space to explore and ultimately discover my true calling in interdisciplinary research—bridging physics with the social sciences, both at Stanford and in Chile. I am grateful to have done so while remaining grounded in my roots in condensed matter physics. Young's clarity about which scientific questions are worth pursuing, and the intellectual freedom fostered in his lab, have provided a strong foundation for my continuing work at the intersection of physics and geoscience.

I would also like to thank James Gross. In my postdoctoral work, I will explore some controversial ideas around crystals and consciousness that have caused me to be the recipient of a lot of hatred and controversy at Stanford, especially at the physics department here. During this time, James has been very kind in welcoming me into philosophy and psychology events and allowing me to express my ideas non-judgmentally. I think it is the philosopher in him that helped drive this curiosity and open-mindedness. These events led me to meet people like Robert Harrison, who really helped me out a lot. I'm truly grateful. Without these opportunities and flicker of belief in me, I would have never been able to develop my ideas into the project that it has become. I extend the same

gratitude towards Geoffrey Cohen, who also helped to encourage me during his social psychology class. Without these invitations, my true philosophical ideas might never have flourished here.

In a similar vein, I would like to give my thanks to Robert P. Harrison, for letting me express my philosophical ideas on his show *Entitled Opinions*. I greatly enjoyed having a platform for my voice to be heard, and I can hardly think of a better venue in which to do this. As the reader shall see, I think that this is a very important message for everyone to hear right now in this day and age. He is also a very kind and spiritual soul that understands the counterculture and psychedelics deeply; this is a rare quality here at Stanford, and it has helped me to develop my spiritual ideas into full fruition. From this interview, I am very happy to report that I made many connections that are invaluable to my continued work on Herbertsmithite in Chile.

I also wish to thank my ever-patient digital collaborator, ChatGPT, whose tireless help in organizing references, finding obscure geoscience sources, and tracing the evolution of ideas across disciplines has made this thesis far more coherent than it would otherwise have been—a true oracle librarian of the digital age. I don't know that there's any other entity that could've helped me to start my postdoctoral research in Chile, although I'm glad that humans are seeming to catch up to the speed of my mind now as well :-).

On account of my depression, I was not able to maintain many stable personal relationships during my time at Stanford. I am very hopeful that this will get better when I move on to greener pastures in Chile. Nonetheless, I would like to thank Madison Tetzlaff (and family) for caring for me when I was cut adrift and lost when I first got to Stanford. She is a very special and rare person, with the tender heart and caring love of a nurse, and the meticulous knowledge of a doctor; she is very much what the world needs more of now. She also sparked my first interest into neuroscience and psychology, which I am quickly finding a lot of passion for as well.

Likewise, I would like to thank Sean Littleton. He is the truest friend I had here, and he always helped me out when I was in a rough spot multiple times, especially when I was moving around and soul searching. We've been through a lot together, and helped each other out through the toughest of our times here.

And finally I would like to thank my mother and Father, Lori and Thomas Breidenbach. I would like to thank Mom for all the care packages she sent to me when I was really feeling down. I would like to thank her for helping me wade through endless stacks of miss-billed paperwork from my mental health services. It is support like this that only a mother would give and that I really don't know how I would get done without her. I would also like to thank her for helping me develop my skills as a writer. She would stay up late-nights with me in high school, transferring her skills as an English teacher to me. I'm happy to say that these lessons helped me to create a successful and popular blog, which seems to be having quite the disruptive effect on research at Stanford, particularly in the psychology and psychedelics research departments. I'm confident that the reader will experience the consequences of this mentorship throughout the rest of this thesis.

Finally, my relationship with my father has always been a difficult one. He definitely pushed me too hard in school to the detriment of my mental health. He also pushed me to go to Stanford over Berkeley for graduate school, which in hindsight was a terrible decision for me personally. He has apologized for this though, and we are moving towards a healthier relationship in which he respects the decisions I make as my own person. I forgive him for his past, and I can see he only pushed me so hard in these ways because he loved me and thought it was best for me. He certainly did spend a lot of time with me in my youth to help me learn the sciences and mathematics, which will also be on full display in this thesis.

And who knows, as a newly found spiritual person, I am finding that maybe these six years in hell were meant to be. The project born out of its ashes are just about the most compelling thing in the world to me.

Along this vein, I would like to thank those who are helping me to manifest my dreams of postdoctoral research in Herbertsmithite in Chile.

I'd like to start by giving an extra special thanks to Steve Dobo and Tamra Arp along with their organization The Audacity Lab. They provided me with a generous seed grant which will help me to start doing Anthropology and Geology research related to this thesis in Chile. I've been dreaming about becoming an anthropologist for years now, and I'm so grateful that they helped this dream of mine come true. Many more organizations seem interested in this project as well now, but I'm forever grateful for my first grant, the first true commitment to my project, and I'll never forget it.

I'd also like to thank Anne White. She's been incredibly sweet and kind in letting me into her home and introducing me to many very influential people within the philanthropy and spiritual spaces. I feel so loved and cherished to have someone in my life that so wholeheartedly believes in me and my vision.

With this, I'd also like to thank Alex Mitchel, who also interviewed me. I'm particularly grateful for her interview, because she is a physicist that asked good physics questions while also not shying away from my philosophical views. I've had a rough run of engagement at Stanford, and I was heartened to see that some physicists are willing to engage with the metaphysical as well. I'm also grateful for her awesome presence and style. I was genuinely worried for a fair bit that Stanford would loose a considerable amount of its personality and fashion sense once I left campus, particularly in the physics department. With Alex though, I'm glad to say that this is, in fact, in great hands!

Finally, I'd like to thank the last of (the first wave of) my interviewers, Michael Kokal. It was great to be interviewed by an established animist with a long running podcast, especially as I am just beginning to put all of these thoughts together.

And lastly, I'd like to give a huge, extra special thanks to Vicente Carrasola Vega. I always knew I wanted to come to Chile to study anthropology, but I had so many questions and very little idea as to what I was doing. So, I took to the internet and I told the world about my project. And amazingly, he responded to the call.

He's been a great host in Chile. He's provided me with so much that I simply could not get in any other way. I'm now in contact with many indigenous leaders that will help me with my explorations into the crystals of Herbertsmithite. These are really difficult contacts to make, and I'm really glad that I have them. I'm also grateful for his hosting of me when I arrived in Chile. He's helped me a lot to receive me into the country, and I'm very excited for our impending trip up north. He's also been very patient as I have requested many things of him while I have been desperately scrambling for organization and money in this project. I think that this will get better very soon, and I'm appreciative that he put up with this spell. I'm glad that the future pastures look greener for both of us.

And last but certainly not least, I'd like to thank myself. You did it. You finished your degree. There were so many moments of doubt. So many moments in which you wanted to quit. But you persevered. And you found greatness. There aren't many other people in this world that are nearly as creative, resilient, and brilliant as you, my love. You're awesome. And you're going to change the world.

Contents

List of Tables

List of Figures

Chapter 1

Introduction

1.1 Quantum Spin Liquids and the Kagome Lattice

The search for exotic phases of matter lies at the heart of condensed matter physics. Among these, the quantum spin liquid (QSL) occupies a special place. First proposed by Anderson in 1973 in the context of high-T_c superconductivity, a QSL is a highly entangled quantum state in which local magnetic moments remain disordered down to absolute zero due to strong quantum fluctuations and geometric frustration [3]. Unlike conventional magnets, which typically undergo symmetry-breaking transitions into ordered states, QSLs preserve spin-rotational symmetry but host fractionalized excitations and emergent gauge fields. These features make them both fundamentally intriguing and of potential relevance to topological quantum computation.

The kagome lattice—a two-dimensional network of corner-sharing triangles—provides one of the most promising geometries for realizing a QSL. In the $S = \frac{1}{2}$ Heisenberg model on the kagome lattice, competing interactions prevent any classical Néel ordering pattern from stabilizing, leaving the ground state highly degenerate. Extensive numerical studies, including density matrix renormalization group (DMRG) and tensor network approaches, suggest that the kagome Heisenberg antiferromagnet realizes either a gapped Z_2 spin liquid or a closely related gapless phase [4]. Experimental realization of such a state requires materials with minimal structural distortions, weak interlayer coupling, and magnetic ions confined to the kagome planes.

1.2 From Herbertsmithite to Zn–Barlowite

The mineral Herbertsmithite [$Cu_3Zn(OH)_6Cl_2$] has emerged over the past two decades as the canonical kagome QSL candidate. Neutron scattering experiments have revealed a broad continuum of magnetic excitations consistent with spin fractionalization, but interpretation remains complicated by antisite disorder: some fraction of Zn^{2+} ions intended for the interlayer site occupy kagome sites,

while Cu^{2+} defects reside between the layers [2, 5]. This disorder complicates precise determination of the intrinsic ground state.

The discovery of Barlowite [$Cu_4(OH)_6FBr$] opened a new path toward realizing an ideal kagome QSL. By substituting interlayer Cu^{2+} with non-magnetic Zn^{2+}, one can suppress interlayer coupling and push the system toward the QSL regime. However, the synthesis of large, high-quality single crystals of Zn–Barlowite has long been hindered by the chemical reactivity of fluorine. In this work, I report a novel hydrothermal growth technique that overcomes these challenges, enabling the first millimeter-scale single crystals of Zn–Barlowite. These crystals allow for inelastic neutron scattering measurements of unprecedented resolution, providing new insights into the universality of the kagome QSL state [6].

1.3 Barlowite II and the Role of Interlayer Coupling

Alongside Zn–Barlowite, this thesis also examines Barlowite II, a polymorph with subtly different structural ordering that stabilizes long-range antiferromagnetic order below $T_N \approx 6$ K. Elastic neutron scattering measurements reveal how its interlayer ions and distortions conspire to lift frustration and select an ordered state. Comparing Barlowite II to Zn–Barlowite and Herbertsmithite highlights the delicate balance between exchange, anisotropy, and Zeeman terms that determines whether a kagome system hosts a QSL or an ordered magnet. Extending this comparison across the broader Atacamite family further illuminates the role of interlayer cations in tuning frustration, with substitutions leading to diverse behaviors including spin-glassiness.

1.4 From Laboratory to Landscape

Although these materials have been synthesized and studied in the laboratory, they are not purely human inventions. Herbertsmithite and related minerals occur naturally in copper-rich deposits such as the Atacama Desert in northern Chile, one of the oldest and driest landscapes on Earth. For millennia, this desert has been a lived and sacred space for the Atacameño people, who have regarded its mountains, rivers, and stars as conscious entities. The presence of naturally occurring kagome QSL candidates in such a cultural landscape invites reflection on the boundaries between physics, geology, and cosmology. What does it mean that materials capable of hosting some of the most exotic quantum states of matter also exist as natural crystals, formed slowly in the Earth's crust and embedded in indigenous worldviews of consciousness and spirit? In the last chapter, I comment on how natural crystals might guide experiments which make the quantum computers of the future.

1.5 Neutron Scattering Pedagogy for Exotic Magnetic Materials

Neutron scattering provides one of the most direct and quantitative probes of magnetic correlations in quantum materials. Because the neutron carries both spin and momentum, it can exchange angular momentum and energy with the magnetic moments of a sample, allowing the full space–time structure of spin correlations to be measured. Inelastic neutron scattering (INS), in particular, offers a unique window into the dynamics of systems that evade classical long-range order—such as quantum spin liquids (QSLs)—by measuring the spectrum of magnetic excitations as a function of momentum transfer $\mathbf{Q}$ and energy transfer $\hbar\omega$.

In contrast to conventional magnets, which exhibit sharp magnon modes associated with symmetry-broken order, QSLs retain strong quantum fluctuations down to the lowest temperatures. These fluctuations destroy static order, leading instead to a continuum of fractionalized spin excitations in $S(\mathbf{Q},\omega)$, the dynamic spin structure factor. Since these excitations are inherently dynamic, techniques sensitive to static magnetism—such as neutron diffraction or muon spin rotation—can only partially characterize the ground state. INS, by contrast, directly captures the dynamical fingerprints of quantum entanglement and thus serves as the most essential experimental probe for candidate QSL materials.

Among the suite of modern neutron instruments, the Cold Neutron Chopper Spectrometer (CNCS) at Oak Ridge National Laboratory is particularly well suited for such measurements. Its high neutron flux and flexible incident energy settings enable broad $(\mathbf{Q},\omega)$ coverage with meV-scale energy resolution, ideal for resolving the low-energy spin continua characteristic of kagome antiferromagnets. For single crystals of $ZnCu_3(OH)_6FBr$ (Zn-Barlowite) and $ZnCu_3(OH)_6Cl_2$ (Herbertsmithite), the magnetic scattering intensity is concentrated at small momentum transfers below ~ 3 Å^{-1}, corresponding to the first few Brillouin zones of the kagome lattice. CNCS provides excellent sensitivity in this regime, enabling a quantitative comparison between experimental spectra and theoretical models of fractionalized excitations.

Complementary information can also be obtained using triple-axis spectrometers such as HB-1A at the High Flux Isotope Reactor. Unlike time-of-flight instruments, which map large regions of $(\mathbf{Q},\omega)$ simultaneously, triple-axis spectrometers measure selected points in reciprocal space with high precision and controlled resolution. Such measurements are particularly valuable for studying field-dependent phenomena and static or quasi-static correlations in frustrated magnets. In later chapters, these methods are applied to the compound $Cu_4(OH)_6FBr$ (Barlowite II) to investigate how applied magnetic fields modify the underlying spin correlations.

This section reviews the theoretical framework connecting the measured neutron intensity to the microscopic spin correlations in QSLs. We begin by outlining the fundamental neutron–matter interaction and the resulting magnetic scattering cross section, before relating these expressions to

the dynamic spin structure factor $S(\mathbf{Q},\omega)$ and its manifestations in kagome quantum magnets.

1.5.1 Neutron–Matter Interaction and the Magnetic Cross Section

The interaction between a neutron and a magnetic material arises from the coupling of the neutron's spin magnetic moment to the internal magnetic fields produced by unpaired electron spins in the sample. Within first-order perturbation theory, the scattering process is described by Fermi's golden rule, which gives the probability per unit time for a neutron with initial wavevector $\mathbf{k}_i$ and spin state σ_i to scatter into a final state $\mathbf{k}_f, \sigma_f$ with an energy transfer $\hbar\omega = E_i - E_f$ and momentum transfer $\mathbf{Q} = \mathbf{k}_i - \mathbf{k}_f$:

$$\frac{d^2\sigma}{d\Omega\, dE_f} = \frac{k_f}{k_i} \sum_{\alpha,\beta} \left(\delta_{\alpha\beta} - \frac{Q_\alpha Q_\beta}{Q^2} \right) |F(\mathbf{Q})|^2 S^{\alpha\beta}(\mathbf{Q},\omega). \tag{1.1}$$

Here, $F(\mathbf{Q})$ is the magnetic form factor of the magnetic ion—reflecting the spatial distribution of its unpaired d-electron density—and $S^{\alpha\beta}(\mathbf{Q},\omega)$ is the dynamic spin correlation function, which encodes the intrinsic magnetic dynamics of the material. The prefactor $\left(\delta_{\alpha\beta} - Q_\alpha Q_\beta/Q^2\right)$ represents the polarization factor, ensuring that only spin components perpendicular to the scattering vector $\mathbf{Q}$ contribute to the magnetic cross section, as neutron scattering is sensitive only to the transverse components of magnetization.

Equation 1.1 forms the foundation of inelastic neutron scattering analysis. For quantum spin liquids, this relationship takes on particular significance: since QSLs exhibit no static long-range order, the entire magnetic response is encoded in the dynamic component $S(\mathbf{Q},\omega)$. The measured intensity directly reflects the frequency-resolved spin correlations of an entangled, fluctuating ground state, rather than coherent magnons of an ordered phase.

The scattering amplitude is derived from the magnetic dipole interaction Hamiltonian between the neutron and the sample:

$$\mathcal{H}_{\text{int}} = -\frac{2\mu_B}{\hbar}\, \mathbf{s}_n \cdot \mathbf{B}(\mathbf{r}_n), \tag{1.2}$$

where $\mathbf{s}_n$ and $\mathbf{r}_n$ are the neutron spin and position, and $\mathbf{B}(\mathbf{r}_n)$ is the magnetic field generated by the electronic moments in the sample. By expressing $\mathbf{B}(\mathbf{r}_n)$ in terms of the Fourier-transformed spin density $\mathbf{S}(\mathbf{Q})$ and applying time-dependent perturbation theory, one arrives at Eq. 1.1. The derivation naturally separates into the geometric polarization term, the form factor, and the intrinsic dynamic correlations of the material.

For practical data analysis, it is common to rewrite Eq. 1.1 in a compact form proportional to the imaginary part of the dynamical susceptibility:

$$\frac{d^2\sigma}{d\Omega\, dE_f} = C|F(\mathbf{Q})|^2 \left(1 - \frac{(\mathbf{Q}\cdot\hat{\mathbf{M}})^2}{Q^2} \right) \frac{1}{\pi[1 - e^{-\hbar\omega/k_B T}]} \chi''(\mathbf{Q},\omega), \tag{1.3}$$

where C is a constant determined by instrument calibration and $\chi''(\mathbf{Q},\omega)$ is the imaginary part of the dynamic magnetic susceptibility. This form makes explicit the connection between neutron scattering intensity and the linear response of the system to a magnetic perturbation.

For kagome quantum spin liquids such as Zn-Barlowite, the broad continua observed in $S(\mathbf{Q},\omega)$ arise from fractionalized excitations that cannot be described as single-spin flips. The cross-section formalism above thus provides the crucial bridge between the measured scattering intensity and the many-body correlations that define these highly entangled magnetic states.

1.5.2 The Dynamic Spin Structure Factor $S(\mathbf{Q},\omega)$

The key quantity that connects theory to experiment in magnetic neutron scattering is the dynamic spin structure factor $S(\mathbf{Q},\omega)$, which encodes the space–time correlations of magnetic moments in the sample. Formally, it is defined as the Fourier transform of the spin–spin correlation function:

$$S^{\alpha\beta}(\mathbf{Q},\omega) = \frac{1}{2\pi\hbar N}\sum_{i,j} e^{-i\mathbf{Q}\cdot(\mathbf{r}_i-\mathbf{r}_j)}\int_{-\infty}^{\infty} dt\, e^{i\omega t}\langle S_i^{\alpha}(0)S_j^{\beta}(t)\rangle. \tag{1.4}$$

Here, $\langle S_i^{\alpha}(0)S_j^{\beta}(t)\rangle$ is the quantum mechanical expectation value of the spin correlation between sites i and j, and N is the number of spins in the sample. For systems with isotropic spin interactions, the diagonal terms dominate and one typically writes $S(\mathbf{Q},\omega) = \sum_{\alpha} S^{\alpha\alpha}(\mathbf{Q},\omega)$.

In magnetically ordered systems, $S(\mathbf{Q},\omega)$ exhibits sharp, dispersive peaks corresponding to well-defined collective excitations (magnons) emerging from the Bragg wavevectors of the ordered state. In quantum spin liquids, however, these delta-function-like modes are replaced by a broad continuum of intensity, reflecting fractionalized spin excitations that carry spin-1/2 but no net charge. This diffuse continuum in $S(\mathbf{Q},\omega)$ is one of the defining experimental signatures of a QSL and directly reflects the absence of symmetry breaking in the ground state.

Physically, $S(\mathbf{Q},\omega)$ provides a momentum- and energy-resolved map of how spin correlations propagate through the lattice. For the kagome Heisenberg antiferromagnet, theoretical approaches such as Density Matrix Renormalization Group (DMRG) and parton mean-field theories predict a broad intensity centered near the Brillouin zone boundaries, with little temperature dependence below $\sim J/10$. The characteristic energy scale of this continuum, typically a few meV for $ZnCu_3(OH)_6Cl_2$ and $ZnCu_3(OH)_6FBr$, corresponds to the exchange constant J, and can be quantitatively extracted from the momentum-integrated scattering spectra.

Experimentally, $S(\mathbf{Q},\omega)$ is obtained from the measured neutron intensity after correcting for background, instrumental resolution, and the magnetic form factor. The resulting quantity can then be compared directly to numerical simulations of model Hamiltonians, providing stringent constraints on the microscopic exchange parameters and on possible anisotropies such as Dzyaloshinskii–Moriya (DM) interactions.

In Zn-Barlowite, the observed scattering at CNCS displays the hallmarks of this quantum continuum: broad, nearly featureless magnetic intensity extending up to ∼15 meV, with no evidence of sharp magnon peaks or spin gaps down to the base temperature. This will be presented later in Chapter 3.2 of this thesis. Such spectra confirm that the dynamic spin structure factor in these materials is dominated by short-range, highly entangled correlations rather than long-lived quasiparticles, consistent with theoretical expectations for a kagome quantum spin liquid.

1.5.3 From Spin Hamiltonian to Observable Scattering

The form of the dynamic structure factor $S(\mathbf{Q}, \omega)$ ultimately reflects the underlying spin Hamiltonian of the material. For kagome antiferromagnets such as $ZnCu_3(OH)_6FBr$ and $ZnCu_3(OH)_6Cl_2$, the dominant interactions are well captured by a nearest-neighbor Heisenberg model:

$$H = J_1 \sum_{\langle i,j \rangle} \mathbf{S}_i \cdot \mathbf{S}_j + \sum_{\langle i,j \rangle} \mathbf{D}_{ij} \cdot (\mathbf{S}_i \times \mathbf{S}_j) + J_2 \sum_{\langle\langle i,j \rangle\rangle} \mathbf{S}_i \cdot \mathbf{S}_j + J_\perp \sum_{\langle i,j \rangle_{\text{inter}}} \mathbf{S}_i \cdot \mathbf{S}_j, \tag{1.5}$$

where J_1 is the dominant antiferromagnetic exchange within the kagome plane, $\mathbf{D}_{ij}$ represents Dzyaloshinskii–Moriya (DM) interactions allowed by the lattice symmetry, J_2 accounts for next-nearest-neighbor coupling, and $J_\perp$ denotes the much weaker interlayer exchange mediated through the nonmagnetic ion (Zn^{2+}, Mg^{2+}, or similar). The relative magnitudes of these parameters determine whether the ground state exhibits long-range order, weak spin canting, or a fully disordered quantum spin liquid phase. Work presented later in this thesis strongly suggests $J_1 \approx 14meV$ with all other exchange energies hovering around 10% of this value.

In ordered magnets, linear spin-wave theory provides a good approximation for $S(\mathbf{Q}, \omega)$ by expanding the Hamiltonian around a classical ground state and diagonalizing the quadratic spin-wave Hamiltonian. This yields sharp dispersive magnon branches in the scattering spectrum. For QSL candidates, however, this approach fails because the ground state is not adiabatically connected to a classical configuration. Instead, theoretical modeling relies on numerical approaches such as exact diagonalization, DMRG, or parton mean-field theories, which compute $S(\mathbf{Q}, \omega)$ by representing spins in terms of fractionalized excitations—fermionic or bosonic spinons.

These calculations predict broad continua in $S(\mathbf{Q}, \omega)$ with momentum-dependent intensity patterns that are highly characteristic of the kagome geometry. In particular, the strongest scattering is expected near the zone boundaries of the two-dimensional Brillouin zone, often around the $(1, 0)$ and $(0.5, 0.5)$ positions, where destructive interference between neighboring spins produces enhanced dynamic correlations. The inclusion of DM interactions modifies these patterns by introducing weak anisotropy and shifting spectral weight between different symmetry points, while small interlayer couplings $J_\perp$ broaden the response slightly along the out-of-plane momentum L.

In experimental analysis, the connection between the Hamiltonian parameters and the observed

neutron spectra is made through model fitting or comparison to numerical simulations. For Zn-Barlowite, the high-field measurements described later in this work demonstrate that even moderate external fields primarily modify the impurity correlations while leaving the in-plane continuum intact—consistent with a robustly entangled ground state dominated by J_1 exchange. By quantitatively matching the measured $S(\mathbf{Q}, \omega)$ to model predictions, one can thus extract effective exchange parameters and assess proximity to the ideal kagome Heisenberg limit.

This mapping between Hamiltonian and observable scattering provides the theoretical backbone for interpreting neutron spectra in QSL candidates. It links the raw intensity data acquired at CNCS directly to microscopic spin interactions, allowing neutron scattering to serve as both a diagnostic and a benchmark for the emergence of quantum spin-liquid behavior.

1.5.4 Experimental Considerations

While the theoretical formalism of magnetic neutron scattering is general, its successful application to quantum spin liquids requires careful experimental design and quantitative treatment of instrumental effects. Because QSLs exhibit no static magnetic order, the magnetic signal is inherently weak and distributed across a broad continuum in energy and momentum, demanding high signal-to-noise measurements and precise background subtraction.

All inelastic neutron scattering data presented in this work were collected at the Cold Neutron Chopper Spectrometer (CNCS) at Oak Ridge National Laboratory. CNCS provides a high-flux cold-neutron beam with selectable incident energies $E_i = 1.55$–25 meV and sub-meV resolution, ideally suited for mapping the low-energy excitations of frustrated magnets. Single crystals were co-aligned on aluminum plates and their orientation was verified using Laue diffraction.

During measurement, the sample was rotated through a full 180° to achieve complete reciprocal-space coverage, while the time-of-flight geometry and large detector array allowed simultaneous access to both energy and momentum transfer—features critical for resolving the diffuse continua characteristic of kagome QSLs.

To reduce incoherent background from hydrogen, all Zn-Barlowite and Zn-Barlowite II samples were deuterated by synthesizing and exchanging in D_2O, which suppresses incoherent scattering by roughly an order of magnitude. This improvement arises from the large difference in nuclear spin-dependent scattering between protium and deuterium. For hydrogen (^{1}H, nuclear spin $I = 1/2$), the neutron–nucleus interaction depends strongly on whether the neutron spin is parallel or antiparallel to the proton's spin, producing widely differing scattering lengths in the singlet and triplet spin channels. The resulting fluctuations yield an incoherent cross section of $\sigma_{\text{inc}} \approx 80$ barns—over forty times larger than for deuterium (^{2}H, $I = 1$), where the two spin states have nearly equal scattering lengths and $\sigma_{\text{inc}} \approx 2$ barns. This statistical suppression of spin-dependent scattering makes deuteration an essential step in the accurate measurement of weak magnetic signals in hydroxide-based compounds such as Zn-Barlowite.

Typical total sample masses were about 750 mg, composed of several co-aligned single crystals with a combined mosaic spread of $\sim 3^\circ$. This deuteration step, together with low-temperature operation, proved essential for isolating the intrinsic magnetic continuum from phonon contributions.

Raw neutron events were reduced to four-dimensional intensity data $I(\mathbf{Q}, \omega)$ using the DAVE software package. Backgrounds from the empty sample holder and cryostat were subtracted, and detector efficiencies were corrected using a vanadium standard.

The instrumental resolution at CNCS is well described by a four-dimensional Gaussian function in $(\mathbf{Q}, \omega)$ space, parameterized by the incident energy and chopper configuration. For $E_i = 3.32$ meV, the full width at half maximum (FWHM) of the elastic line is approximately 0.08 meV, while the in-plane momentum resolution is typically $\Delta Q = 0.05$–0.1 Å^{-1}. In the vertical direction, the resolution is much broader and data are effectively integrated over a small range of out-of-plane momentum L. To compare experimental spectra with theoretical models, calculated $S(\mathbf{Q}, \omega)$ functions were convolved with the CNCS resolution function,

$$I_{\mathrm{calc}}(\mathbf{Q}, \omega) = \int R(\mathbf{Q} - \mathbf{Q}', \omega - \omega')\, S(\mathbf{Q}', \omega')\, d\mathbf{Q}'\, d\omega', \tag{1.6}$$

where $R(\mathbf{Q}, \omega)$ represents the normalized instrumental resolution. This convolution ensures that simulated intensity maps reflect the same broadening and asymmetry present in the measured data.

The resolution analysis is particularly important for field-dependent measurements, where energy broadening can arise both from instrumental effects and from genuine field-induced modifications of the excitation spectrum.

Complementary elastic neutron scattering experiments on Barlowite II were performed at the HB-1A triple-axis spectrometer at the High Flux Isotope Reactor (HFIR). Unlike the time-of-flight geometry of CNCS, HB-1A employs fixed incident and scattered neutron energies defined by a pyrolytic-graphite monochromator and analyzer, providing high precision for tracking field-induced changes at selected reciprocal-lattice positions. All measurements at HB-1A were elastic and carried out within the $(H\,0\,L)$ scattering plane using a vertical-field 8 T superconducting cryomagnet. This configuration constrains reciprocal-space access to the horizontal plane but enables detailed mapping of field-dependent Bragg intensities associated with weak interlayer correlations. The HB-1A resolution function forms an ellipsoidal volume in reciprocal space, determined by the spectrometer's collimation and energy settings; at $E_i = 14.7$ meV, the instrumental momentum resolution is typically $\Delta Q \approx 0.03$ Å^{-1}. .

Together, the CNCS and HB-1A experiments provide complementary views of the spin dynamics in the Barlowite family: CNCS mapping the full diffuse continuum in zero field, and HB-1A resolving field-induced elastic correlations. Accurate modeling of each instrument's resolution function was essential to separate intrinsic magnetic effects from instrumental broadening. These combined measurements therefore represent one of the most detailed and quantitatively calibrated characterizations of magnetic correlations in the kagome quantum spin-liquid regime.

1.5.5 Gaussian Approximation of the Resolution Function

In a real scattering experiment, however, the measured intensity is not the bare partial differential cross section, but its convolution with the instrumental resolution:

$$I(\mathbf{Q}_0,\omega_0) = \int \frac{d^2\sigma}{d\Omega_f\, dE_f}\, R(\mathbf{Q}-\mathbf{Q}_0,\, \omega-\omega_0)\, d\mathbf{Q}\, d\omega = \int S(\mathbf{Q},\omega)\, R(\mathbf{Q}-\mathbf{Q}_0,\, \omega-\omega_0)\, d\mathbf{Q}\, d\omega. \quad (1.7)$$

We can re-write the partial cross section in terms of the scattering function $S(\mathbf{Q},\omega)$, while the prefactors are absorbed into the (instrument- and geometry-dependent) resolution function $R(\mathbf{Q}-\mathbf{Q}_0,\omega-\omega_0)$.

In the Gaussian approximation, the resolution is modeled as a four-dimensional (4D) Gaussian distribution in energy–momentum space:

$$R(\mathbf{Q}-\mathbf{Q}_0,\omega-\omega_0) \equiv R(\Delta\mathbf{Q}) = R_0\, \exp\!\left[-\tfrac{1}{2}\,\Delta\mathbf{Q}^{\,T}\,\mathbf{M}\,\Delta\mathbf{Q}\right], \qquad \Delta\mathbf{Q} = (q_x, q_y, q_z, \hbar\omega), \quad (1.8)$$

with a 4×4 symmetric matrix $\mathbf{M}$. We adopt the conventional $\mathbf{Q}$-*system* coordinates: $\hat{x} \parallel \mathbf{Q}_0$, $\hat{z}$ normal to the scattering plane, and $\hat{y}$ completing a right-handed triad. The resolution is visualized as a 4D ellipsoid centered at $(\mathbf{Q}_0,\omega_0)$. In the paraxial approximation, the vertical coordinate decouples from the in-plane ones, implying $M_{xz} = M_{zx} = 0$.

When one needs peak *shapes* and intrinsic *widths*, the rigorous analysis performs the full convolution in the above equation. In many cases, however, only *integrated* intensities are required (e.g., for magnetic structure refinement like in our Barlowite II experiment), and simpler strategies suffice.

For coherent *elastic* scattering from a perfect crystal, the energy axis may be dropped and the resolution reduced to 3D:

$$R(\mathbf{Q}-\mathbf{Q}_0) = R_0\, \exp\!\left[-\tfrac{1}{2}\,\Delta\mathbf{Q}^{\,T}\,\mathbf{M}\,\Delta\mathbf{Q}\right]. \quad (1.9)$$

For both nuclear and magnetic Bragg scattering, the elastic differential cross sections (cf. previous equations) are commonly written as [**?**]

$$\left(\frac{d\sigma}{d\Omega}\right)_{\text{Bragg}} = A\frac{|\mathbf{F}|^2}{\nu^2}, \quad (1.10)$$

where $\mathbf{F}$ is the (nuclear or magnetic) structure factor, ν the unit-cell volume, and A a geometry/flux/sample/time scale factor (constant across a fixed series of measurements). For a perfect crystal, a nuclear Bragg reflection at $\mathbf{Q}_b$ is modeled by a delta function:

$$S(\mathbf{Q}) = S_0\, \delta(\mathbf{Q}-\mathbf{Q}_b). \quad (1.11)$$

Then the measured intensity becomes

$$I(\mathbf{Q}_0) = \int S(\mathbf{Q})\, R(\mathbf{Q} - \mathbf{Q}_0)\, d\mathbf{Q} = S_0\, R(\mathbf{Q}_b - \mathbf{Q}_0), \tag{1.12}$$

and a scan through $\mathbf{Q}_b$ yields the integrated intensity

$$\text{Int. } I(\mathbf{Q}_b) = S_0 \int R(\mathbf{Q}_b - \mathbf{Q}_0)\, d\mathbf{Q}_0. \tag{1.13}$$

Thus, even for elastic Bragg peaks, the integrated intensity depends both on the intrinsic cross section at the Bragg condition and on the line integral of the resolution along the scan trajectory in reciprocal space.

The above expression applies to long-range-ordered (LRO) elastic peaks. For *short-range*-ordered (SRO) elastic features (e.g., broadened magnetic peaks), the delta-function model no longer holds. A practical correction can be obtained under three assumptions: (i) the scattering function is a 3D Gaussian centered at $\mathbf{Q}_b$,

$$S(\mathbf{Q}) = S_0\, \frac{1}{\sqrt{2\pi}\,\sigma_x}\, e^{-q_x^2/(2\sigma_x^2)}\, \frac{1}{\sqrt{2\pi}\,\sigma_y}\, e^{-q_y^2/(2\sigma_y^2)}\, \frac{1}{\sqrt{2\pi}\,\sigma_z}\, e^{-q_z^2/(2\sigma_z^2)}, \tag{1.14}$$

(ii) within the narrow scan window, the resolution may be approximated by $R(\mathbf{Q}-\mathbf{Q}_b)$ (i.e., it varies slowly near $\mathbf{Q}_b$), and (iii) the off-diagonal in-plane coupling $M_{xy} = M_{yx} \approx 0$, since the resolution ellipsoid's major axis is typically aligned close to $\hat{y}$ due to a relatively large sample mosaic.

Because the convolution of two Gaussians is Gaussian, one obtains an integrated-intensity formula analogous to the previous expression but with a direction-dependent correction factor. For example, for a θ-scan in the $(HK0)$ plane, the correction factor is

$$\frac{1}{\sqrt{(M_{xx}\,\sigma_x^2 + 1)\,(M_{zz}\,\sigma_z^2 + 1)}}. \tag{1.15}$$

These equations allow one to separate the intrinsic scattering function from measured intensities without executing the full 3D convolution. Much of the coding for the above equations was carried out by my predecessor Wei He in python utilizing neutronPy, and I remain extremely grateful for his contributions and help. You can read his thesis here [7]

When only *relative* changes in magnetic scattering are needed, the above procedures suffice. For *absolute* quantities (e.g., ordered moments), an additional absolute normalization is required. Two standard routes are (a) normalizing to nuclear Bragg peaks of the sample (thereby fixing A by comparing measured and calculated $|\mathbf{F}|^2$), or (b) normalizing to the incoherent elastic scattering from a vanadium standard of known mass/geometry. For a constant-$\mathbf{Q}$ scan in energy on vanadium, the energy-integrated intensity directly informs the resolution function.

1.5.6 Summary

This introductory section the theoretical and practical framework of neutron scattering as applied to magnetic materials and, in particular, to quantum spin liquids. Starting from the fundamental neutron–matter interaction, we derived the magnetic cross section and its relation to the dynamic spin structure factor $S(\mathbf{Q}, \omega)$, which encodes the space–time correlations of the underlying spins. In contrast to conventional magnets, quantum spin liquids exhibit no static long-range order, and their scattering response is dominated by a broad, continuum-like spectrum of fractionalized excitations. Inelastic neutron scattering is therefore uniquely capable of revealing these dynamics by directly measuring the momentum- and energy-resolved magnetic fluctuations.

We also discussed how realistic experimental data must be interpreted through the instrument's resolution function and how, in the Gaussian approximation, this function defines an effective convolution kernel between the intrinsic scattering and the measured intensity. For elastic measurements, the same framework connects Bragg-peak intensities to the static structure factor, while for short-range order it provides analytic corrections for finite correlation lengths. Together, these formalisms provide the quantitative link between model Hamiltonians, calculated correlation functions, and the observables in a real experiment.

The concepts developed here—cross sections, dynamic structure factors, and resolution effects—form the basis for all subsequent chapters of this thesis. They provide the theoretical foundation needed to interpret the neutron scattering studies presented later on the kagome antiferromagnets $ZnCu_3(OH)_6FBr$ and $Cu_4(OH)_6FBr$, where these principles are applied to uncover the signatures of quantum spin-liquid behavior and field-induced correlations.

Chapter 2

In Field Elastic Neutron Scattering of Barlowite II

2.1 Introduction

The spin-$\frac{1}{2}$ kagome antiferromagnet has long been considered an ideal host for a quantum spin liquid (QSL) ground state, an exotic magnetic state characterized by the absence of long-range order down to the lowest temperatures and the presence of long-range quantum entanglement [8]. The kagome lattice, consisting of corner-sharing triangles, is a prototypical geometry for magnetic frustration. One candidate realization is the resonating valence bond (RVB) state proposed by Anderson [3], in which singlets of entangled spins fluctuate over the lattice without static ordering.

Through their potential to host topologically protected excitations, QSLs have been proposed as platforms for quantum computation and high-density data storage [9]. Among known kagome antiferromagnets, Barlowite, $Cu_4(OH)_6FBr$, is structurally similar to the celebrated QSL candidate Herbertsmithite, $Cu_3Zn(OH)_6Cl_2$ [10, 5, 11]. However, in Barlowite the interlayer sites are occupied by Cu^{2+} ions, resulting in long-range magnetic order below $T_N \approx 15$ K [12, 13]. Substituting these interlayer sites with nonmagnetic Zn^{2+} suppresses long-range order and leads to QSL behavior [14, 15], a result strongly supported by recent inelastic neutron scattering studies on Zn–Barlowite.

In addition to its relevance as a progenitor material for QSL physics, Barlowite itself is an intriguing frustrated magnet. Two polymorphs can be grown reproducibly through different synthesis pathways, with nearly indistinguishable room-temperature structures but different low-temperature magnetic orders [1, 16]. This extreme sensitivity to perturbations motivates the present study, in which we probe the magnetic ground state of Barlowite in the presence of an external magnetic field.

2.2 Experimental Methods

Elastic neutron scattering measurements were carried out at the HB-1A triple-axis spectrometer at the High Flux Isotope Reactor (HFIR), Oak Ridge National Laboratory. A large co-aligned crystal array of Barlowite II crystals was mounted in the $(H0L)$ scattering plane. Magnetic fields up to 8 T were applied in the in-plane $(HH0)$ direction using a vertical-field cryomagnet, with base temperatures of 1.5 K achieved via a pumped ^{4}He insert.

To isolate the magnetic scattering from peaks overlapping with structural Bragg reflections, we measured intensities at three temperatures: base temperature (1.5 K), 8 K, and 20 K. The choice of 20 K is above all known magnetic phase transitions in Barlowite, while being low enough to minimize changes in lattice constants from thermal contraction. The intermediate temperature of 8 K falls within the stability range of the exotic low-temperature phase reported in Smaha *et al* [1], allowing us to examine its response to field.

2.2.1 Subtraction procedure for isolating magnetic scattering

Many of the magnetic peaks in Barlowite coincide in Q-space with strong structural Bragg peaks. In order to isolate the magnetic contribution to such peaks, we measured each at three temperatures: 1.5 K, 8 K, and 20 K. The 20 K point was intentionally chosen to be above both known magnetic ordering transitions, while still close enough to base temperature that changes in the lattice constants from thermal contraction were minimal. This allows the 20 K measurement to serve as a proxy for the purely structural scattering background.

A naïve approach would be to fit the combined nuclear and magnetic peaks at both temperatures with a simple function (e.g., Gaussian or Lorentzian), and subtract the fits from each other. Then the residual can be integrated to get an estimate of the magnetic scattering intensity. However, this approach fails here for two key reasons:

1. **Dominance of the nuclear contribution:** The nuclear Bragg peaks are roughly 10^2–10^4 times more intense than the magnetic peaks. Given that our magnetic signal is on the order of 1% of the total, even small uncertainties in the nuclear fit translate into large relative errors in the magnetic intensity. This is a particular issue here since the magnetic scattering from our frustrated spin $\frac{1}{2}$ Cu^{2+} system is very weak relative to that of a typical experiment;

2. **Crystal-array geometry:** The use of a large crystal array, rather than a perfect single crystal, leads to broadened and somewhat irregular peak profiles. This further destabilizes the fit when attempting to extract a small magnetic component from a much larger nuclear background.

These issues are illustrated in Fig. 2.1(a,b). Even though the 1.5 K data lie systematically above the 20 K data at the peak maximum, the Gaussian fits overlap within their 2σ uncertainty bands,

making the extracted magnetic contribution unreliable.

An alternative would be to subtract the raw intensities at each 2θ directly. However, the spectrometer does not necessarily sample the *exact* same angular points at each temperature due to differences in instrument alignment and environmental factors. This mismatch is especially problematic near the steep flanks of the Bragg peaks, where a small angular offset produces a large intensity difference unrelated to magnetic scattering. Binning the data to match 2θ points is also unsatisfactory, since it can smear out fine features and introduce artifacts if there is any systematic drift in the peak position.

To address this, we adopt an interpolation-based subtraction procedure:

1. Fit the 20 K nuclear-only dataset with a smooth interpolation function that passes through all measured points. In practice, we use a cubic spline, which is flexible enough to capture the actual lineshape without overfitting to noise.

2. For each point in the low-temperature (1.5 K or 8 K) dataset, evaluate the interpolated 20 K function at the same 2θ.

3. Subtract the interpolated value from the measured low-temperature intensity to obtain the net magnetic contribution at that Q.

This method preserves the precise angular information of the low-temperature measurement while ensuring that the high-temperature baseline is matched exactly in 2θ. It also avoids amplifying statistical noise by fitting both datasets independently and subtracting the fits.

The procedure is visualized in Fig. 2.1(c,d). Panel (c) shows the smooth interpolation of the 20 K nuclear data (black curve) and the direct point-by-point subtraction from the 1.5 K data. Panel (d) zooms in on the circled region, with the vertical segment Δy illustrating the extracted magnetic contribution at that specific Q.

This approach yields a more reliable estimate of the weak magnetic scattering and is especially important for peaks with strong nuclear contributions, such as $(1, 0, 0)$, $(1, 0, 2)$, and $(1, 0, 4)$. For purely magnetic peaks like $(0.5, 0, 1)$, no subtraction is necessary, but it is worth noting that the base signal is much weaker, especially since this corresponds to a super lattice peak. I should also add a note on the nomenclature here. We are indexing peaks based upon the room-temperature crystalline structure here. However, the exotic, q=0 pinwheel magnetic ordering leads to a unit cell doubling at low temperatures [1]. This is why there are purely magnetic half integer peaks at low temperatures. All other integer peaks are coincident with nuclear peaks.

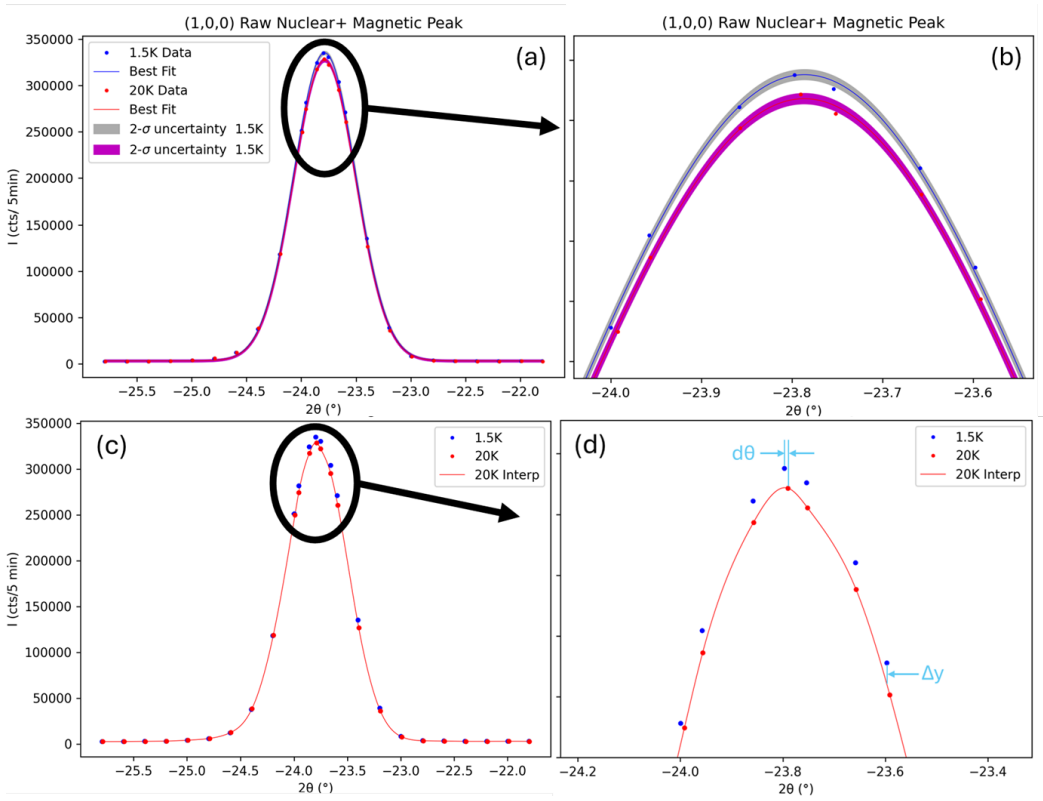

Figure 2.1: (a) Combined nuclear and magnetic $(1, 0, 0)$ peak at 1.5 K (red) and 20 K (blue) with Gaussian fits and shaded 2σ uncertainty bands. Inset: zoom of the peak maximum, showing that the 1.5 K data lie systematically higher due to magnetic scattering, though the Gaussian fits overlap within error. (b) Magnified view of the circled region in (a). (c) Interpolation-based subtraction procedure: the 20 K data are interpolated to the 2θ points of the low-T scan, then subtracted point-by-point. (d) Magnified view of the circled region in (c). The vertical blue segment (Δy) represents the difference attributed to magnetic scattering. This method minimizes subtraction artifacts due to slight angular misalignments or peak shifts, which is critical when the magnetic signal is $\sim$1% of the total intensity.

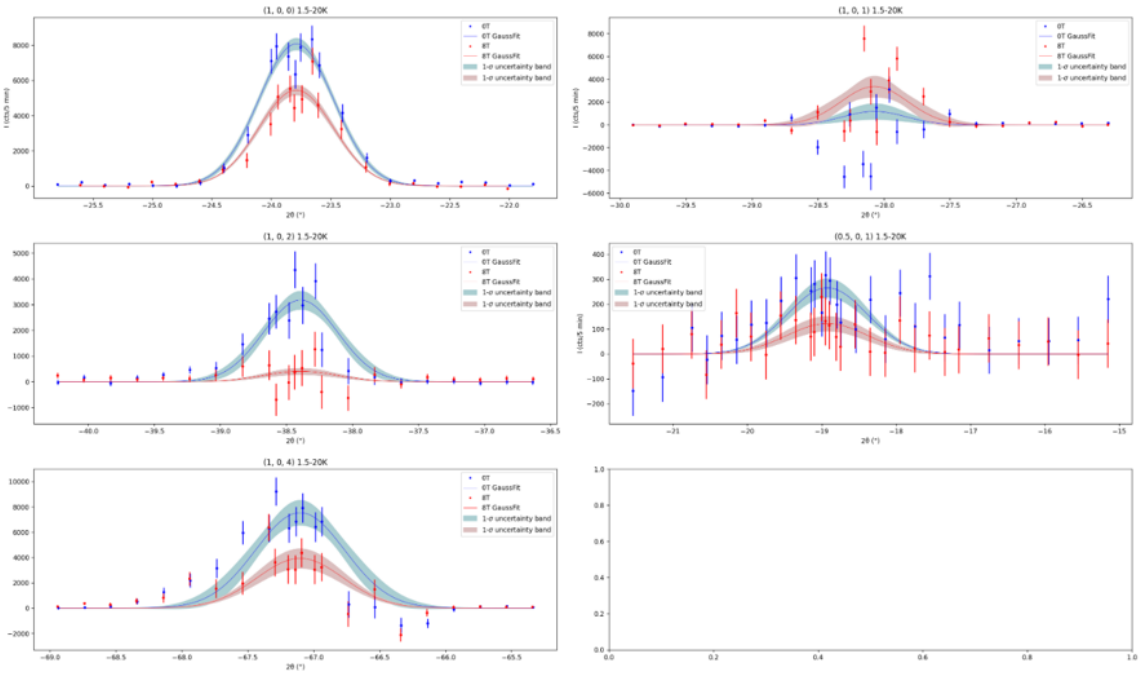

Figure 2.2: Magnetic scattering peaks at 1.5 K after subtraction of the 20 K data, shown in zero field (blue) and with an in-plane 8 T field (red). Solid lines are Gaussian fits with fixed center and width; shaded bands indicate $\pm 1\sigma$ uncertainties in the fit amplitude. The field suppresses the $(1, 0, \text{even})$ peaks and enhances the $(1, 0, 1)$ peak, suggesting a modification of interlayer magnetic correlations.

2.3 Results

2.3.1 Temperature and field dependence of magnetic peaks

Figures 2.2 and 2.3 show the magnetic scattering after subtraction at 1.5 K and 8 K, respectively, in zero field and with an 8 T in-plane field. Gaussian functions were fit to the subtracted peaks using the python package `lmfit`, with the peak center fixed to the expected Bragg angle (determined from high-quality nuclear peaks) and the width fixed from the instrument resolution and estimated correlation lengths [1]. The only free parameter was the Gaussian amplitude.

The integrated intensities from these fits are summarized in Fig. 2.4. Peaks for which the top three data points were within error of zero were flagged as unreliable. From a scattering perspective, the most likely explanation for this is that the magnetic peak is simply 0 or near 0 due to destructive interference. Note also that peaks which fail this criterion tend to also have large negative points and non-gaussian-like line-shapes, which are both non-physical from a pure scattering perspective; the observed signal in these cases is probably just random noise left over from subtracting two big numbers in the procedure as described above. We find that the $(1, 0, \text{even})$ peaks are strongly

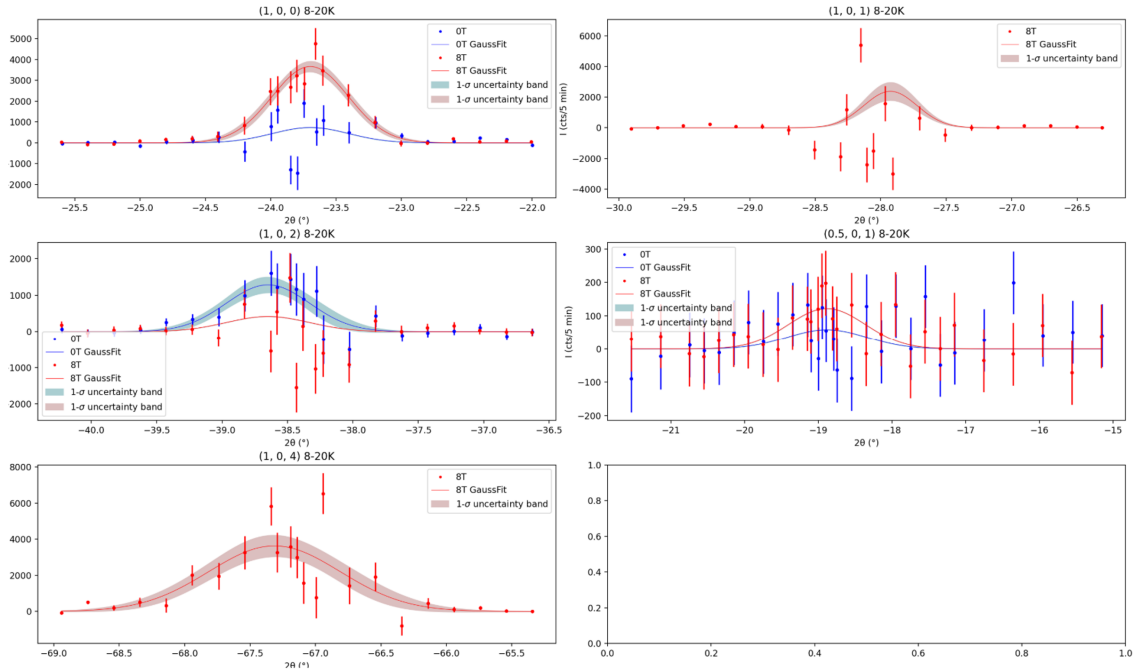

Figure 2.3: Magnetic scattering peaks at 8 K after subtraction of the 20 K data, in zero field (blue) and with an in-plane 8 T field (red). No zero-field data were collected for the $(1, 0, 1)$ and $(1, 0, 4)$ peaks at this temperature. The field response resembles the low-temperature behavior, suggesting that the field destabilizes the proposed pinwheel valence bond crystal phase at 8 K.

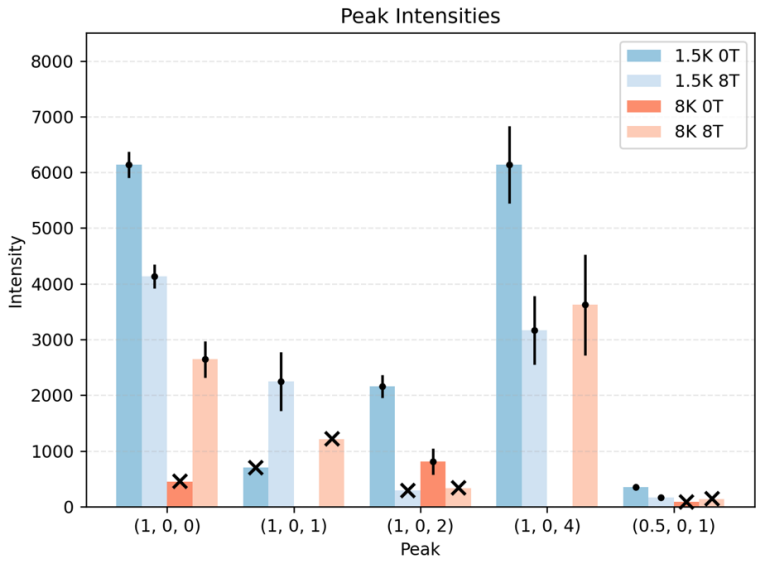

Figure 2.4: Integrated intensities of magnetic peaks at 1.5 K and 8 K, in zero field and with 8 T in-plane field, extracted from Gaussian fits to the subtracted data. Nuclear contributions have been removed for peaks overlapping with structural Bragg peaks. Crosses mark peaks whose maximum intensity is within error of zero, indicating unreliable measurements.

suppressed by the applied field, while the $(1, 0, 1)$ peak grows significantly, suggesting that the field perturbs the interlayer ordering.

2.3.2 Magnetic structure modeling

To interpret the field-dependent intensities, we followed the modeling approach of Ref. [1], restricting the unit cell to three moment types: K1, K2 (kagome spins), and I (interlayer spins). For the in-field data, moment magnitudes were fixed to their zero-field values, kagome-layer angles were constrained near 120°, The only significant free parameters were:

1. The rotation angle of the $q = 0$-like kagome spin pattern relative to the field direction.
2. The out-of-plane canting angle of the red K1-type spins.

It is worth noting that the only measured peak with any sensitivity to the interlayer is the incredibly weak (0.5,0,1) peak. Hence, all the interlayer moments we fixed to point in the same direction as the magnetic field. This seems like a reasonable assumption given the applied field should be strong relative to the fairly weak interlayer to kagome layer ferromagnetic coupling.

The best-fit in-field structure (Fig. 2.5) shows K1 spins canting further out of plane (from ∼29° to ∼70°) to reduce their Zeeman energy, accompanied by an overall rotation of the kagome plane moments relative to the field.

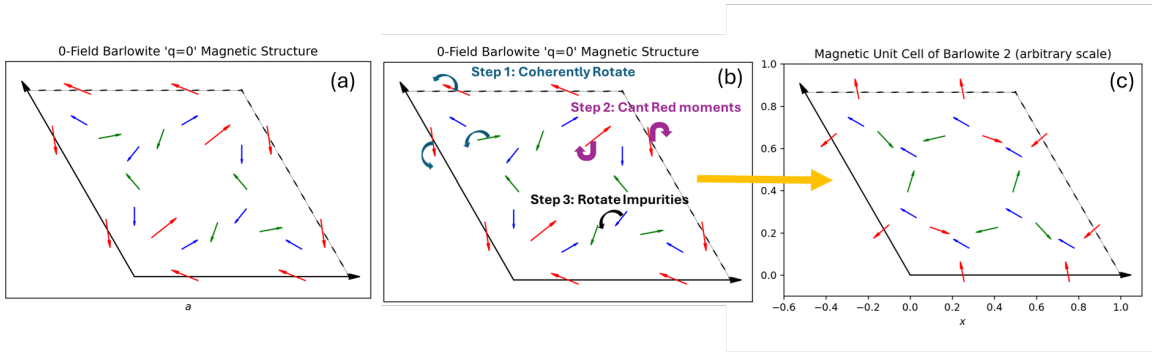

Figure 2.5: (a) Zero-field magnetic structure of Barlowite-2 from Ref. [1]. (b) Parameterization of in-field refinements: kagome spins rotated relative to the field and K1 spins canted out of plane. (c) Best-fit in-field structure for 8 T applied along $(HH0)$. The K1 spins cant further out of plane, reducing their in-plane component and aligning more with the field direction to lower the Zeeman energy.

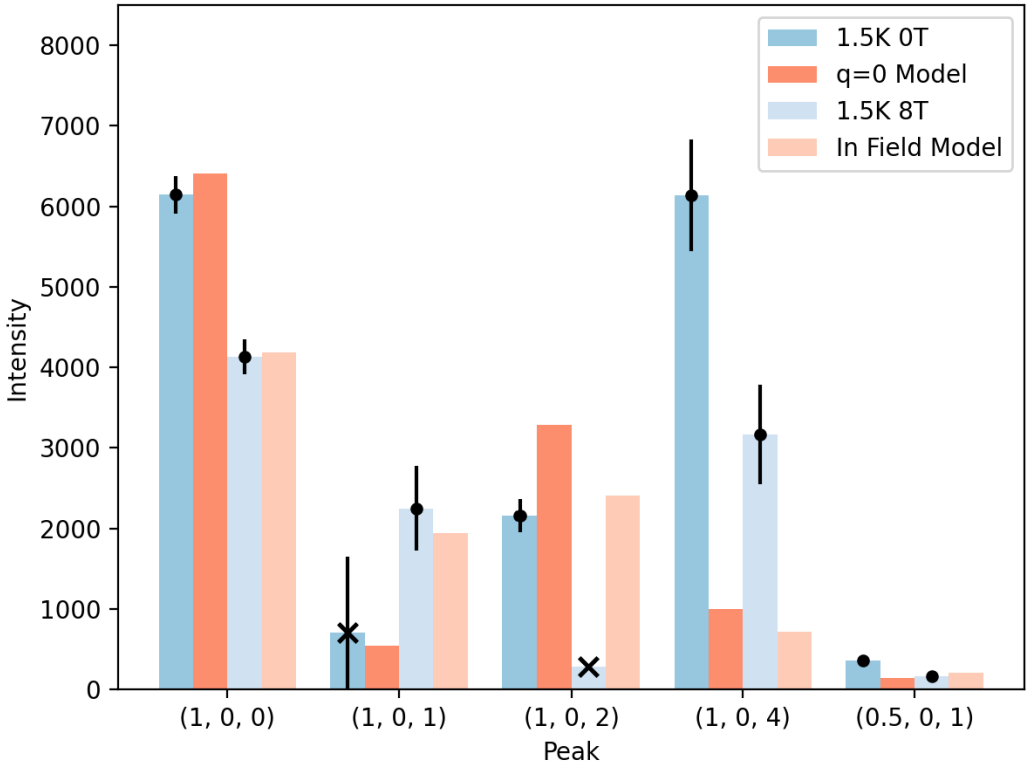

Figure 2.6: Comparison of measured and calculated integrated intensities for the zero-field (left) and in-field (right) models. The in-field refinement captures the suppression of $(1, 0, \text{even})$ peaks and enhancement of $(1, 0, 1)$, consistent with increased K1 canting out of plane.

2.4 Discussion

The in-field magnetic structure model described above successfully captures the most prominent qualitative trends in the experimental data: suppression of the $(1, 0, \text{even})$ peaks and enhancement of the $(1, 0, 1)$ peak in an 8 T in-plane field. These changes are consistent with the applied field modifying the interlayer magnetic correlations and inducing additional canting of the kagome-layer spins. In the refined in-field model, the K1-type spins cant further out of the kagome plane (from $\sim 29°$ to $\sim 70°$) while the entire $q = 0$-like kagome spin pattern rotates relative to the field direction.

From a fitting perspective, the model does an excellent job reproducing the most reliable dataset: the strong suppression of $(1, 0, 0)$ and the growth of $(1, 0, 1)$, as well as the modest changes to $(0.5, 0, 1)$. This last point is particularly encouraging, since $(0.5, 0, 1)$ is the only purely magnetic peak measured here and is sensitive to the alignment of interlayer moments. The fact that the model matches this within the experimental uncertainties provides some confidence in the overall approach.

In contrast, the fits to $(1, 0, 2)$ and $(1, 0, 4)$ are less satisfactory. One likely explanation is that these peaks retain some residual structural contributions after subtraction, due either to small changes in lattice parameters with temperature or to Debye–Waller effects. Because the nuclear scattering from these reflections is 1000–3000 times larger than the magnetic scattering, even a small systematic mismatch between the low- and high-temperature measurements can propagate into a relatively large error in the subtracted intensity. This limitation highlights the need for longer counting times or a cleaner single-crystal sample to improve statistics for these reflections. The upshot however is that the qualitative trend is right; both the models and the measured peak are suppressed by the applied magnetic field.

The proposed canting evolution can be understood qualitatively in terms of energy minimization. We considered a simple energy model with two contributions: (1) the nearest-neighbor Heisenberg exchange between kagome spins, estimated as $J \approx 14$ meV based on literature values for similar compounds, and (2) the Zeeman energy from the applied 8 T field. Using the refined spin orientations, the exchange energy is estimated to change from approximately -3.6 meV in zero field to -1.2 meV in the in-field configuration, while the Zeeman term changes from -0.04 meV to -0.2 meV. These values suggest that the in-field structure sacrifices some exchange energy in order to gain Zeeman energy, resulting in increased canting of the K1 spins toward the field direction. The notable issue though is that the Zeeman energy scale is an order of magnitude lower than the direct exchange, meanining that our in-field model is incomplete, either in terms of spin or energetic modeling.

Of course, several caveats apply. First, the J value is not directly measured here and may differ significantly from the estimate; a smaller J would make the Zeeman term comparatively more important. Second, the model is under-constrained: only five magnetic peaks were measured in field, and the fits involve fixed moment magnitudes and constrained spin angles to reduce the parameter space. This leaves open the possibility that other spin configurations could produce similar scattering patterns while having a more balanced energy performance (e.g. with slightly less canting). Third,

longer-range exchange pathways and anisotropic exchange terms, which are known to be relevant in other kagome magnets, are not included in this simple energy analysis. Finally, the zero-field $q = 0$ model itself is not uniquely determined by the available data, so any in-field refinements inherit this uncertainty.

Despite these limitations, the general conclusion seems like a feasible start: the kagome-layer spins respond to the applied field by rotating and canting further out of plane in a spin-flop like transition, consistent with a compromise between minimizing exchange energy and maximizing Zeeman energy. This conclusion is qualitatively consistent with in-field neutron powder studies of clinoatacamite [17, 18], which also found that applied fields induce substantial out-of-plane antiferromagnetic components. The main difference is that those studies suggested a spin structure built from antiferromagnetically coupled singlet pairs, whereas our results retain the 120° kagome-plane arrangement. Given the different interlayer environments in clinoatacamite and Barlowite, such differences are not unexpected.

The next step in modeling would be to add an additional tilt of each magnetic moment towards the applied magnetic field. In theory this should help to further minimize the Zeeman energy while minimally affecting the Heisenberg energy due to the additional out of plane canting. Minor perturbations may also preserve the good fit to the measured peaks. More peaks would be needed to properly refine this minor perturbation though. This step is outlined in Fig. 2.7.

Overall, these results reinforce the view that the kagome lattice, particularly in the presence of partially occupied interlayer sites, provides a rich playground for exotic and field-tunable magnetism. The extreme sensitivity of the Barlowite magnetic ground state to perturbations—whether chemical substitution, subtle structural differences, or applied magnetic field—underscores its value as a reference system for interpreting the more exotic spin dynamics of Zn–Barlowite, which will be explored in the next chapter.

2.5 Conclusions

Elastic neutron scattering at HB-1A reveals that the low-temperature magnetic order in Barlowite responds strongly to an in-plane magnetic field, with suppression of $(1, 0, \text{even})$ peaks, enhancement of $(1, 0, 1)$, and increased canting of K1 spins out of plane. These findings highlight the extreme sensitivity of the Barlowite ground state to perturbations, reinforcing its value as a model system for kagome magnetism and as a reference for understanding the QSL behavior of Zn–Barlowite.

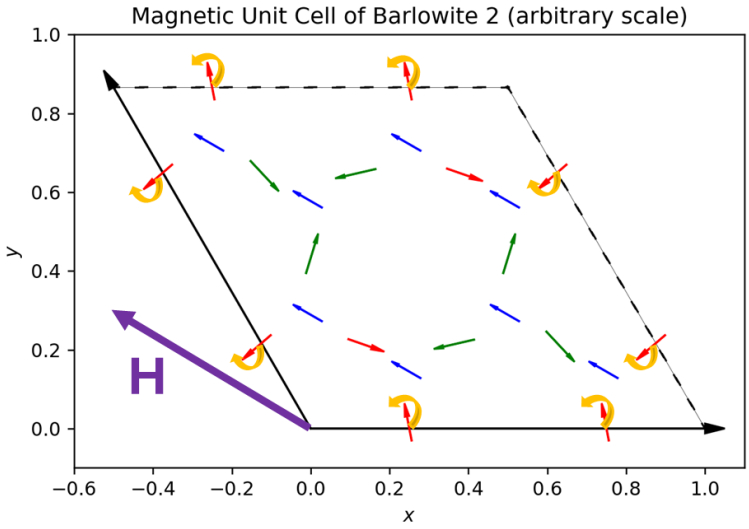

Figure 2.7: Figure showing the next free parameter that could be refined to further determine the structure of Barlowite II in an applied magnetic field. The yellow arrows indicate an additional perturbation towards the direction of the applied magnetic field that may help to further lower the Zeeman Energy.

Chapter 3

Inelastic Neutron Scattering on Zn-Barlowite

Introduction

The inelastic neutron scattering (INS) measurements presented in this chapter represent the most comprehensive investigation of Zn-barlowite's magnetic excitation spectrum to date. They were enabled by the first growth of large, high-quality, fully deuterated single crystals of this material—sufficient in mass and alignment precision to make detailed mapping of the dynamic structure factor $S(\mathbf{q}, \omega)$ feasible.

Across multiple experimental campaigns at the Cold Neutron Chopper Spectrometer (CNCS), we collected data spanning a broad range of energies, temperatures, and magnetic field conditions. This work establishes several important benchmarks for the study of kagome quantum spin liquid (QSL) candidates:

- **Observation of a robust spinon continuum**: At low temperature, Zn-barlowite exhibits a broad, nearly energy-independent continuum of magnetic scattering extending up to at least 3 meV, closely mirroring the behavior of the canonical QSL candidate herbertsmithite.
- **Separation of intrinsic kagome and impurity contributions**: Using a combination of empirical correlation modeling and temperature-dependent subtraction methods, we cleanly distinguished high-energy kagome-plane excitations from low-energy scattering associated with interlayer Cu^{2+} impurities.
- **Extraction of quantitative spin-spin correlations**: Fits to the momentum dependence across energies reveal dominant antiferromagnetic correlations on nearest-neighbor kagome

bonds, weaker ferromagnetic further-neighbor correlations, and a strong ferromagnetic coupling between impurities and their nearest kagome neighbors.

- **Evidence for a spin gap**: After isolating the kagome contribution, the intrinsic spectrum shows a gaplike onset at $\Delta \approx 1.1$ meV, in close agreement with herbertsmithite and consistent with a gapped $\mathbb{Z}_2$ QSL.
- **Robustness under temperature and field**: The kagome continuum persists up to $T \gtrsim 150$ K ($\sim J/5$) with little change in its high-energy form, while applied magnetic fields primarily suppress the impurity-dominated low-energy response.
- **Extension to new regimes**: Additional measurements probed out-of-plane scattering, higher incident energies up to 25 meV, and 14 T applied fields, each revealing new structural or dynamical aspects of the excitation spectrum.

By combining these diverse data sets, this chapter not only confirms the universality of kagome QSL physics in Zn-barlowite and Herbertsmithite, but also provides unprecedented quantitative detail on how intrinsic and impurity-driven excitations coexist and evolve under varying experimental conditions. The results here form the basis for three promising future publications on out-of-plane correlations, high-energy dynamics, and in-field behavior.

3.1 Techniques and Data Processing

3.1.1 Crystal Grown and Sample Preparation

A key challenge of studying Zn-Barlowite relative to Herbertsmithite is that Zn-Barlowite contains fluorine, which is highly reactive and can react with common growth chambers. This means that significant adaptation of growth methods was required relative to the large single crystal Herbertsmithite synthesis techniques used by my predecessors [19].

In the first step of crystal growth, hydrothermal reactions were performed in 45 ml PTFE-lined stainless steel autoclaves. Zn-substituted barlowite powder was synthesized in this reaction using CuO (Aldrich), NH_4F (Alfa, 96%), $ZnBr_2$ (BTC, 99.999%), and 20 ml D_2O (Aldrich, 99.9%). These contents are heated over 2.5 hrs from 35 °C to 185°C, held for 48 hrs, then cooled back to 30°C over 30h. The complete products of this pre-reaction (including both the Zn-barlowite powder and ion-rich D_2O) were placed into a 11.8mm OD thin-walled PFA Teflon liner and frozen. The end of the liner was then vacuum sealed ($\sim 10^{-2}$ Torr) and the liner and the contents were placed into a quartz tube with an inner diameter of 12.7mm and outer diameter of 18.7mm. With the contents frozen, vacuum was pulled in the quartz tube ($\sim 10^{-3}$ Torr) and it was sealed. The PFA Teflon liner is necessary for this growth to ensure the fluorine ions present in the D_2O do not react with the quartz tube; this removes them from the reaction and weakens the quartz tube, leading to an

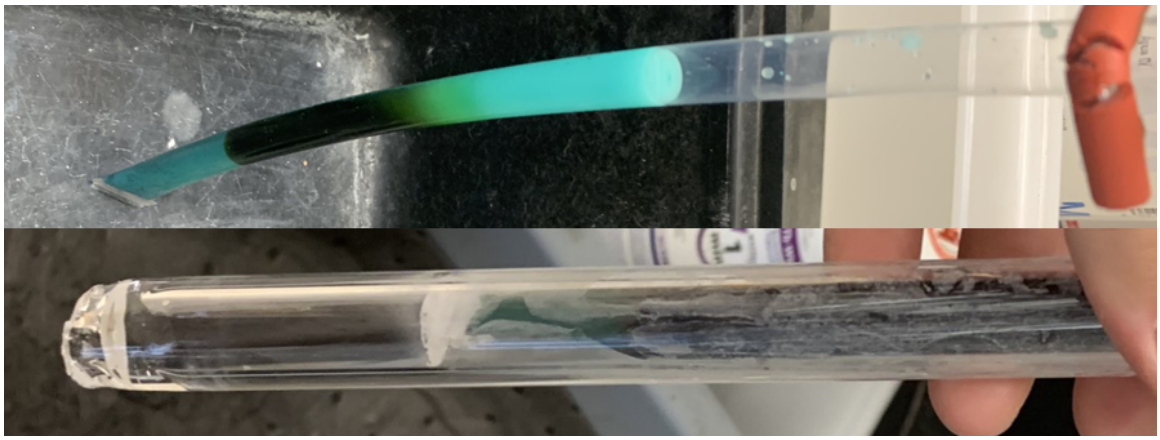

Figure 3.1: Figure showing the pre-reacted powder reactants for Zn-Barlowite in a Teflon liner (top), in addition to the Teflon liner sealed inside of a quartz tube (bottom). Note that the use of the plug in the bottom left is what makes sealing this Teflon liner inside of the quartz possible.

explosion hazard and impure growth. Note that the pre-reaction to form Zn-barlowite powder can also be performed directly in the Teflon-lined test tube; both methods can be effective, but the separate pre-reaction in the autoclave seemed to work more consistently for us.

An additional note is that this process is much more difficult than it may seem as simply described. The largest bottleneck is that quartz melts at $\sim 1600C$, while the PFA Teflon liner melts at $\sim 300C$. Note that the Teflon liner must also already be inside of the quartz when it is sealed. This makes it rather challenging to seal the quartz tube without completely melting the Teflon liner and causing it to leak fluoridated water, which will eat at the quartz test tube. The best recourse to deal with this is to use a long $\sim 2in$ long quartz plug so that the quartz can be sealed far away from the Teflon. This is shown in the top panel of Fig. 3.1. Thankfully, quartz has very poor thermal conductivity, so with practice, it is possible to get a reliable seal without affecting the Teflon's integrity.

Two separate quartz tube assemblies were made with this above process. Each was placed inside a three zone furnace for continued hydrothermal synthesis. The zones formed a temperature gradient with a ∼180°C hot end and a ∼170°C at the cold. The pre-reacted powder is manipulated to start at the hot end. Note that this itself may take some effort; especially when pre-reacting in the test tube, the powder contents can easily become stuck at the ends of the teflon liner.

In these furnace conditions, Zn-substituted barlowite powder will dissolve in the D_2O fluid at the hot end and will nucleate at the cold end as it is slowly thermally transported there. The growths were monitored regularly and ran for approximately one year. Each growth yielded several clumps of large crystals that were strongly attached to each other at domain walls. Manually separating these clumps with tweesers and a razor yielded single-domain crystals up to ∼5×5×0.1mm in size. ICP-AES measurements on the resulting groups of crystals revealed Zn concentrations of x=0.78 for batch

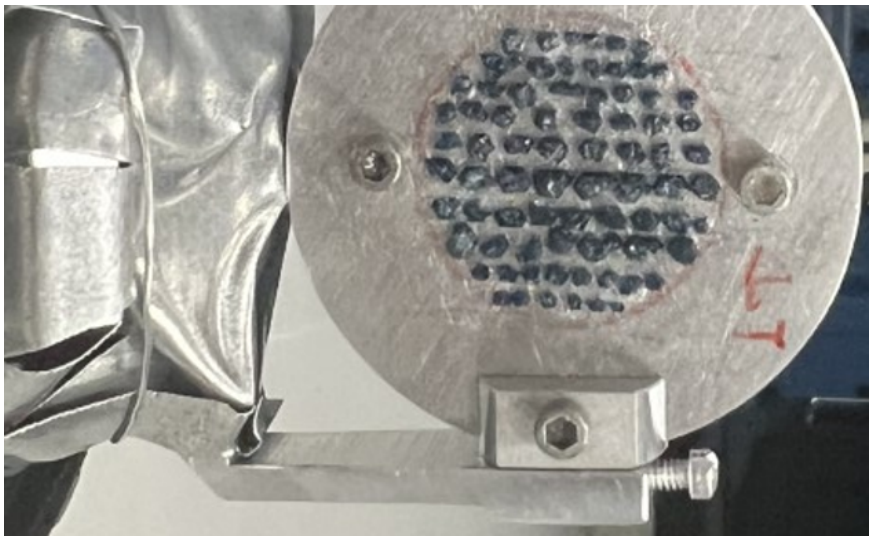

Figure 3.2: Co-alligned crystals of Zn-barlowite mounted on Aluminum plates that are affixed to the CNCS instrument sample holder. This sample contains 0.76g of Zn-barlowite crystals mounted across three vertically stacked plates. Neutrons were scattered off this crystal array to obtain the data reported, with the rough beam width indicated by the red circle on the plate shown.

one and x=0.85 for batch 2. Electron microprobe analysis was also performed and corroborated with the above measurements, revealing Zn-concentrations x=0.75 for batch one and x=0.85 for batch 2. 0.57 g of crystals from the first batch and 0.19 g from the second were coaligned on two mounting plates using CYTOP adhesive. This yielded a total sample mass of 0.76 g. The end product of these labors is displayed in Fig. 3.2.

Teflon Tube Sealing Detailed Procedure As the process is far from trivial, and is very error prone, I will add additional details with regards to the PFA teflon liner sealing procedure, especially so that a new graduate student coming into Young Lee's group might have a better chance of replicating it.

1. The first step is to cut off a piece of PFA teflon tubing from our large spool. This will be cut again, so typically you want to cut off a generous amount that is going to be longer than the final length. For most of the Zn-Barlowite growths, the calibrated length of the Lee lab's furnaces is 12 in, so this is the final length one should shoot for. Hence one should cut off 18-20" of PFA teflon in the first step (i.e. about 6" more than the intended final length).

   (a) The next step is to seal the first end of the Teflon tube. This is done by lining up an impulse sealer in the lab about a quarter of an inch from one open end of the tube. Then, you want to firmly press down on the sealer with the heat turned on to its maximum setting. The sealer will time out after a few seconds. When this happens you need to

immediately raise the sealer a bit to reset it (you will hear a small click). Then you want to quickly press down again on the Teflon sealer. The goal here is to essentially bypass the safety mechanism of the Teflon impulse sealer.

(b) Repeat this process of rapidly overheating the impulse sealer. After about 5-15 repetitions, you will eventually notice a strange smoke coming off of the PFA. This is good, this means the sealing has commenced. For obvious reasons, you also want to do this in a fume-hood with the sash lowered as much as possible so you can avoid breathing in toxic fluorocarbons and giving yourself cancer later in life. When the smoking begins, you want to do one last press and hold to really mechanically force in the seal. Press down on the handle as hard as possible and directly over the point of the tube sealing. Note that this is more of a technique than strength thing. If you properly align your body, you can lean over the sealer with your entire body weight, rather than engaging your relatively weak biceps, which exerts less force than our body weight (for the vast majority of us).

(c) If you did a good seal, then the PFA should be stuck to the Teflon liner of the impulse sealer, which would've melted on-to it. This is great! Then just carefully pick the liner from the sealer with a tweezers, trying to maximize the amount of Teflon that goes with the tube for a solid seal.

(d) One thing to note is that this process obviously destroys the impulse sealer rather rapidly. Generally, over several uses, you'll want to make sure you're sealing on a "fresh" part of the sealer, which is usually virgin and not blackened. If the entire length of the Teflon liner is black, this can be replaced, and replacement liners can be found next to the sealer in our lab. I generally find that each fresh liner is good for about 10 seals before they need to be replaced. Likewise, this process also destroys the heating element, which typically needs replacement about every 20 seals (i.e. replace with every other Teflon liner replacement). The heating elements are shipped alongside replacement liners. Replacement liners can be found here (and you can also look on the group ordering sheet). Every once in awhile, it seems that the entire sealer will be destroyed by this process, and you can order new ones here.

In general, we are obviously pushing the Teflon sealers beyond their design limits here. If you are a new graduate student to the group, and are planning to embark on many growths, it might be worth considering asking to upgrade our system to a higher temperature one that is designed to seal Teflon. These are available here and here. Generally, these dedicated Teflon sealers are intended for industrial use and tend to cost $5,000 USD and up. For comparison, our impulse sealers cost about $ 225 USD a piece, so they are much cheaper, even with frequent replacement. That being said, these growths have a success rate of only about 40% in my experience, with the most frequent failure mode being a Teflon seal that doesn't hold. Hence, if you are doing a lot fo these, it might be

very beneficial and cost-effective to upgrade this system in the long run.

(e) One final note for this incredibly involved subsection. There is a second technique I have been trying to develop which involves sealing the PFA tube to a PFA teflon plug that fits inside of the tube. As I will visit later in this manual, this could provide a better seal, in addition to making the liner fit in the quartz tube better. One disadvantage of this currently described sealing technique is that this seal necessarily expands the width of the Teflon from its diameter "D" to half of its circumference, $\frac{\pi D}{2} > D$. This means it has to bend when being stuffed into the quartz tube, which can also lead to failures. Alternatively sealing with a plug would alleviate this issue. The main issue with this technique currently is that I can't find an appropriate size of PFA rod that can be ground down to fit inside the PFA tubing. I have bought 12mm diameter PTFE Teflon rods, but these don't seem to seal to PFA well enough to hold a vacuum. This is an open area for development of this technique though!

2. Phew! With all of this being said, the next step is to create a double seal, right next to the first one. Generally, you want this seal to be close to the first, without overlapping. About 1/16" or so is ideal, and your eye for lining this up will get better over time. I have found that the double seal significantly improves success rates of the seal holding.

3. After double sealing, pour your powdered mixture into the Teflon tube. Alternatively, if pre-reacting in the tube itself, you'll want to just dump in the reactants here. Generally, I feel like success rates are higher when pre-reacting in a Teflon-lined Parr-bomb to make powder. This is primarily because pre-reacting in the tube itself can cause the powder to "clump" inside of the tube that makes it difficult to later set up the hydrothermal furnace. That said, I really haven't done enough growths to test this beyond superstition, and indeed, one of my best growths did come from a tube pre-reaction. The best course of action may even depend on what crystal you're trying to grow. So in general, I'd recommend a bomb pre-reaction, but this variable might be worth playing with as well. The rest of this guide will follow the bomb pre-reaction for the most part, with notes for a tube pre-reaction included as sidebars where appropriate.

4. Next, you'll want to make a Sharpie mark 12" above your innermost double seal. This is where your second seal is going to go.

5. Next, you'll want to freeze the pre-reacted powder in liquid nitrogen. As Teflon is flexible, you can do this quickly if you want.

6. The next step is to vacuum seal the tube. Generally, we do this with our tube sealing assembly. I tend to like to add the O-ring directly to the tube while sealing so that I can transfer to the

station quickly with minimal melting. Then, the sealing should commence to get the vacuum down to about 10^{-2} torr. This sealing process will flatten the flexible Teflon to be mostly flat.

7. Once vacuum is reached, you'll want to pinch at the top as hard as possible to maintain the vacuum. Then, run this over to the impulse sealer as fast as possible to avoid leakage. Then, use the above steps to seal on the mark. Ideally, the tube will stay flat below the seal in this process.

8. Like before, you'll want to double seal the top. Depending on how the first seal goes, you might also consider re-freezing the solution before doing this. Make sure you cut off any excess length from the top to get your final 12" Teflon liner as well

   (a) This step is one of the most failure prone in the entire process. In this step, you need to shove the Teflon liner into a quartz tube. The thin-walled Teflon liner has an outer diameter of 11.8 mm, whereas the inner diameter of the quartz tube is 12 mm. This will be an incredibly tight fit, and you will be fighting friction, even with the characteristically slippery Teflon.

   (b) Note that you generally will want the quartz tube to be about 18 inches in length an pre-sealed on the bottom before beginning the stuffing procedure. Please ask a senior lab member for details on sealing the bottom of the quartz tube.

   (c) To start this procedure, you will need to fold the Teflon tube in on itself so that the wide seal can fit inside the quartz tube. Generally, the Teflon liner will pucker in this process and it will return to its natural diameter over 1-2 inches of length. Shove this down until you reach the second seal. This process usually isn't too bad.

   (d) Pucker the second seal like the first one, and shove into the tube. Once the Teflon is fully inside the quartz, it will still need to go down about another 4" due to the design. This tends to be the most difficult part. To do this, you'll want to take a narrow metal rod from the lab and push on top of the seal (ideally). Once you get it moving, don't let up! Remember that kinetic friction is less than static friction, so you can minimize the force and stress on the tube by overcoming this force only once!

   (e) Often, this process will bend the top before you get the Teflon to the bottom. Play around with different diameter ram-rods, and pushing locations. If you really can't move it, taking a wider ram-rod and pushing on the pucker point of the sealer tube usually works. This should be a last resort though, especially since the Teflon liner is only about 0.1mm thick. I have ruptured the liner in this process before. Overall just be patient and persistent. This part is the hardest, but it is also very possible.

   (f) In hindsight, I have several ideas for improvements on this step. If I were to re-order everything from scratch, I would've ordered a 11.25-11.5 mm outer diameter Teflon liner

tubing with a thickness of 0.2 mm instead of 0.1 mm. The shorter outer diameter would help this part of the procedure a lot, and PFA expands to heat anyways, so I don't think it would affect the lining that much. Meanwhile, the thicker PFA would make ruptures less likely. The current spool of Teflon was custom ordered for about $ 1,000 USD, with the minimum order length unfortunately being 1000 ft, which is comically an order of magnitude more than we need. Another consideration for this might be custom ordering PFA Teflon rods to completely remove the puckering. Ordering a new dedicated Teflon sealer might also be synergistic with the thicker-walled PFA liner too. Especially since we're pushing these sealers to the limit, the thicker PFA might be even harder to seal properly.

9. The last step is to put a 12mm quartz rod inside the quartz tube. Let it slide down the length and rest on top of the Teflon liner. Then, you'll want to freeze the whole assembly. Note this time, you'll have to lower it slowly, so that the quartz doesn't crack. Again, you'll want to add the O-ring and gasket to the tubing assembly here, so it is ready for a quick transfer to the sealing station.

10. When hooking the assembly up to the tube vacuum sealer, open the valve slowly. Often, the rod fits so tightly in the quartz tube that it will fly up when you pull vacuum. If you open it all the way, it can fly in with force, which might damage the sealing assembly. So be patient, and increase the vacuum in increments.

11. Once you have the vacuum wide open, you're ready for the final step! Here, you'll want to make a methane-oxygen torch as hot as possible (again, ask a senior graduate student for help with this). Then, you'll want to seal the top of the quartz plug to the quartz tube while pulling vacuum. The tricky part is that quartz melts at about 1700 C, while PFA melts at about 300 C. If you aren't careful, you can end up melting the PFA and ruin the liner! To avoid this, you generally want to angle your torch up while you seal the top of the quartz plug. One benefit you have is that quartz in a notoriously bad thermal conductor, so the 2" of leeway tends to be enough to do about 10 minutes or so of heating work. This is also why the original quartz tube was made to be 18", so that you have 2" of leeway to not point the torch too closely into the sealing assembly.

12. As you seal the quartz tube to the plug, make sure you seal on all sides. And yes, while sealing the backside, you will have to point the torch right at yourself, which is a bit scary. Please do this with supervision. Generally, you can tell that the top seal is good when the quartz tube melts around the plug and gets pulled up a little bit by the vacuum (i.e. the quartz tube will shrink a bit in diameter right above the plug. Try to make the rod-tube seal at least a quarter inch large. The bigger the better, obviously, and if you aren't careful, an insufficient seal can explode when heated up in the oven.

13. With this, dremel off the excess quartz tube length and you are done!

14. One final note is that our final tube length is 14" and our furnaces are calibrated over a length of 12". This is fine, you'll just want to make sure you align the 12" of internal space in the quartz tube with the 12" of the furnace that are calibrated, letting the plug stick into the uncalibrated zone.

15. Another closing note is that you'll want the pre-reacted powder to all be at the "hot" end of the zone furnace when you turn it on. Often the puckering can cause a certain percentage of the powder to get stuck at one (or both) ends of the tube. Sonication and vigorous shaking can help... It's a bit of a superstition of mine, but my best growths seem to have about half of the powder "stuck" at one end. My best guess is that this helps the feed rate to the cold end be a bit slower, such that crystals can nucleate and form at an ideal rate. Maybe more investigation needs to be done with regards to the ideal amount of pre-reacted powder, and how to best get powder unstuck from the ends

Measurement Details The development of a new synthesis method for Zn-barlowite, discussed in the previous section, yielded the first large, high-quality single crystals of this material [12, 20, 21]. These crystals are up to 5×5×0.1 mm in size and are fully deuterated to reduce incoherent background. This enabled the most ambitious neutron experiment on Zn-barlowite to date. A total of 190 crystals were co-aligned into a 0.76 g mosaic, with a precision of about 3 degrees, which was verified by Laue Diffraction. This effort was essential: only with such a sample mass and alignment was it possible to probe the subtle magnetic excitations of Zn-barlowite with sufficient resolution at the Cold Neutron Chopper Spectrometer (CNCS) at Oak Ridge National Laboratory [22].

Measurements were performed primarily with an incident energy of $E_i = 3.32$ meV and a base temperature of $T = 1.7$ K, allowing high-resolution mapping of the dynamic structure factor $S(\mathbf{q}, \omega)$. Additional data were collected at higher temperatures ($T = 40$ K and $T = 150$ K) to examine the thermal evolution of the excitation spectrum and to perform detail balanced background subtraction which will be outlined later in this section. The reported neutron data were collected using the CNCS spectrometer at Oak Ridge National Laboratory's Spallation Neutron Source. Spectra were measured at sample temperatures T=1.7 K, T=40 K, and T=150 K with incident neutron energy E_i=3.32 meV over 360° scans in the HK0 scattering plane. The chopper frequency used was 180Hz.

Sample Environment Background Subtraction In addition to scattering from the crystals, anything else in our sample environment can interact with the incoming neutron pulses and add background to our data. For this reason, two separate background measurements were performed; one with just an empty can of Helium and another on dummy aluminum sample plates coated with the same mass CYTOP as that of the true sample holder. This is a fairly standard neutron scattering procedure, but I still outline it in detail below as this is a thesis defense and not a paper.

To accurately separate and subtract background contributions from Helium and CYTOP from our data sets, we empirically estimate the shielding factor parameter. This is a factor that accounts for the effect of neutrons being shielded from the CYTOP by the sample itself, which means that the scattering counts in the raw dummy measurement will generally be higher than when the crystals are present, and generally needs to be scaled down before subtracting. For this reason, practical background subtraction for all temperatures is best approached with a detailed and analytic procedure. For each temperature at which we measured data, we made three measurements: One on the entire sample assembly – with the crystals, CYTOP adhesive, and Helium in the background, one on a "dummy" sample – a sample without crystals but with a nearly matching amount of CYTOP – and background Helium, and one with no sample in the beam path and only Helium. For clarity, we call these measurements, respectively, $\mathcal{M}[\text{Sample} + \text{He} + \text{CYTOP}]$, $\mathcal{M}[\text{He} + \text{CYTOP}]$, and $\mathcal{M}[\text{He}]$. We also let $\mathcal{D}[\text{Sample}]$ be our best estimate of the data only from the crystal sample. With this, we estimate the shielding factors as follows:

$$\mathcal{D}[\text{Sample}] = \mathcal{M}[\text{Sample} + \text{He} + \text{CYTOP}] - \beta\,\mathcal{M}[\text{He} + \text{CYTOP}] - (1-\beta)\mathcal{M}[\text{He}], \tag{3.1}$$

where β is a "self-shielding factor" parameter. Note that for all choices of β, the He signal is fully accounted for. This only changes the amount of the CYTOP-only signal that is subtracted from $\mathcal{M}[\text{Sample} + \text{He} + \text{CYTOP}]$ to estimate $\mathcal{D}[\text{Sample}]$.

Empirically, we find that the CYTOP signal is strongest in the elastic line: i.e. where there is zero energy transfer. Figure 3.3 shows this elastic signal from CYTOP integrated along the [H 0 0] and equivalent directions measured at T=1.7 K. It also shows $\mathcal{D}[\text{Sample}]$ estimated with various shielding factors. It is clear that in the $\beta = 0$ case the CYTOP is under-subtracted – as it is ignored completely – but in the $\beta = 1$ case there is over-subtraction of the CYTOP signal. By examining plots like these, we found choices for β that minimized CYTOP signals for all data sets. For T=1.7 K and T=40 K data, the best choice was clearly β=0.71. The noisiness of the T=150 K data made this parameter much harder to estimate, but it was chosen to be $\beta = 1.75$, although all values in the range $\beta \in [1.5, 2.0]$ seemed reasonable. Note that the dummy sample for the 150K background was taken in a slightly different geometry, which is why we have $\beta > 1$; normally physical constraints would govern $0 < \beta < 1$ for a dummy sample in the same geometry and the same amount of CYTOP.

Additional Elastic Background Unique to Zn-Barlowite Zn-Barlowite measurements are unique in that we are measuring the weakest possible magnetic moment (spin-$\frac{1}{2}$ Cu^{2+} ions) on a maximally frustrated antiferromagnetic lattice (the kagome lattice). While this is what could potentially lead to the exotic QSL magnetism, this also leads to rather weak and diffuse scattering. This means that we often encounter different and difficult backgrounds that would normally be too weak relative to the signal to be terribly important. We have, in fact, already encountered this theme in section 2.2.1 in this very thesis in processing the magnetic scattering of Barlowite II. Of

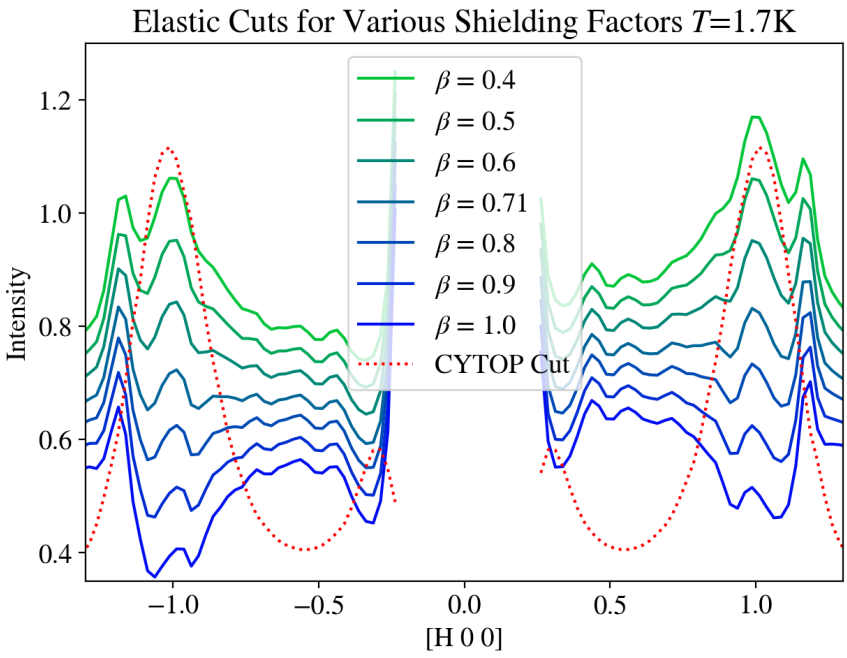

Figure 3.3: Averaged cuts along [H 0 0] and equivalent directions of the elastic scattering pattern – $\hbar\omega$ = [-0.1, 0.1] meV – for data processed with various shielding factors using Equation 3.1 applied to T=1.7 K data. Red dotted line shows this same cut for measured [CYTOP + He] data. The signature of the CYTOP is clear in the elastic data and a shielding factor choice of 0.71 appears optimal.

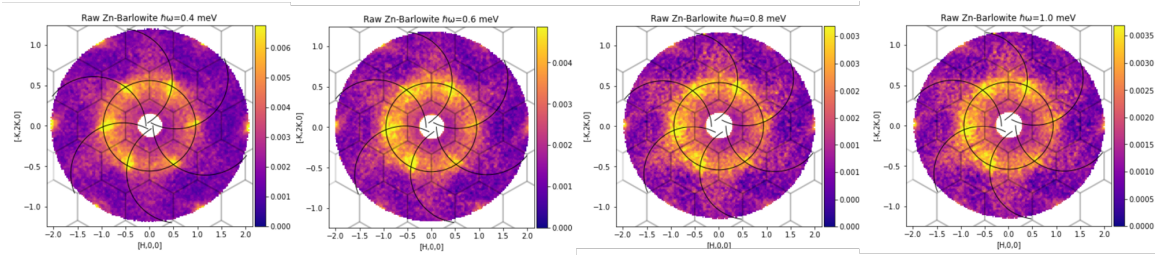

Figure 3.4: Raw data slices at various energies. The snaking arc features indicate the momentum data captured by a single detector bank at these energies. Meanwhile, the intersection of this with the circle indicates where elastic bleed into the sample should show up, as is derived in the remainder of this section.

course since Zn-Barlowite is even more frustrated, the situation is only exacerbated here.

Figure 3.4 shows what the raw CNCS data looks like before background subtraction. This shows strong scattering features near [1 0 0] and equivalent positions. These appear as "streaks" of a chiral nature and persist with subtractions of Helium and CYTOP backgrounds (regardless of shielding factor). It is of note that we can be 100 % certain that these chiral features are in fact an artifact, since this data was taken on a large crystal array; if there were truly chiral-like intrinsic magnetic behavior in our crystals, the data would include signals from both handed orientations due to the many crystal orientations in the large array. Due to their proximity to the bragg peak location, I correctly identified the origin as bleed in from the much stronger elastic scattering, which I derive in detail below. This is what allowed us to track the evolution of this artifact in Fig. 3.4 as is detailed at the intersection of the arcs and circles. This is one of the proudest achievements of my PhD and I think demonstrates my mastery of experimental design and analysis; even the beamline scientists were relatively ignorant to this background source.

To track this effect, we consider the time-of-flight scattering geometry of the CNCS instrument and the effects of the energy width of the incident beam. For a normal inelastic scattering event from an incoming beam of energy E_i, the detected $\mathbf{q}$ in units [Å^{-1}] is

$$\mathbf{q} = \mathbf{k}_f - \mathbf{k}_i = k(E_i)\left[\left(\sqrt{1-\frac{\Delta E}{E_i}}\cos\phi - 1\right)\hat{i} + \left(\sqrt{1-\frac{\Delta E}{E_i}}\sin\phi - 1\right)\hat{j}\right], \tag{3.2}$$

where ΔE is the detected loss in energy from the time of flight, $k(E)$ is the incident beam wavenumber, and ϕ is the angle between initial and final wave vectors (and equal to twice the Bragg angle, $\phi = 2\theta_B$). We now suppose the incident energy E_i is actually $E_i + \delta$, where δ is some deviation that may be positive or negative. From the time of flight geometry, we can calculate the effect of this

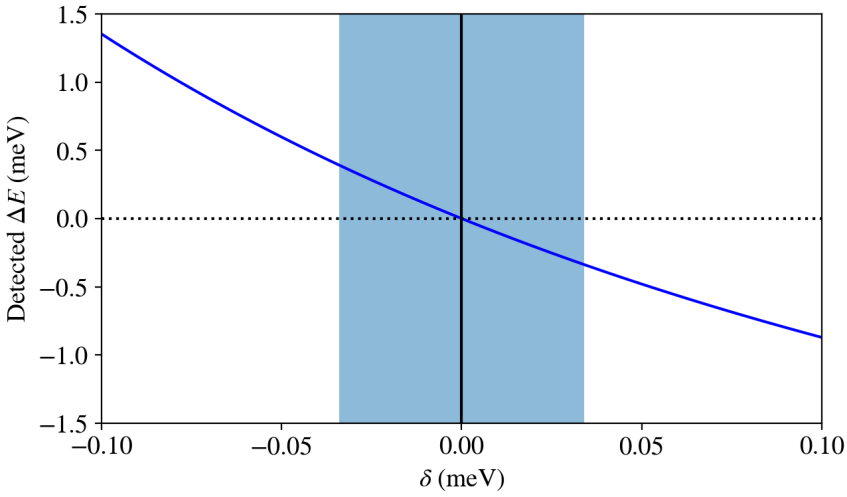

Figure 3.5: Detected ΔE as a function of incident neutron energy deviation δ according to Equation 3.3 given CNCS instrument geometry and incident neutron energy E_i=3.32 meV. The shaded region shows the reported FWHM for δ at the CNCS for the 180Hz DD-chopper frequency used in our experiments.

deviation δ on the detected ΔE from an elastic scattering event according to the function

$$\Delta E_d(\delta) = E_i \left[\left(\frac{d_1}{d_2} - \frac{d_1 + d_2}{d_2} \sqrt{\frac{E_i}{E_i + \delta}} \right)^{-2} - 1 \right]. \tag{3.3}$$

At the CNCS instrument, d_1=36.25 m and d_2=3.75 m. Figure 3.5 below shows this relationship and the FWHM of δ given our chosen incident energy and chopper speed. Note that it is nearly linear in our regime of interest.

Alone, Equation 3.3 accounts for the "bleeding" of elastic Bragg features into the inelastic signal, but does not explain the chiral nature of the artifacts. This quality comes from the combination of Equations 2 and 3, which shows that a non-zero δ also affects the detected $\mathbf{q}$ position of elastic scattering events. Specifically, an elastic Bragg scattering event that should be detected at

$$\mathbf{q} = k(E_i) \left[(\cos\phi - 1)\,\hat{i} + (\sin\phi - 1)\hat{j} \right] \tag{3.4}$$

is instead detected at

$$\mathbf{q}_d = k(E_i + \delta) \left[\left(\sqrt{1 - \frac{\Delta E_d(\delta)}{E_i + \delta}}\cos\phi - 1 \right) \hat{i} + \left(\sqrt{1 - \frac{\Delta E_d(\delta)}{E_i + \delta}}\sin\phi - 1 \right) \hat{j} \right]. \tag{3.5}$$

Using Equations 3.3 and 3.5, one can model and track how this process contaminates the detected

inelastic data; this is done across energy in 3.4. The intersection of the $\mathbf{q} = 0$ centered circle and thearcs show where the strongest signal from Bragg peaks themselves appears and the arcs follow the streaking caused by the variance in δ. In the figure chiral artifacts from [2 0 0] equivalent Bragg peaks also appear, but these are not tracked.

Advanced Helton Background Subtraction of Elastic Artifacts Following this step, we used a background subtraction technique introduced by Helton et al. [23]. This approach takes advantage of the oddness of $\chi''(\omega)$ with respect to ω and the fact that $S(\mathbf{q},\omega) = [1 + n(\omega)]\,\chi''(\mathbf{q},\omega)$, where $n(\omega)$ is the Bose occupation factor. Since the time of flight based CNCS spectrometer measures scattering events that both transfer energy to and from the crystals (positive and negative energy scattering events respectively), we can exploit this oddness to clean the data of all temperature-independent background features. With data taken at two temperatures T_{L} and T_{H} the method can be described by the equation set

$$\begin{aligned} S(\mathbf{q},+\omega,T_{\mathrm{L}}) =& S(\mathbf{q},+\omega,T_{\mathrm{L}}) - S(\mathbf{q},+\omega,T_{\mathrm{H}}) \\ &- \frac{1+n(\omega)}{1+n(-\omega)}[S(\mathbf{q},-\omega,T_{\mathrm{L}}) - S(\mathbf{q},-\omega,T_{\mathrm{H}})], \\ S(\mathbf{q},+\omega,T_{\mathrm{H}}) =& S(\mathbf{q},-\omega,T_{\mathrm{L}}) - S(\mathbf{q},-\omega,T_{\mathrm{H}}). \end{aligned} \tag{3.6}$$

As is detailed in Fig. 3.4, the largest parasitic background in our measured inelastic data arises from elastic brag peaks "bleeding" into the inelastic data due to the finite energy width of the beam; this effect is especially prominent at low energy transfers. However, as the elastic Bragg Peaks are nearly temperature independent in strength, this method yields magnetic scattering dominated $S(\mathbf{q},\omega)$ data sets at two temperatures.

Final Data Processing Touches Finally, the data underwent D_6 symmetrization, yielding sets on which all analyses were performed. Fig. 3.6 in the Extended Data shows these processing steps for the T=1.7 K dataset.

3.2 Results and Analysis

Observation of a Broad Continuum of Magnetic Excitations

The most striking feature of the Zn-barlowite data is the presence of a broad, nearly energy-independent continuum of magnetic excitations extending up to at least 3 meV, as is shown in Fig. 3.7. Another visualization for this can be seen by taking full momentum slices at different energies, and this is shown in Fig. 3.8. This type of diffuse scattering is widely regarded as the "smoking gun" signature of a quantum spin liquid (QSL) [24, 25, 3]: it suggests that the $S = 1/2$ spins on the kagome lattice are not forming conventional magnons but are instead fractionalizing

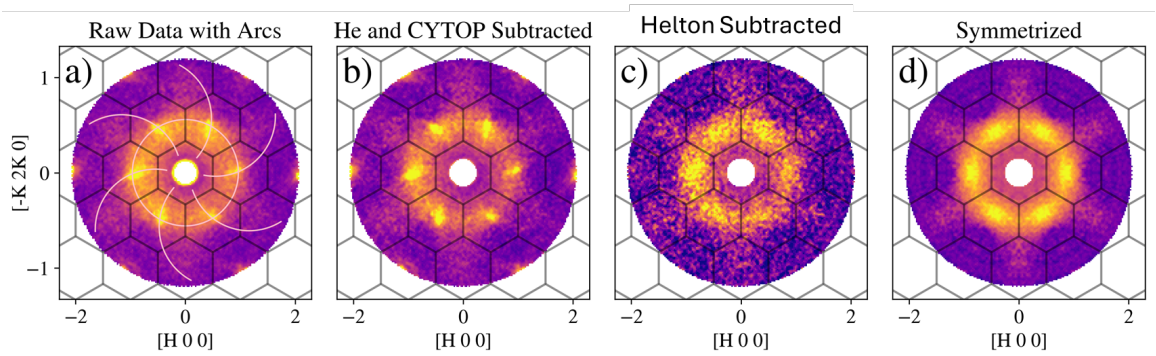

Figure 3.6: Steps to process inelastic neutron scattering for analysis. (a) Raw scattering data at $\hbar\omega = [0.3, 0.5]meV$ with T=1.7 K and incident neutron energy E_i=3.32 meV. Parasitic arc-like chiral features stemming from elastic line Bragg peak bleed into the inelastic data are highlighted at the intersection of the light-pink curves overlayed on the data. (b) Data after subtraction of He and CYTOP backgrounds with an empirically-determined shielding factor. (c) Removal of temperature-independent background using the Helton Background subtraction technique. (d) Data after D_6 symmetrization, yielding sets on which analyses are performed. FIG.

into spinons, which carry spin-1/2 but no charge [5]. Also of note is that the spin scattering spectra is minimally affected by a shift in temperature from T=1.7 K to T=40 K, with the main difference being in the low energy intensities less than ≈1 meV. As we shall explore shortly, this low energy scattering is likely due to the magnetic impurities in the system [13], which are far more likely to be affected by this temperature shift. In contrast, T=40 K would only correspond to about $T \sim J/5$ in comparison to the exchange energy in the kagome lattice, which is why the higher energies aren't affected as much.

Comparisons to Herbertsmithite — the prototypical kagome QSL [23, 11] — immediately revealed both *striking similarities* and *important differences*. This is noted outlined in Fig. 3.9. At higher energy transfers (for instance, $\hbar\omega \approx 1.3$ meV), the scattering patterns of Zn-barlowite and Herbertsmithite are qualitatively indistinguishable; this is shown in panels (c) and (d). Empirical modeling suggests that this momentum-dependent scattering around high-symmetry positions is primarily due to correlations within the kagome plane itself. This provides strong evidence that both of these scattering patterns are a result of universal kagome layer physics between the two materials [2]. It also greatly strengthens the case to be made that both of these materials do, in fact, host a kagome QSL state [24].

At lower energy transfers ($\hbar\omega \approx 0.4$ meV), however, the scattering patterns diverge, as is shown in panels (a) and (b) of Fig. 3.9. In Zn-barlowite, one observes intensity variations along the (1,0,0) and (1,1,0) directions that are absent in Herbertsmithite. This low-energy discrepancy is not unexpected: it stems from structural differences in the two materials [13]. While Herbertsmithite's interlayer Cu^{2+} impurities occupy highly symmetric sites directly above and below the kagome

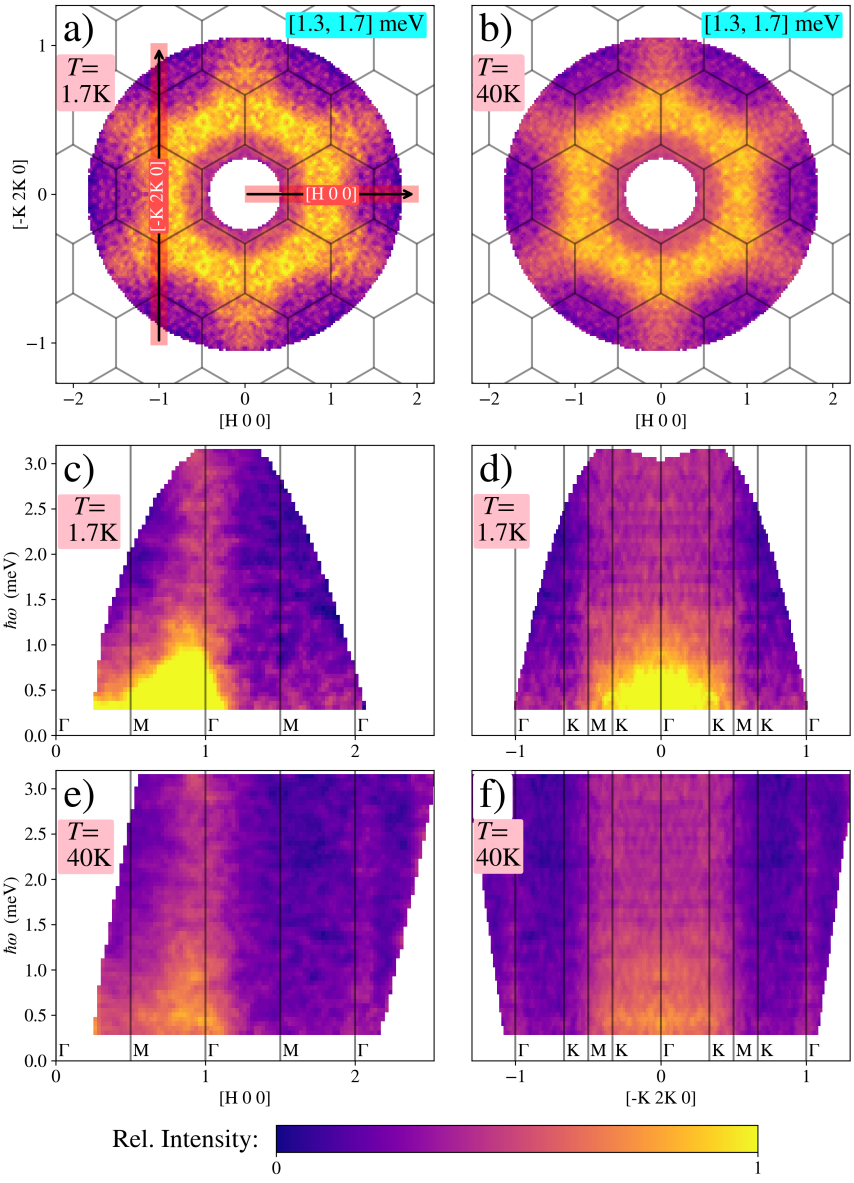

Figure 3.7: **Spin excitation continuum in Zn-barlowite, highlighting its relative independence on energy transfer and robustness to changes in temperature. This is a signature hallmark that strongly supports the existence of a quantum spin liquid ground state with diffuse magnetic excitations of spinons. (a, b)** Inelastic scattering pattern integrated over $\hbar\omega$=[1.3, 1.7] meV at T=1.7 K (a) and T=40 K (b). **(c-f)** Momentum-integrated scattering over regions indicated by red boxes in (a) at T=1.7 K (c, d) and T=40 K (e, f). Data shown were all taken with incident energy E_i=3.32 meV. (a, b) share a common intensity scale as do (c-f).

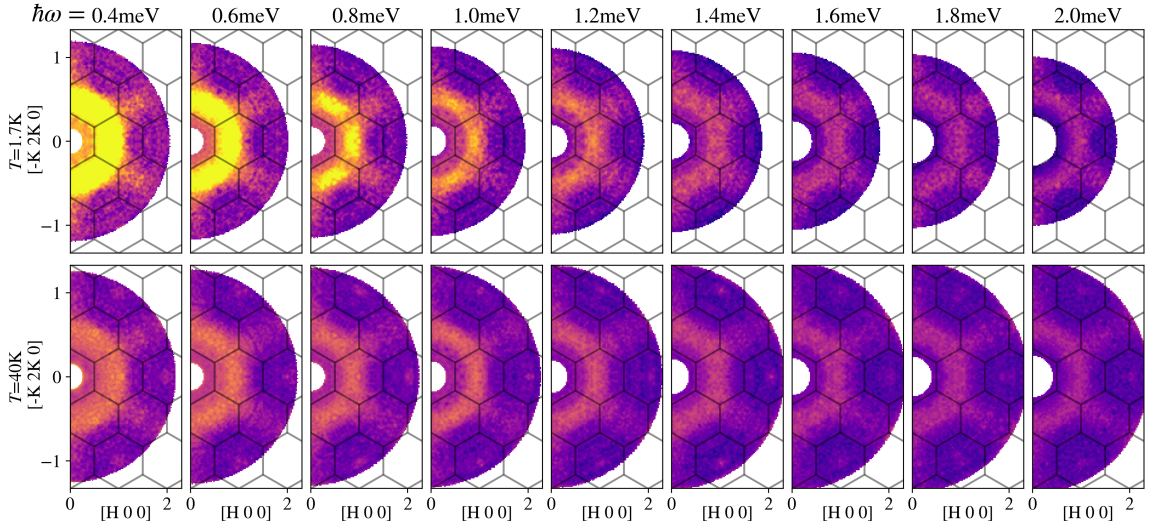

Figure 3.8: Energy Slices at T=1.7 K and T=40 K, showing the progression of scattering in momentum space across energy

hexagons, Zn-barlowite's residual Cu^{2+} impurities sit in off-centered, lower-symmetry positions. In Herbertsmithite, this scattering pattern can be modeled as arising primarily from antiferromagnetic correlations between neighboring impurity sites [2]. In contrast, in Zn-Barlowite, the modeling suggests that this scattering is a result primarily of ferromagnetic correlations between the impurity sites and the kagome layer [21]. Both of these correlations are self-consistent with what we would expect from the fully ordered Cu^{2+} analog materials as well (Atacamite and Barlowite) [10]. In barlowite, this ferromagnetic correlation is drives a Jahn-Teller distortion that leads to long range magnetic order in the kagome lattice. It seems likely that this correlation is somewhat preserved here, but does not lead to ordering, instead incorporating itself into the kagome wavefunction itself. We will explore this modeling in more detail shortly.

Role of Impurities in Zn-Barlowite and the Need for Separation

One of the central challenges in studying kagome quantum spin liquid candidates is that no real material is perfectly clean. Both Herbertsmithite and Zn-Barlowite suffer from a small but non-negligible population of Cu^{2+} "impurity" spins occupying the nominally non-magnetic interlayer Zn^{2+} sites [2, 13]. These impurities are magnetically active and weakly coupled to the kagome planes. As a result, they introduce low-energy excitations and additional scattering intensity that are not representative of the intrinsic kagome physics we wish to probe.

In Zn-barlowite, this effect is especially nuanced: unlike herbertsmithite, whose impurities sit symmetrically above the kagome hexagons, Zn-barlowite's impurities occupy lower-symmetry positions, changing how they interact with the surrounding spins [21]. This structural difference

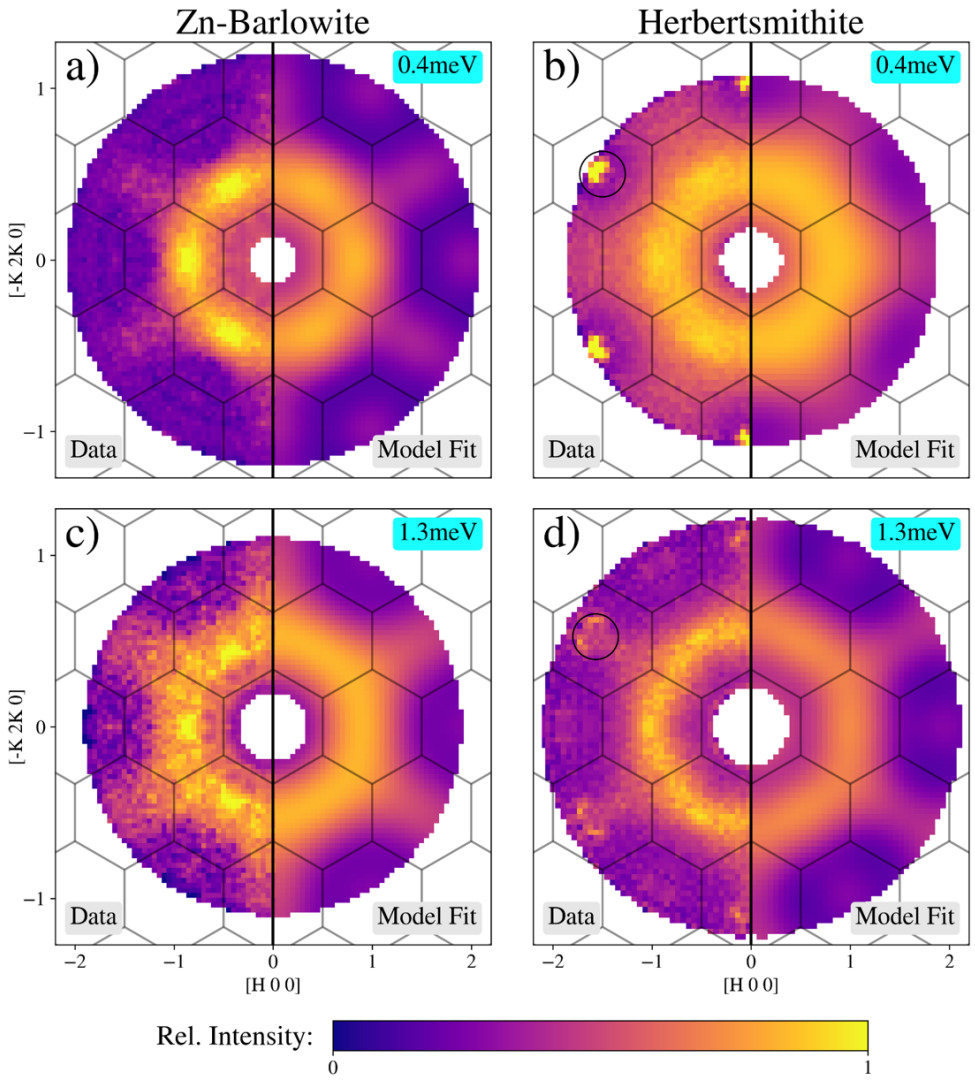

Figure 3.9: **Comparison of magnetic excitations between candidate kagome QSL materials, showing universal behavior, with distinct low-energy impurity-related scattering. (a-d)** Comparisons between measured and modeled magnetic neutron scattering intensity for Zn-barlowite (a, c) and herbertsmithite (b, d) [2] for energy transfers of $\hbar\omega$=0.4 meV and $\hbar\omega$=1.3 meV, respectively (see the Spin Correlations and Numerical Comparisons section). Black circles in b and d indicate scattering from phonons or tails of the Bragg peak intensity near the [1 1 0] positions, which are not captured by the magnetic model. All data shown were taken with incident energy E_i=3.32 meV and T=1.7 K. Zn-barlowite data was taken at the Cold Neutron Chopper Spectrometer at Oak Ridge National Laboratory and contours in (a, c) are respectively integrated over [0.3,0.5] meV and [1.2,1.4] meV to match the resolution of the data from Han et al. [2].

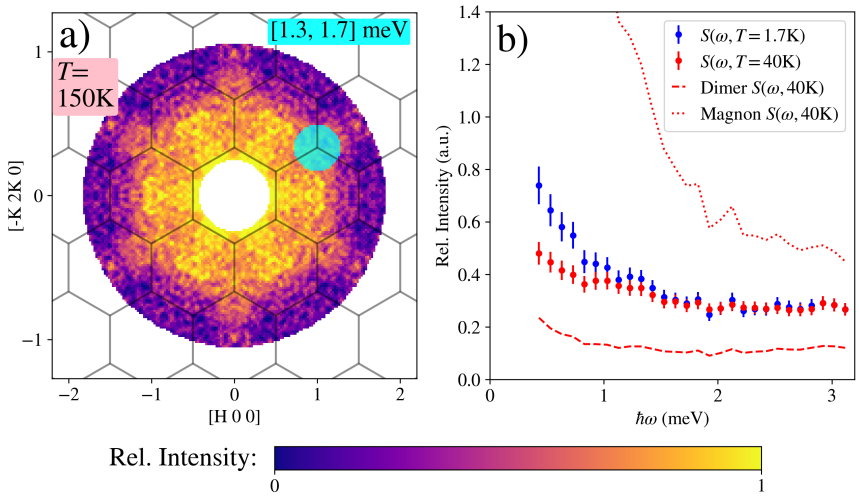

Figure 3.10: **Temperature dependence of spinon excitations. (a)** Inelastic scattering pattern integrated over $\hbar\omega$=[1.3, 1.7] meV at T=150 K showing persistent star-shaped scattering. **(b)** Energy dependent magnetic scattering intensity integrated over the cyan-highlighted **q**-region in (a) for sample temperatures T=1.7 K and T=40 K. Error bars for T=1.7 K and T=40 K are statistical counting errors. Line plots show estimated scattering for T=40 K based on the T=1.7 K data scaled by statistics for different models: (dashed) a dimer model with a singlet ground state and triplet excited state; and (dotted) those associated with magnons. Both are shown to diverge from the observed data.

manifests as distinct intensity variations at low energies, most visibly below ∼1.2 meV.

For this reason, separating the impurity-driven scattering from the kagome-plane scattering is not just a technical detail but a scientific necessity. Without this separation, one could mistakenly attribute impurity excitations to intrinsic kagome physics or overlook subtle features such as a spin gap [11]. Impurity contributions are the largest cited reason for those that still doubt if Herbertsmithite and Zn-Barlowite host a QSL state [24]. Much of the subsequent modeling in this chapter — including the empirical bond-correlation fits and the gap analysis — is motivated by the need to clearly delineate these two contributions.

Temperature Dependence and the Robustness of Kagome Excitations

To test the resilience of the kagome spin liquid state, we collected data at elevated temperatures of 40 K and 150 K, as is shown in Fig. 3.10. Remarkably, the higher-energy continuum ($\hbar\omega \gtrsim 1.2$ meV) persisted with only modest intensity loss even at $T = 150$ K. This means that the short-range kagome correlations that give rise to the spinon continuum remain intact up to a significant fraction of the exchange constant J (on the order of $J/5$ or more) [5].

In contrast, the low-energy spectral weight below ~ 1.2 meV displayed noticeable temperature dependence (panel b), consistent with the picture that this part of the spectrum is dominated by weakly bound impurity spins [2]. As these loosely coupled moments are thermally activated, they

gradually decouple from the kagome network, explaining the evolution of the low-energy scattering profile with temperature.

Finally, we note that the thermal evolution of the scattering shown in panel (b) does not follow the statistics of any classical magnetic excitation model well, such as that which would arise from magnons. This provides further evidence for the existence of the exotic QSL state in these materials, which have been predicted theoretically to instead host exotic quasi-particles like anyons, which would in principle have strange thermal statistics [26].

3.3 Analysis

Separating Kagome and Impurity Contributions via an Empirical Model

To move beyond qualitative impressions and rigorously quantify which parts of the scattering arise from intrinsic kagome correlations versus impurity-driven effects, we adopted an empirical bond-correlation model [2]. In this framework, the magnetic scattering intensity is written as:

$$S_{\mathrm{mag}}(\mathbf{q},\omega) \approx \alpha(\omega)|F(\mathbf{q})|^2 \left[1 + 2\sum_i \rho_i(\omega) f_i(\mathbf{q})\right], \tag{3.7}$$

where $|F(\mathbf{q})|^2$ is the Cu^{2+} magnetic form factor, $\alpha(\omega)$ captures the overall energy-dependent scattering strength, and $\rho_i(\omega)$ represents the spin-spin correlation strength across bond type i. The functions $f_i(\mathbf{q})$ encode the Fourier transforms of each bond type's geometry [5].

As is detailed in panel (a) of Fig. 3.11, We included the six shortest bond types in Zn-barlowite:

- the three shortest kagome–kagome bonds (nearest, second-, and third-neighbor);
- the two shortest impurity–kagome bonds; and
- the impurity–impurity bond.

The individual contributions from each $f_i(\mathbf{q})$ are shown in Fig. 3.12.

By fitting this model across energy slices, we extracted the energy dependence of the pairwise correlations.

Key Correlation Results

- *Nearest-neighbor kagome correlations* are strongly antiferromagnetic across the entire measured energy window, as is shown in Fig. 3.11 (c). This confirms the dominance of nearest-neighbor AFM exchange in Zn-barlowite. This exchange was expected from other previous measurements [12, 21].

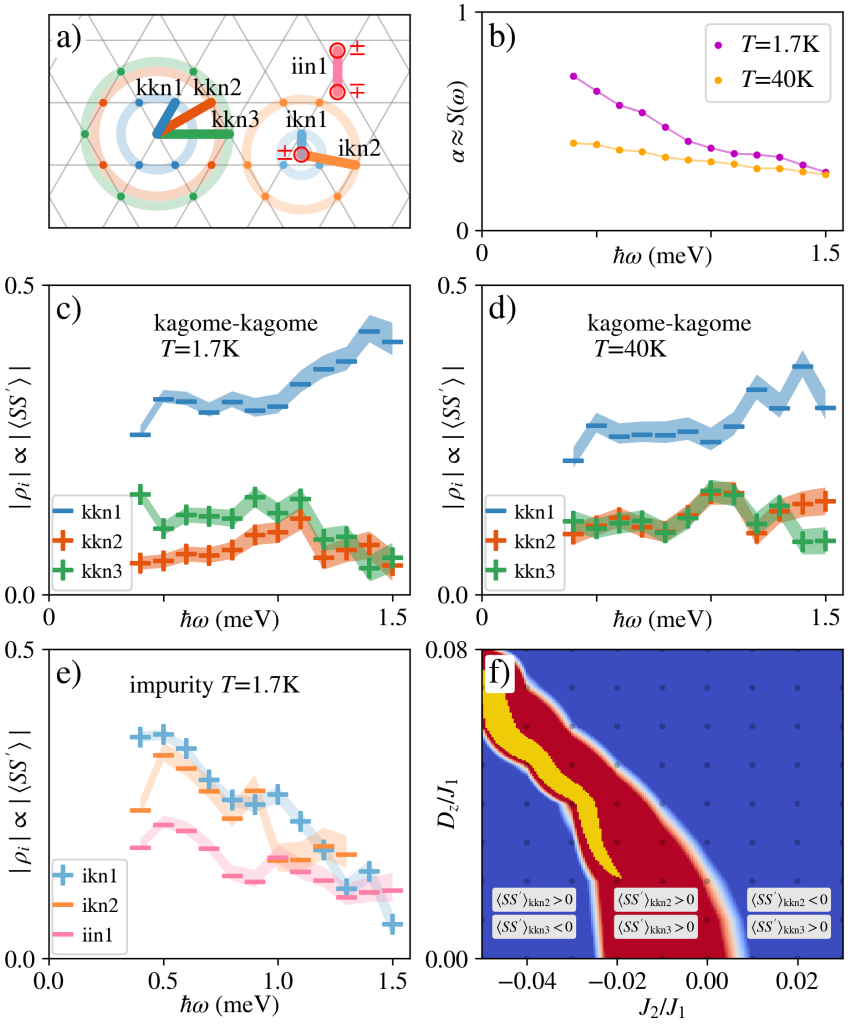

Figure 3.11: **Extracted pair-wise spin correlations over energy and temperature. (a)** Illustration of bond directions over which we report estimated correlation signals. Red circles indicate impurities with ± indicating their c-axis displacements from the kagome plane. **(b)** Fitted parameter $\alpha(\omega) \approx S(\omega)$ for T=1.7 K and T=40 K with standard errors, which correlated well with the overall scattering intensity at each energy. (c, d) Fitted relative correlation parameter $\rho(\omega)$ for three nearest kagome-kagome bonds for T=1.7 K and T=40 K. Here, AFM correlations are denoted with a "−" symbol and FM with a "+" symbol. (e) Fitted $\rho(\omega)$ for three nearest impurity-involved bonds for T=1.7 K data. (f) DMRG results for second and third nearest-neighbor correlations. Red region indicates parameter space where both are positive, consistent with fitted $\rho(\omega)$ signs. Yellow region indicates parameter combinations that most closely match $\hbar\omega$=[1.3, 1.7] meV neutron data as described in the text. Reported errors in (b-e) reflect standard errors from parameter fits. See Methods and Supplementary Information for details.

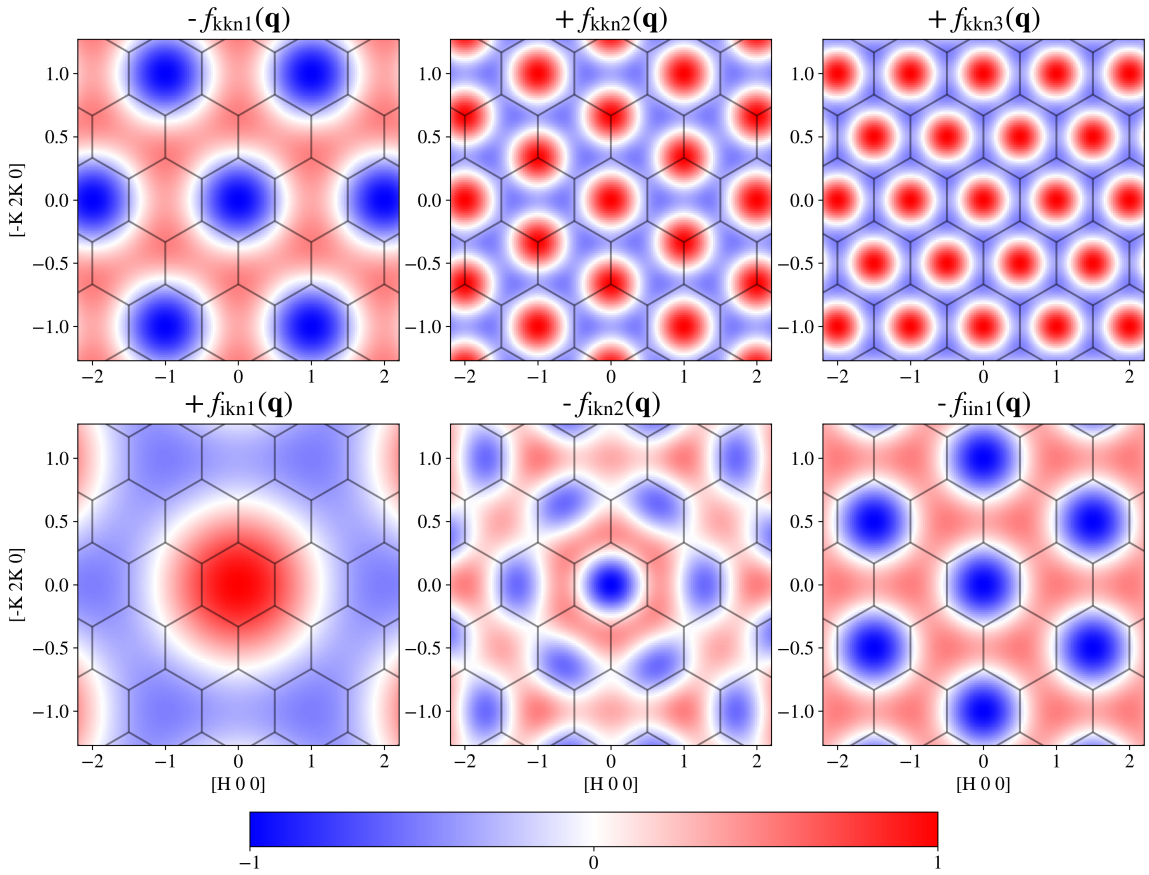

Figure 3.12: Figure showing the individual $f_i(\mathbf{q})$ components of the empirical model detailed in equation 3.7. Each of these components corresponds to a scattering contribution arising from magnetic correlations between specific bonds. The correspondance of these labels to the physical bonds in Zn-Barlowite is shown in Fig. 3.11

- *Second- and third-neighbor kagome correlations* are weaker and ferromagnetic. This combination deviates from the patterns expected for classical ordered kagome states (such as the $q = 0$ or $\sqrt{3} \times \sqrt{3}$ states) and is instead consistent with a disordered QSL ground state, especially as no classical analog can be drawn [24].

- *The largest impurity correlation* is a ferromagnetic exchange between the impurity moment and its nearest kagome layer moment, as is shown in Fig. 3.11 (e). This exchange is also expected from other modeling and the static order observed in Barlowite [21].

- *Impurity-involved correlations* fall off rapidly with energy and become negligible above $\sim$ 1.5 meV. This corroborates the interpretation that the high-energy continuum arises entirely from the intrinsic kagome network, not from disorder physics [2].

Comparison to Theory

With these fitted correlations in hand, we compared the results to Density Matrix Renormalization Group (DMRG) calculations of the kagome $S = 1/2$ Heisenberg model with small perturbations [27, 28, 2]:

$$H = J_1 \sum_{\langle ij \rangle} \mathbf{S}_i \cdot \mathbf{S}_j + J_2 \sum_{\langle\langle ij \rangle\rangle} \mathbf{S}_i \cdot \mathbf{S}_j + \sum_{\langle ij \rangle} \mathbf{D}_{ij} \cdot (\mathbf{S}_i \times \mathbf{S}_j). \tag{3.8}$$

The results of this modeling are shown in Fig. 3.11 (f). The measured correlation pattern places Zn-barlowite in the "sweet spot" of the kagome phase diagram: the nearest-neighbor Heisenberg term J_1 dominates, while J_2 and D_z are small (less than $\sim$10% of J_1) but nonzero [29]. The sign and magnitude of these perturbations — a slightly ferromagnetic J_2 and a small positive D_z — act to stabilize the spin-liquid phase [24]. The yellow region in Fig. 3.11 (f) shows the DMRG parameters that are most consistent with the measured inelastic neutron scattering data at high energies where kagome contributions dominate.

3.4 Spin Gap Analysis

Determining whether the kagome quantum spin liquid in Zn-barlowite is *gapped* or *gapless* is not merely academic — it directly speaks to the underlying phase of matter [25]. A gapped QSL corresponds to a $\mathbb{Z}_2$ topological phase, predicted to host emergent anyons that could one day serve as building blocks for fault-tolerant quantum computation [26]. By contrast, a gapless (Dirac) QSL would imply fundamentally different excitations and stability criteria.

Evidence for a Gapped Spin Liquid

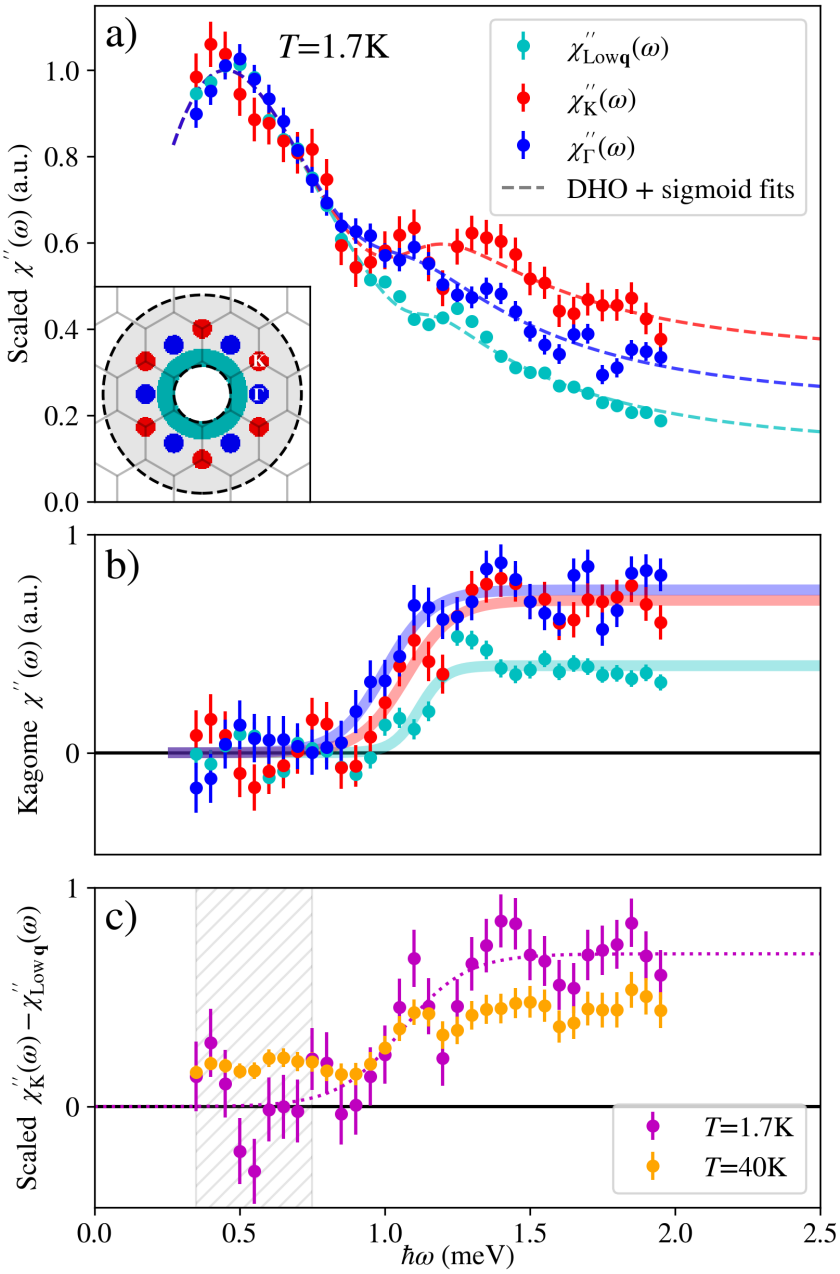

Figure 3.13: **Signature of a possible spin gap in intrinsic kagome spin excitations. (a)** Energy cuts of $\chi''(\omega)$ over various high-symmetry positions scaled and modeled as described in the text. Fitted function curves for each are shown as dashed lines. Inset shows integration regions inscribed by the q-region kinematically accessible at all reported energies. **(b)** non-normalized data from (a) with DHO component subtracted. Resulting sigmoid fits are highlighted showing similar widths and centers consistent with a 1.1(2) meV energy gap. **(c)** Subtractions of $\chi''_{\mathrm{K}}(\omega)$ from $\chi''_{\mathrm{Low}-\mathbf{q}}(\omega)$, where the latter is scaled such that the mean of the T=1.7 K data subtraction is zero at energies in the hatched region. Subtractions with this same scale are reported for T=1.7 K and T=40 K data along with a fitted sigmoid for the former. Error bars in (a-c) are propagated from counting statistics.

In Herbertsmithite, careful neutron and NMR studies suggest the presence of a small spin gap (≈0.8meV) [11, 2, 30]. Determining whether Zn-Barlowite shares this property required separating impurity scattering from intrinsic kagome scattering.

We applied the fluctuation–dissipation theorem to derive the imaginary part of the dynamical susceptibility, $\chi''(\mathbf{q}, \omega)$, and modeled the low-energy scattering as the sum of two contributions: a damped harmonic oscillator (DHO) for the impurity response and a sigmoid function for the kagome response [31]. The results of this analysis are shown in Fig. 3.13

Subtracting the DHO component from χ'' across multiple momentum regions consistently revealed a gaplike onset in the kagome scattering at $\Delta = 1.1(2)$ meV. Notably, the kagome layer correlations shown in Fig. 3.11 (c) also show an uptick at around 1 meV. This is also strikingly similar to Herbertsmithite [11] and provides compelling evidence that Zn-Barlowite, too, realizes a **gapped quantum spin liquid ground state**, especially when viewed in conjunction with the NMR results [32]. This experimental result will provide valuable information to theorists as they explore potential theoretical models for the QSL in this system.

3.5 Summary of Findings

The CNCS experiment establishes Zn-barlowite as one of the cleanest realizations of a kagome quantum spin liquid to date. The key takeaways are:

- A robust, nearly energy-independent spinon continuum, closely matching that of Herbertsmithite [5, 24].
- A clear separation between high-energy kagome excitations (universal) and low-energy impurity scattering (material-dependent) [2, 13].
- Extracted spin-spin correlations that are dominantly nearest-neighbor AFM with weaker ferromagnetic longer-range terms, consistent with QSL physics [27, 28].
- The presence of a ~ 1.1 meV spin gap, again mirroring Herbertsmithite [11, 32].

These results not only demonstrate the universality of kagome QSL behavior across Zn-Barlowite and Herbertsmithite, but also provide critical quantitative constraints for theoretical modeling of these exotic states [25, 24].

3.6 Out of Plane Data and Refined Modeling

The last section concludes what has been solidified, published, and peer reviewed in terms of knowledge about Zn-Barlowite. This section dives into promising directions for future research that will likely turn into future papers.

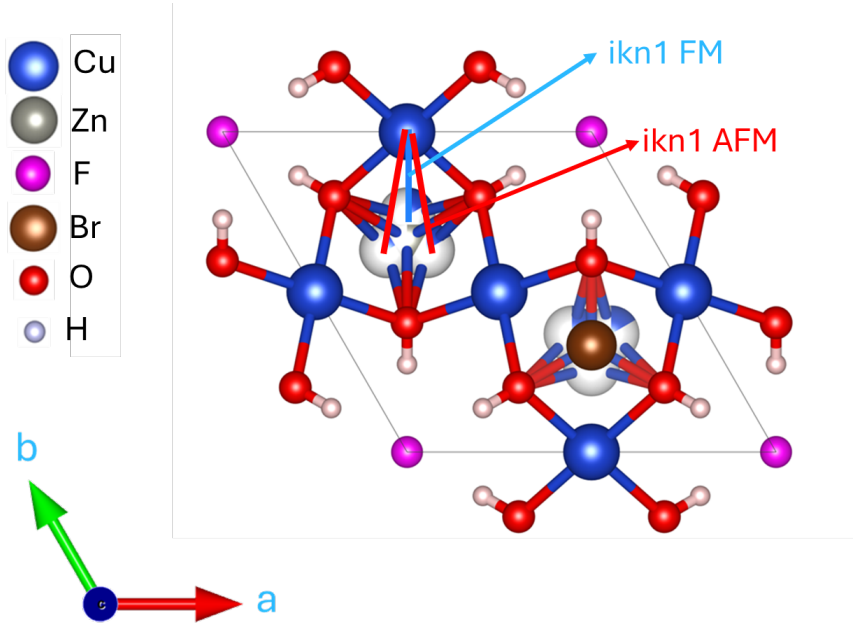

Figure 3.14: Illustration of the Jahn-Teller distortion of the interlayer Cu^{2+} sites. The interlayer copper moves of the center of the equilateral triange of the kagome lattice, and about 10% closer to the kagome layer site that it is ferromagnetically coupled to.

I begin this section by talking about a small refinement that can be made to the cosine correlation model. In Fig. 3.11 (a), an implicit detail is glossed over in refining the bond directions. This is that the impurity site is assumed to sit directly in the center of the equilateral Cu^{2+} triangle, just like it would if it was a Zn^{2+} ion. We know from detailed crystallography that this isn't the case though [1]; instead, the Cu^{2+} interlayer impurity will ferromagnetically couple to one of the neighboring kagome sites. This induces a subtle Jahn-Teller distortion, moving the interlayer impurity closer to the copper site that it is ferromagnetically coupled to. This distortion is significant–approximately 10% of the original bond length– and is detailed graphically in Fig. 3.14. In the figure, the short bond is labeled as ikn1 FM, and the longer bonds as ikn1 AFM. While the shortened bond is known to have a direct ferromagnetic exchange with the kagome lattice [1], the long bond is likely anti-ferromagnetically coupled simply by cross correlation, since the kagome layer sites are anti-ferromagnetically coupled with each other. That is to say, we'd expect the net correlation of these bonds to be antiferromagnetic even though the direct exchange energy is probably quite weak especially in comparison to the ferromagnetic exchange.

Since we are defining the Cosine model from a fourier-like transform of the real space lattice bonds, this deviance will affect the components of this model. Specifically, it will split the singular "ikn1" term into two "ikn1FM" and "ikn1FM" terms. The resultant model terms are plotted in

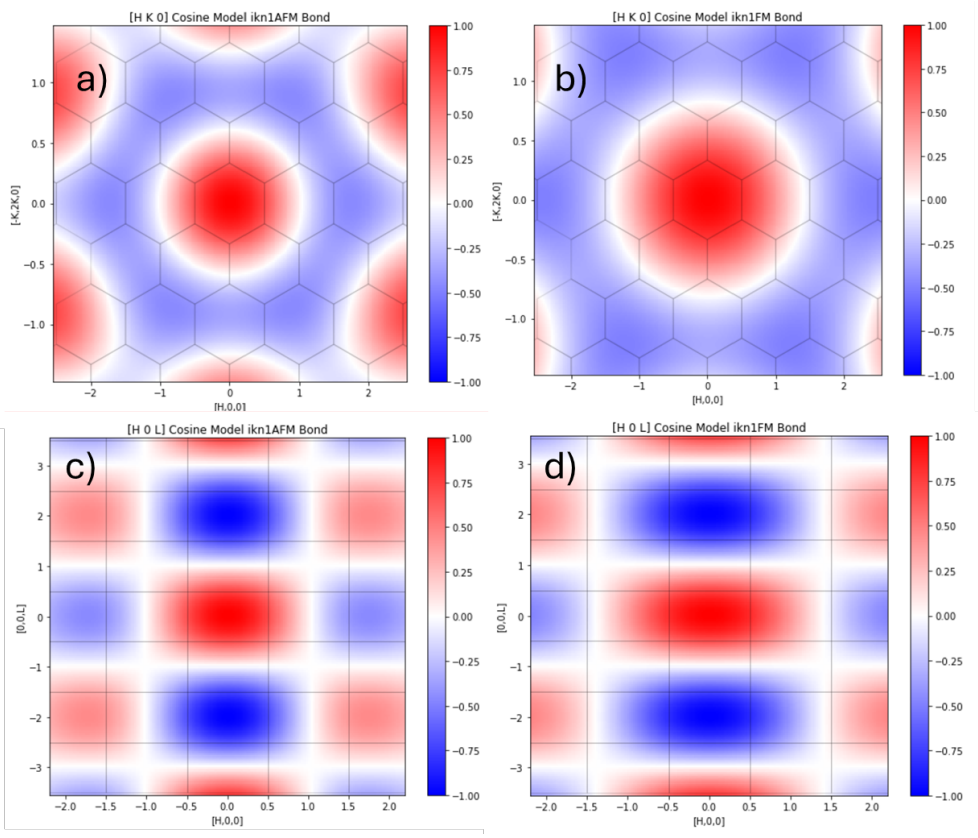

Figure 3.15: Figure illustrating the bond correlations that occur from the distorted interlayer impurity site: a), b), the in-plane HK0 scattering contributions of the FM and AFM distorted impurity bonds respectively. c), d), the out of plane H0L scattering contributions of the FM and AFM distorted impurity bonds respectively. Note that the distinction between these two bonds shows up a bit more clearly here due to the distinctly out of plane character of the impurity moments relative to the kagome lattice. Note that The real space AFM and FM bonds are detailed in Fig. 3.14

Fig. 3.15. Of note, the in-plane HK0 projections of $f_i(\mathbf{q})$ shown in 3.15 a) and b) are quite similar; the main difference is that the pattern is slightly contracted towards the center for the longer AFM bond in panel a), while the shorter FM bond is dilated outwards as shown in panel b). This follows rough expectations of any real to reciprocal space transformation, and you can also compare to the averaged middle ikn1 site as plotted in the lower left hand panel of Fig. 3.12 and see that the pattern sits qualitatively right between the two while maintaining a very similar shape.

With this, the problem thus becomes one of multi-colineraity. Whenever fitting any function to real data, similar fit qualities can often substitute one for another in a way that can be really difficult to separate out. For instance, say that you want to predict the price of a new house and include both square footage and number of bedrooms as separate variables. The relative weight of these two variables will be highly coupled when tuning between descriptive and plausible models since

these two variables are inherently strongly linked to one another. Hence, given the tiny distortion, the terms ikn1FM and ikn1AFM would have a relatively high degree of multi-colinearity with each other. Hence, even though fits suggested that the ikn1AFM bond was indeed antiferromagnetic, and the ikn1FM bond was indeed ferromagnetic, and that the FM correlation was stronger than the AFM correlation, we decided to leave this really interesting conclusion out of the nature paper because it was deemed to be too risky (although I will note that I disagreed with this assessment).

With this though, one strong way to reduce this multi-colinearity is to measure our system in a basis in which the difference between the $f_i(\mathbf{q})$ terms is more pronounced. Due to the out of plan nature of the impurity kagome bonds, the impurity $f_i(\mathbf{q})$ terms can be better distinguished in the H0L scattering plane, as is shown in Fig. 3.15 c) and d). Note that scattering in this geometry would also help us to measure any correlations between kagome layer planes that might be facilitated through the impurity magnetic moments; the HK0 scattering data would be completely insensitive to this kind of correlation. Note that to do this fitting, one does have to make a slight modification to Eq. 3.7. The parameter $\alpha(\omega)$ is a proxy for the overall scattering amplitude, which will generally change between scattering planes and incident energies, unless one manages to measure their neutron scattering in absolute units (which is a notoriously difficult problem [33]). The solution is to allow for two different α parameters, one for each plane, while constraining the ρ parameters to be the same. Since we're ultimately most interested in the evolution of bond correlations, this doesn't represent too major of a restriction.

We start by fitting to our lowest energy data that will be most sensitive to impurities and have the strongest signal: The [0.3,0.5] meV data. The resultant simultaneous fit to the HK0 and H0L data is shown in Fig. 3.16. I also first did this simultaneous fit with just the averaged ikn1 site for comparison (one less overall fitting parameter). Notably, the MSE improves by 15% with the inclusion of the distinguished impurity site bonds. The fitted values for ikn1FM and ikn1 AFM are 0.91 and -0.13, respectively. This can be compared to an ikn1 value of 0.73 when the simultaneous fit is done; notably, the difference between ikn1FM and inkn1AFM is 0.78, suggesting that ikn1 is indeed representing some average correlation of the two real bonds in the fitted data. Finally, I will note that the signs of all the other terms remains the same as the original fitting, although the amplitudes are modulated slightly due to the inclusion of the H0L scattering data. Finally, the addition of a layer to layer coupling term only improves the MSE by about 3%, while the fitted term itself is also weak with a value of only 0.1. This is great news for us, as it highly suggests that the impurity moments do not strongly interfere with the 2-D magnetism of the kagome layer moments. We exclude this contribution from subsequent analysis

This simultaneous fitting was repeated across energies, and the results are displayed in Fig. 3.17. Notably, the ikn1FM term is large and ferromagnetic and decreases with energy alongside all the other impurity terms. The ikn1AFM term, on the other hand remains small and antiferromagnetic throughout, suggesting a very weak direct exchange as was hypothesized earlier. Finally, all kagome

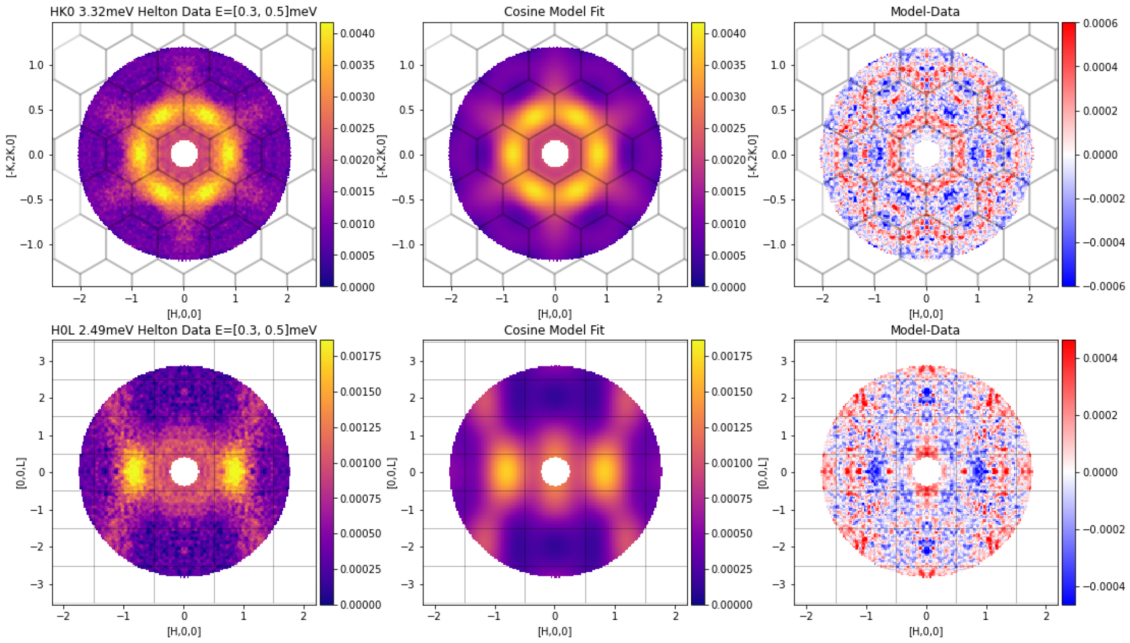

Figure 3.16: Simultaneous MSE fits to both H0L and HK0 scattering data in Zn-Barlowite. This fitted model includes the effects of the subtle Jahn-Teller distortion of the impurity moment.

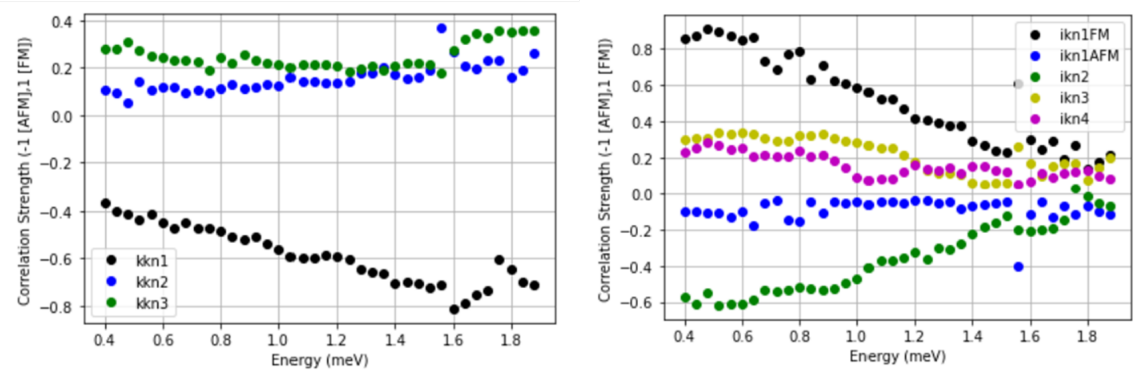

Figure 3.17: A plot of how the correlational parameters ρ_i evolve with energy in simultaneous fits to the H0L and HK0 data

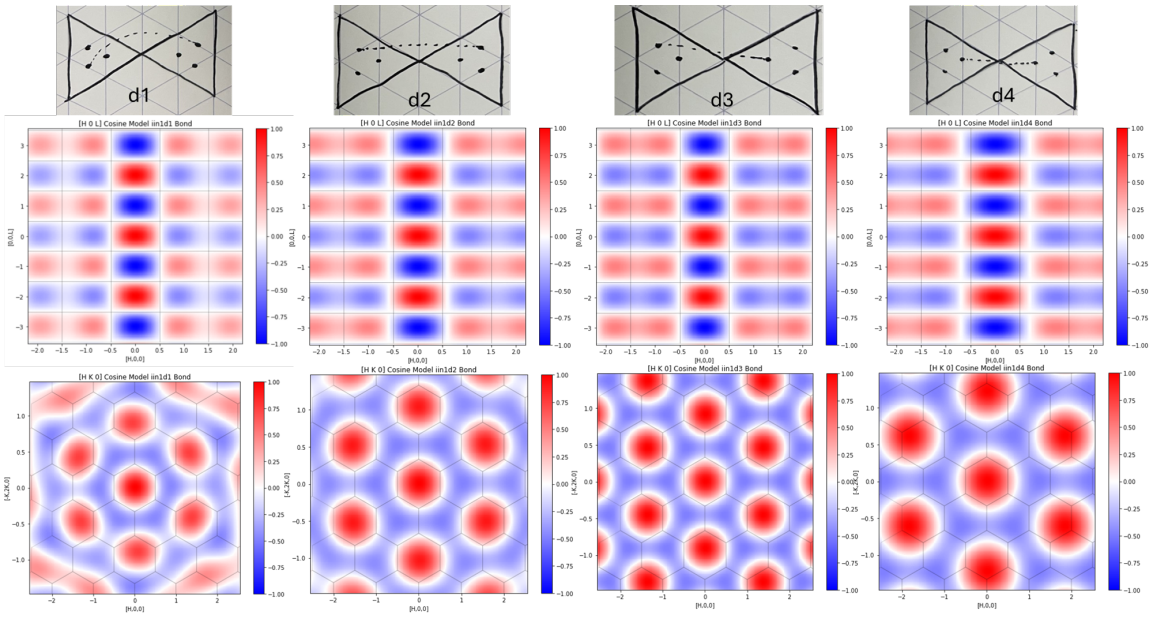

Figure 3.18: Figure showing the distorted $f_i(\mathbf{q})$ maps of the iin1 bonds, alongside the real space distortion that generates these mappings.

terms remain consistent in their signs and magnitudes with the original fits; the uptick in kkn1 magnitude with energy, in particular, is still replicated faithfully,

In summary, the H0L data combined with this distorted fitting refinement strongly suggest that the FM coupling between the impurity moment and the kagome layer is entirely confined to the kagome site which the impurity moment is Jahn-Teller distorted to. The H0L data also suggests that interlayer coupling is very weak, which is a very good sign for this material and its potential kagome layer QSL physics.

This distortion begs another obvious question; won't the other impurity bonds be affected by this distortion as well? The answer is of course yes! But as the impurity bonds get longer, the percentage of length that this distortion represents drops too. While around 10% for ikn1, this distortion is closer to 7% for iin1, and it only gets worse from here, and the multi-colinearity problem will only get worse. One interesting note about iin1 is that there are actually 4 possible (unique) distorted bonds since both sides are affected by the site distortion of the impurity. The different real space distortions alongside the corresponding $f_i(\mathbf{q})$ map is shown in Fig. 3.18.

The upshot of the analysis with respect to iin1 is that it seems likely that only one of these distorted bond types will be manifested in the real material. This is because neighboring impurities might affect each other through the kagome lattice. Hence, as a preliminary analysis, I just did the fit with the same parameter set as above, with ikn1AFM and ikn1FM distinguished, and with no direct inter-kagome-layer term. Then, I compared the results to see which bond was most likely to

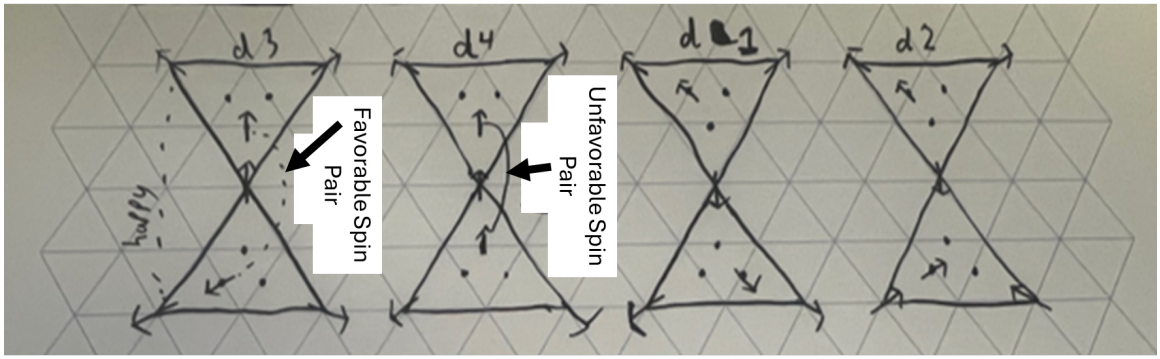

Figure 3.19: A classical ordering surrounding the potential bond distortions that is as consistent as possible with the Jahn-Teller distortion and the measured exchange correlations per our fitted model. Note that d4 seems to be impossible, while d1 and d3 satisfy the co-constraints quite well.

get manifested in this material. The results are tabulated in table 3.1

Table 3.1: Distorted Bond Performance Relative to Reference (iin1)

	iin1 (Ref)	iin1d1	iin1d2	iin1d3	iin1d4	iin1d1+d3
MSE	0.310	0.315	0.318	0.306	0.341	0.303
% Diff from Ref	0.00%	+1.61%	+2.58%	-1.29%	+10.00%	-2.26%
Correlation	-0.215	-0.253	-0.224	-0.230	-0.175	(0.129, -0.323)

Of note, the largest MSE change was for iin1d4. This bond corresponds to the neighboring impurities both being ferromagnetically coupled to the same kagome moment. Since the impurities tend to antiferromagnetically correlate with each other, it makes sense that this would be unfavorable; this distorted arrangement would make it impossible to satisfy all co-constraints. the only fit which saw an improved MSE relative to the centered baseline fit was the d3 distorted impurity to impurity bond. I have no strong intuition as to why this bond distortion would be favored relative to the others, but I do at least have a guess. In figure 3.19, I show a classical ordering surrounding all the potential bond distortions that is as consistent as possible with the Jahn-Teller distortion and the measured exchange correlations per our other parameters in our fitted model. In this, we see that d3 and d1 are able to do this quite well, while d4 fails spectacularly. d2 seems a bit more feasible, but the AFM exchange of the impurity-impurity bond is compromised a bit, and the same-sided-ness of the impurity bond does just seem intuitively wrong to me. I'd have to investigate further on the physics, but I think it would be related to how the impurities can distort the equilateral triangles as is shown in Smaha *et al* [1].

In this spirit, I suggest that the undistorted bond might fit well because the real system actually consists of a random combination of d1 and d3 type bonds. Doing this does indeed improve the MSE relative to the baseline by 2.3 % albiet with one additional fitting parameter. However, in this

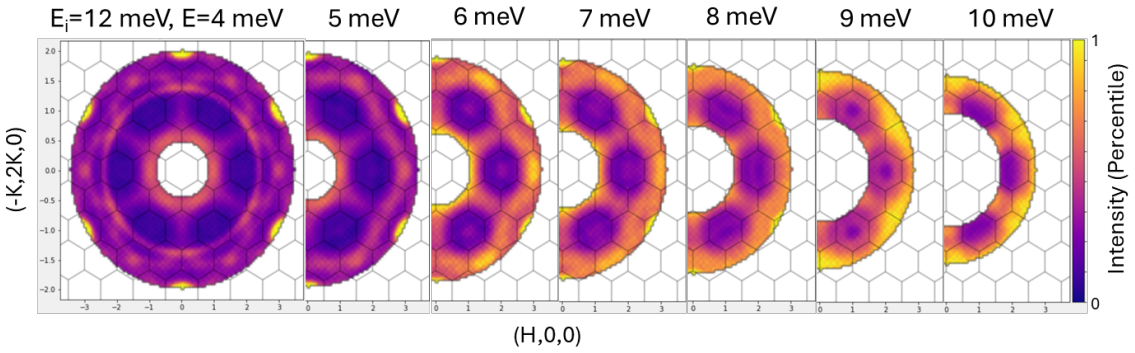

Figure 3.20: Scattering intensity vs momentum for $E_i = 12meV$ incident neutrons at varying inelastic energy transfers

modeling, iin1d1 prefers to be ferromagnetic while iin1d3 prefers to be more antiferromangetic to compensate. This seems less physically realistic to me. Further invertigation is clearly needed to fully determine what impurity-impurity distortions are present and to connect this with a physically feasible theory as to why this is the case.

This study on the out of plan H0L scattering data and the distorted fits is close to being publishable. The natural next step would be to quantify the multicolinearity between ikn1AFM and ikn1FM to see what kind of a range is reasonable as a compromise between these two parameters. Likewise, this multicolinerality analysis is going to be absolutely critical and might just help resolve the minor mystery of how distorted sites in Zn-Barlowite tend to line up when they are next to each other (iin1). Once these issues are resolved, I expect that this would be publishable to a standard journal like Physics Review B very soon.

3.7 High Energy Scattering

In addition to the out of plane H0L scattering data, we have also taken data with higher incident energy neutrons at CNCS. Specifically, data was taken at base temperature with incident neutron pulse energies of $E_i = 12meV$ and $E_i = 25meV$ in the HK0 scattering plane. Momentum resolved scattering maps are shown below in Figs. 3.20 and 3.21 respectively. In Addition to this, I have also collected data with $E_i = 25meV$ in the H0L scattering plane and this data is shown in Fig. 3.22

There are a few key challenges that make analysis of the higher energy data more difficult. The first is that we only took data at these higher energies at base temperature, due to the time constraints of beamtime that we had. This means that we cannot do the Helton background subtraction that was performed with the lower $E_i = 3.32meV$ data set. Note that if we were to go back and take higher temperature data to do Helton subtraction, we would need to be at a temperature such that $k_bT > E_i$. The reason for this is that the sample needs to have enough thermally populated

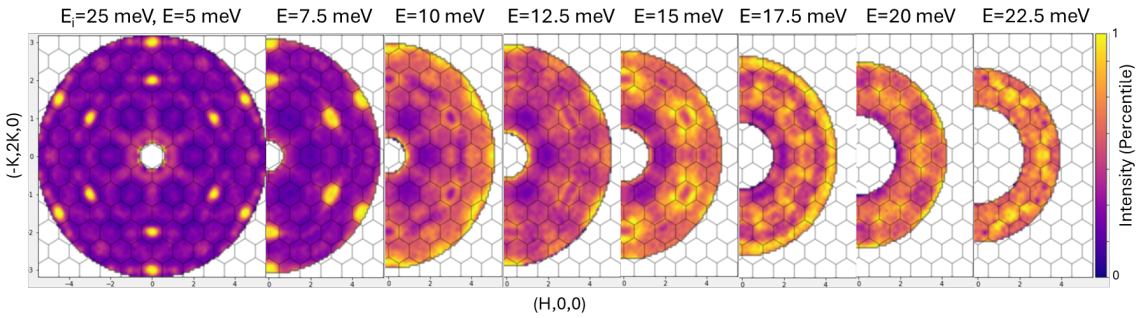

Figure 3.21: Scattering intensity vs momentum for $E_i = 25meV$ incident neutrons at varying inelastic energy transfers

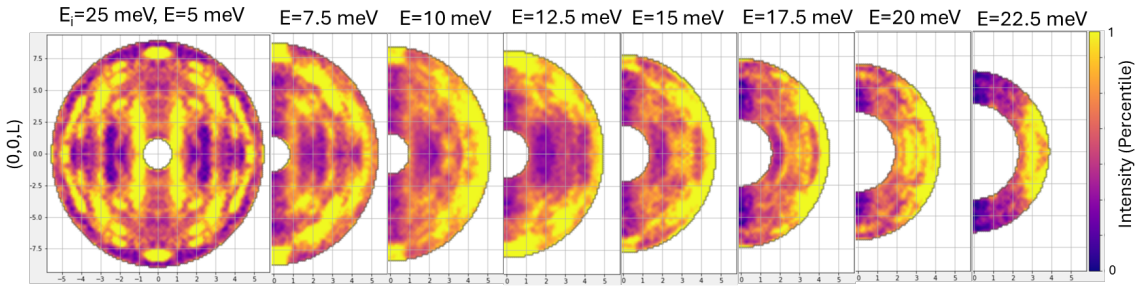

Figure 3.22: Scattering intensity vs momentum for $E_i = 25meV$ incident neutrons at varying inelastic energy transfers

magnetic modes such that they can transfer energy from the sample to the neutrons across the entire energy range studied, allowing the symmetry requirement of the Helton background subtraction to be fulfilled. This means a Helton balancing data set would need to be taken at or above $T = 140K$ to cover the full range of the $E_i = 12meV$ data set, and above $T = 290K$ for the $E_i = 25meV$ data set. The upshot is that the effects of the elastic Bragg peak bleed, as detailed in section 3.1 decreases with increased energy transfer, as there are simply less neutrons in the incident energy packet that are far enough away from the central energy to produce high energy artifacts. Additionally, the inelastic background from our CYTOP is less pronounced at higher energy transfers. Thankfully, one of the principle reasons we are interested in the higher energy data is precisely to look at higher energy dynamics where these issues are less pronounced anyways.

Another unique challenge of the high energy data sets is that at this incident energy, we are now within a range to activate Bragg and phonon sources that were silent at $E_i = 3.32meV$. One such source is incoherent elastic and inelastic scattering from the aluminum in the sample environment. This can be visibly seen in the $E = 4meV$ data in Fig. 3.20 as a powder ring, slightly above [H,0,0]=2.2 in q-space. Another consideration is that we are now activating phonon modes. We can visibly see the family of [2,2,0] phonons being populated on the outer rim of data in Fig. 3.20. Fig. 3.21 shows this phonon dispersing further with energy, branching considerably outwards in momentum. As the magnetic model in equation 3.7 doesn't account for phonons, this means that we cannot do a full magnetic modeling over all of the effective q-space here. Of course, one person's noise is another person's signal. Campello *et al* shows the evolution of the (0.5,0,4) phonon in Zn-Barlowite as contrasted to Barlowite II, and suggests that spinon-phonon coupling might be a key ingredient of this difference. Of course, we could also track the energy an momentum dependence of the phonons captured here in the higher energy data and attempt to connect this with spinon-phonon coupling as well, potentially even comparing to inelastic neutron scattering data taken on Barlowite II. This remains a promising open future direction of research.

As for analysis that we have actually completed on the high energy data, we started by doing the simplest possible thing, which was to restrict the q-range to include only data below both any phonons or aluminum rings. Note that this represents far less data that the $E_i = 3.32meV$ data set; even though the momentum bounds are similar, the momentum resolution is necessarily coarser, which is of course also the reason high energy data has an expanded high-q range. This analysis and fits are shown in Fig. 3.23. Of note, we did these fits with only 4 free fitting parameters; all three kagome terms, and ikn1, just the kagome to nearest interlayer impurity. This fitting confirms the general trend that kagome scattering continues to dominate as we go up in energy. All signs and magnitudes found were qualititively consistent with what we found in the lower energy data. Other than this, I will say that the qualitative patterns that are displayed at higher energies seem to be self consistent with kagome layer dominant scattering. This includes the hexagon feature in the 12 meV data, and the vertical rods at low-q in the H0L data.

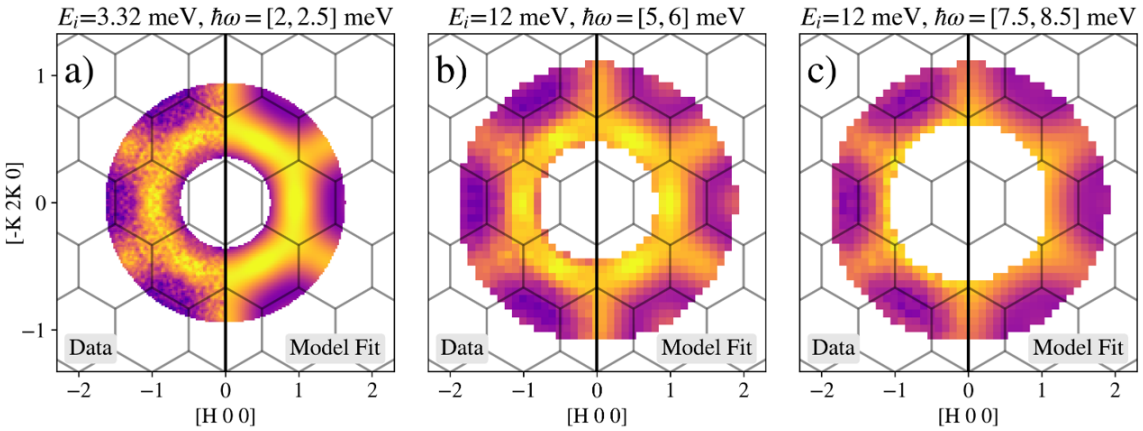

Figure 3.23: Cosine model fits to a few energy slices from the $E_i = 12meV$ data set

An obvious next step for this analysis is to be far more surgical with the q-range restrictions, such that we can fit more data. This seems straightforward enough for the 12meV incident data, which only has one known aluminum line and just the one phonon at high-q. For the 25meV data, more sophisticated phonon analysis might be required, particularly to examine any high-q magnetic features at high energies wherein the phonons have clearly dispersed considerably from their starting Bragg peak. It is not immediately clear here what regions of q should be excluded in an analysis of magnetic excitations across energies. In addition to this, it would also be instructive to plot the fitted parameters across energy as is done in Fig. 3.11 c)-e). After completion of this, I once again expect this could stand as its own independent Physical Review B kind of paper, and would make a great supplement to my nature paper [6].

In addition to this, there are more obvious pathways for high energy analysis that have yet to be explored. One promising result from Smaha *et al* is the measurement of a spinon scattering continuum all the way up to 200 meV using resonant inelastic x-ray scattering [34]. The energy resolution is rather coarse in RIXS at $\approx 30meV$, but the upshot of this is that we have measured a continuum of excitations in Zn-Barlowite from 0.3-200meV when combining with the CNCS data. That said, now that we have the large crystal array assembled and stationed at Oak Ridge, we could potentially measure inelastic neutron scattering in the 25-200 meV energy range with an instrument like SEQUOIA that is optimized for this. This should give us much finer energy resolution than the RIXS, while also providing more momentum information. The thesis presented in the RIXS paper [34] is that the high energy spinon scattering could be due to an exotic multi spinon scattering excitation. I hope that this demonstrates that there are plenty of exciting high energy data left to analyze and measure on the large Zn-Barlowite crystal array. These also plenty left to measure out of this special crystal growth. Perhaps even an entire PhD's worth :-).

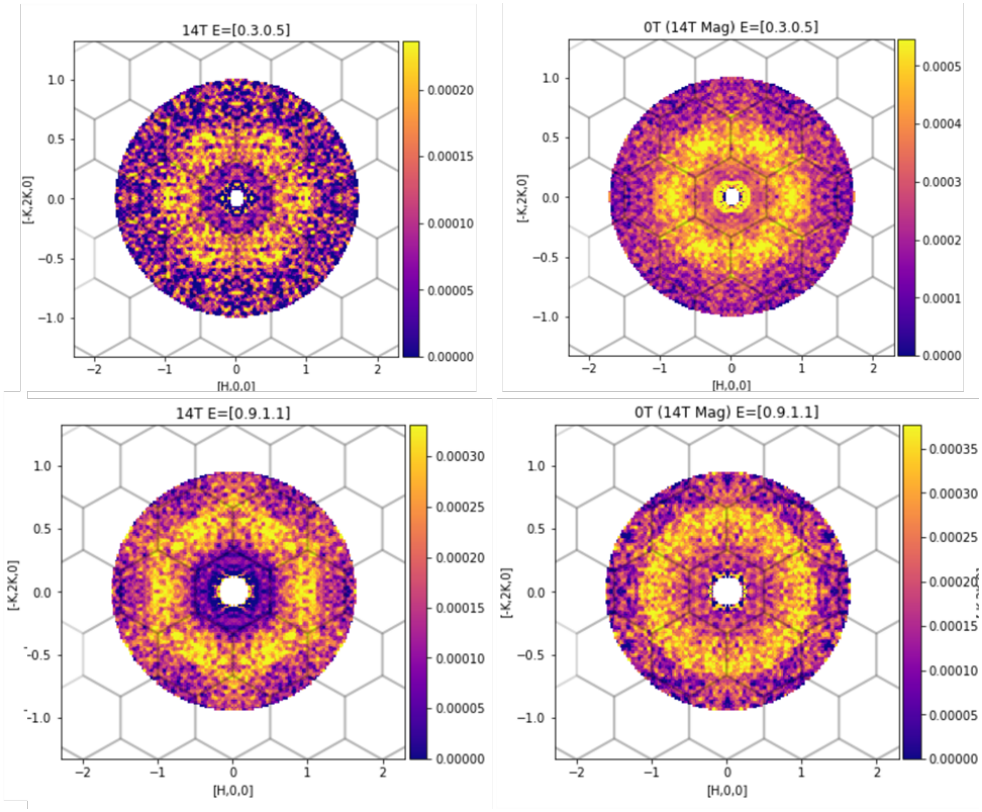

Figure 3.24: Inelastic neutron scattering energy slices taken at base temperature and $E_i = 3.32meV$ both with and without an applied magnetic field. The data is Hetlon subtracted and symmetrized. The 0T data presented is taken with the magnet in place such that that the data can be compared directly with the additional background from this source.

3.8 High Magnetic Field Experiments

The final set of inelastic neutron scattering measurements that were done were in a high applied magnetic field of 14T. As in Fig. 3.9, we show two representative energy slices for both impurity dominated low energy and kagome dominated high energy regimes in Fig. 3.24. Direct comparison of the 0T data in Fig. 3.24 to Fig. 3.9 shows that the patterns are similar enough, but that there is a large remaining background from having the magnet in the sample environment; it is unfortunate that the Helton procedure doesn't deal with this better. Part of the problem here is that having the magnet in place also reduces the effective flux that ends of reaching the detector by a factor of about 4. This is already apparent in the already comparatively bad statistics of Fig. 3.24.

There is still some amount of room for analysis though. One obvious trend is that the low energy data was affected much more by the magnetic field than the high energy data. This effect was expected; as we proved earlier, the low energy contribution is dominated by impurity scattering

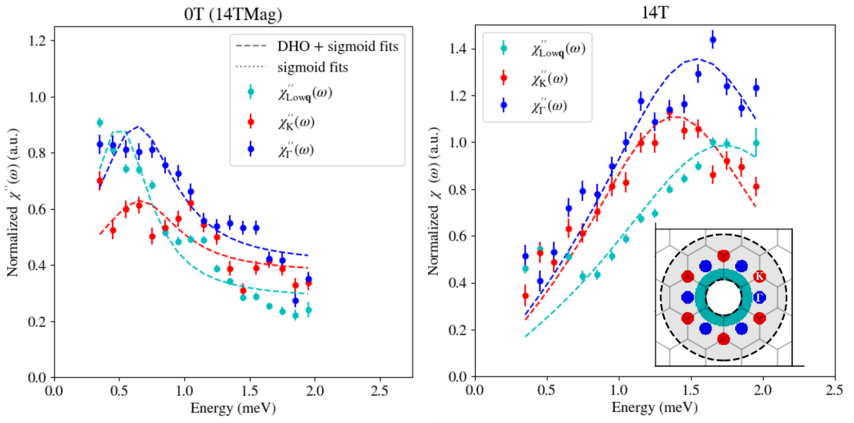

Figure 3.25: Cuts of reciprocal space plotted across energy both with and without an applied magnetic field.

which sits below the intrinsic kagome lattice QSL gap [31]. Hence, we would expect the Zeeman interaction to lift these modes in energy, leaving behind little scattering. This expectation was also supported by previous in field measurements of susceptibility [35, 1], thermal conductivity [36], and specific heat [37].

In Fig. 3.25, we show cuts in reciprocal space that are plotted across energy, analogous to what was done in Fig. 3.13. Here, the lower statistics stand out. The 0T data can't even be reliably fit with an energy gap term, as was done previously. However, the qualitative damped harmonic oscillator (DHO) trends are still loosely followed, and there still does seem to be a bump in scattering around 1 meV. So in short, everything is still self-consistent with the original data set.

In contrast, the 14T data clearly shows decreased scattering at low energy in absolute terms, further supporting the theory that the QSL is fundamentally gapped and that low energy scattering is dominated by impurities. The 14T data is still fittable as a DHO, but now the peak energy is shifted considerably higher in energy.

We can also model this energy shift in the DHO more directly. We model the dominant low-energy impurity response as a DHO with natural frequency ω_0 and damping Γ, whose imaginary susceptibility is

$$\chi''(\omega) \;=\; \chi_0 \,\frac{\Gamma\,\omega}{\left(\omega^2-\omega_0^2\right)^2+(\Gamma\,\omega)^2}. \tag{3.9}$$

For weak damping ($\Gamma \ll \omega_0$), the spectral maximum occurs near

$$\omega_{\mathrm{peak}} \;\simeq\; \sqrt{\omega_0^2-\frac{\Gamma^2}{2}} \;\approx\; \omega_0. \tag{3.10}$$

Effective two-level impurity and Zeeman term. Treat a localized impurity (or small impurity cluster) as an effective $S=\frac{1}{2}$ two-level system with a small zero-field splitting $\Delta_0=\hbar\omega_{\mathrm{imp}}$ that

encodes weak anisotropy/exchange. Applying a field B along $\hat{z}$ adds a Zeeman term $H_Z = g\mu_B B\, S_z$, where $g \approx 2$ and $\mu_B = 0.05788$ meV/T. If the zero-field splitting acts along an axis transverse to the field (e.g. $H_0 = \frac{1}{2}\Delta_0\, \sigma_x$), the full two-level Hamiltonian is

$$H = \frac{\Delta_0}{2}\,\sigma_x + \frac{g\mu_B B}{2}\,\sigma_z, \tag{3.11}$$

with eigenenergies $\pm\frac{1}{2}\Delta(B)$, where the level spacing is

$$\Delta(B) = \sqrt{\Delta_0^2 + \left(g\mu_B B\right)^2}. \tag{3.12}$$

Thus the impurity mode frequency entering Eq. (3.9) is

$$\omega_0(B) = \frac{\Delta(B)}{\hbar} = \sqrt{\omega_{\rm imp}^2 + \omega_Z^2}, \qquad \omega_Z = \frac{g\mu_B B}{\hbar}. \tag{3.13}$$

Equations (3.10)–(3.13) show that, for modest damping, the spectral peak of the impurity DHO shifts as

$$\omega_{\rm peak}(B) \;\approx\; \sqrt{\omega_{\rm imp}^2 + \omega_Z^2}, \tag{3.14}$$

i.e. the field imposes a Zeeman cost and transfers spectral weight from low ω to higher ω.

Numerics for the present experiment. With $g \approx 2$, $g\mu_B \approx 0.1158$ meV/T. Hence

$$E_Z = g\mu_B B \approx 0.1158 \text{ meV/T} \times B. \tag{3.15}$$

At $B = 14$ T,

$$E_Z \approx 1.62 \text{ meV}, \qquad \omega_Z = \frac{E_Z}{\hbar}. \tag{3.16}$$

For a small zero-field impurity scale ($\Delta_0 = \hbar\omega_{\rm imp} \lesssim 0.5$ meV) and moderate damping ($\Gamma \ll \omega_Z$), Eq. (3.13) gives

$$\hbar\omega_{\rm peak}(14 \text{ T}) \;\approx\; \sqrt{\Delta_0^2 + E_Z^2} \;\approx\; 1.4\text{–}1.7 \text{ meV}, \tag{3.17}$$

in quantitative agreement with the observed shift of the DHO (impurity) peak into the 1–2 meV range.

In contrast to the impurity channel, the kagome-plane response is expected to be only modestly perturbed by a 14 T out-of-plane field. With the dominant exchange in Zn–Barlowite estimated at $J \approx 14$ meV, the corresponding Zeeman energy

$$E_Z \approx g\mu_B B \approx 0.1158 \text{ meV/T} \times B \tag{3.18}$$

gives $E_Z \approx 1.6$ meV at $B = 14$ T, a small fraction of the exchange scale. I will assume a gapped

$\mathbb{Z}_2$ spin-liquid framework here since we have measured a gap in this experiment, and this is the leading gapped QSL model. In this model, the magnetic field couples to spinons via the Zeeman term, splitting the two spinon branches so that one gap decreases by $\approx E_Z$ while the other increases by the same amount. Since our measured spin gap is about 1 meV, this implies that the lower branch could in principle be driven close to gapless at $B = 14$ T. This would counteract the lifting of impurities, and add spectral weight back to lower energies. However, because the Zeeman shift is distributed across the continuum and the kagome correlations remain strongly frustrated, theoretical work shows that the $\mathbb{Z}_2$ state remains stable and does not immediately collapse into a polarized phase [38, 39]. The net effect for $E_Z \ll J$ is a modest redistribution of spectral weight near the continuum onset without closing the gap or destabilizing the deconfined spinon state. The observed resilience of the kagome continuum onset near 1 meV, in stark contrast to the large shift of the impurity DHO peak, is therefore consistent with the $\mathbb{Z}_2$ picture: the field efficiently polarizes weakly coupled impurities while leaving the intrinsic gapped spin liquid essentially intact, essentially due to it being much smaller than the kagome exchange energy. It is also worth noting here that having the magnetic field be out of plane probably further reduces coupling to the kagome lattice [1], which lends further credibility to this argument as to why the QSL gap isn't closed even though the magnetic field is on a comparable energy scale.

Cosine Modeling In Field The next obvious step for in-field analysis is to repeat the cosine modeling of equation 3.7 on this data set. Since the statistics are far lower here, the first thing that I will establish is that less is more. Fig. 3.26 shows the $E = 0.4meV$ and $E = 1.2meV$ data at 14T, alongside fits with two sets of fitting parameters: (1) just the leading kagome and impurity terms, ikn1 and kkn1, and (2) the full model, with all the terms used in Fig.. 3.11. Of note is that although the full model tends to look prettier, it performs worse in MSE in both cases. What this demonstrates is that the model still captures the scattering quite well in spite of the noise, and that the scattering is still dominated by the leading order terms. With this, we proceed to plot the model parameters across energy. We can start with a slightly reduced four term model, as shown in Fig. 3.27. The first thing to note is that the correlations at 0T with the magnet in place roughly follow the trends and magnitudes of the original 0T base temperature data set. However, due to the additional noise in the data, the fitted model parameters are also quite a bit noisier, particularly the higher order kkn2 and kkn3 terms, which now oscillate in sign around 0 semi-randomly; I strongly suspect that this is an artifact of overfitting to noise, rather than a real effect. This again motivates a more bare bones two parameter model model that is adopted in Fig. 3.28. Notably, the 0T data follows a more similar trend both with and without the magnet in place.

With this, the fits do provoke a bit of a mystery. The ikn1 impurity to nearest kagome correlation decreases more rapidly in the applied magnetic field. And yet a key expectation was that impurity scattering should be lifted in energy with the applied field.As we discussed earlier, one expects a maximum in the impurity response around $\hbar\omega_L \approx 1.6$ meV, but this isn't the case in the direct bond

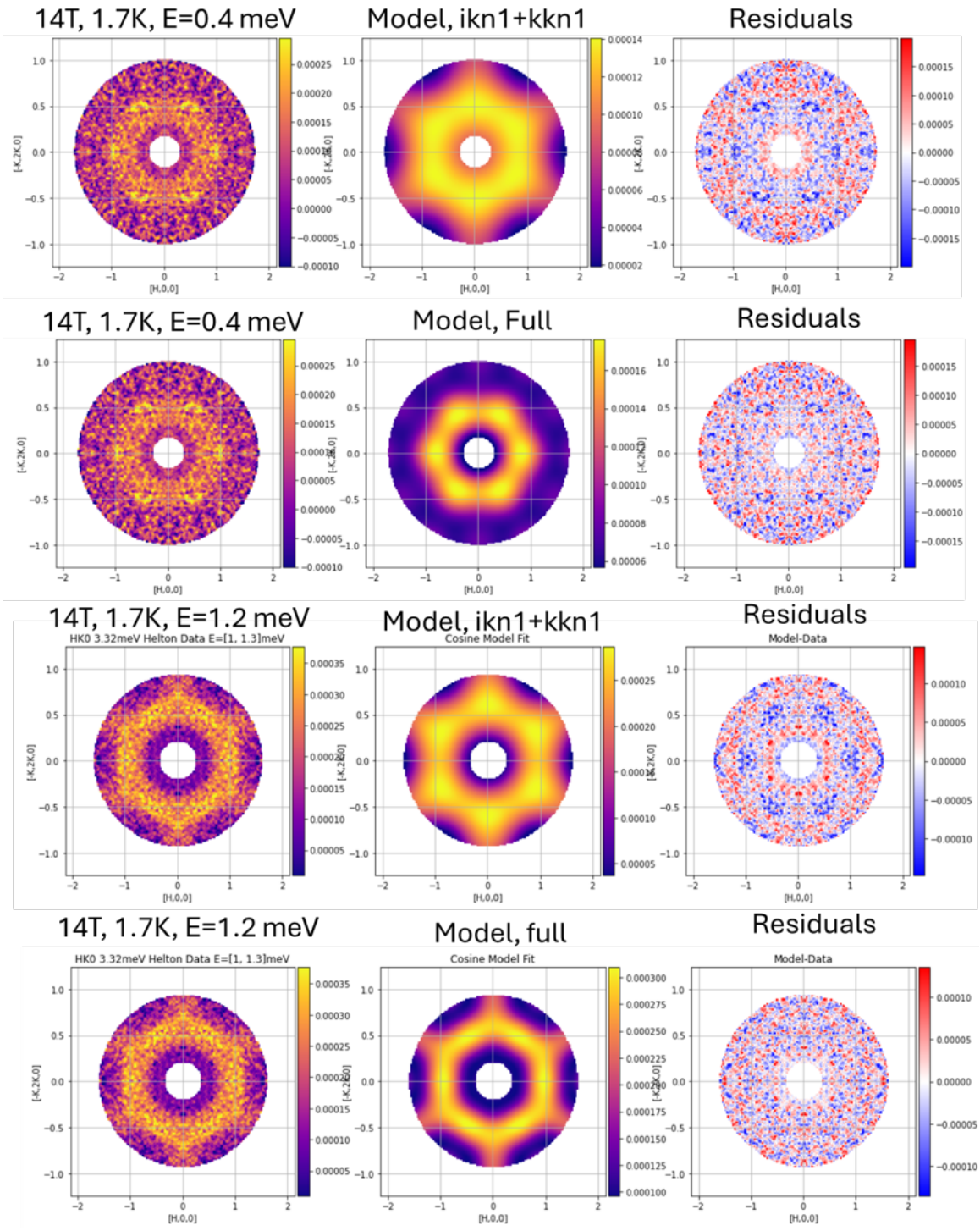

Figure 3.26: Two different cosine models fitted to the low energy (0.4 meV) and high energy (1.2 meV) data slices in an applied magnetic field of 14T

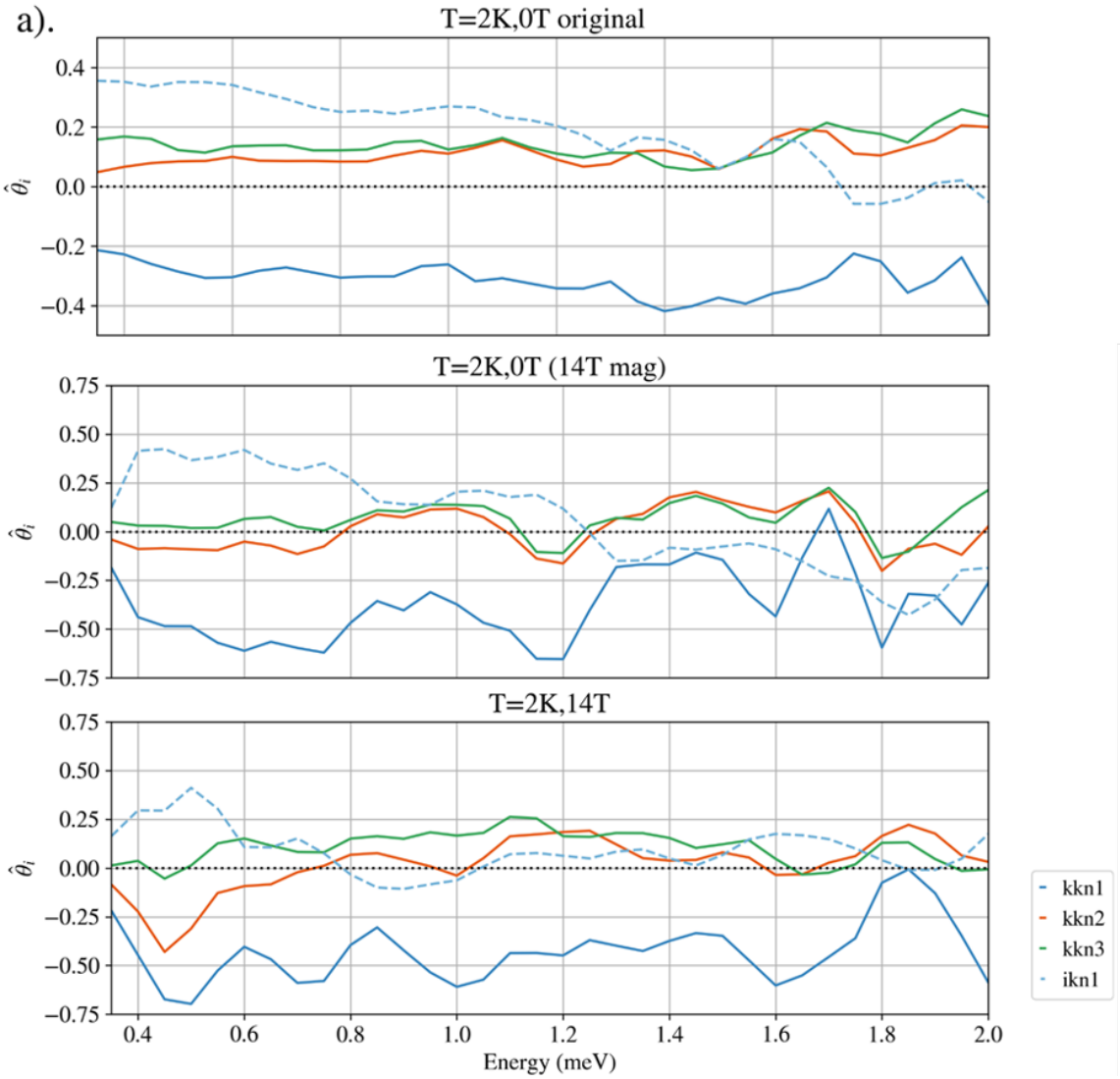

Figure 3.27: Evolution of fitted model parameters for a four parameter cosine model as a function of energy for the original data, 0T data with a magnet in place, and the 14T applied magnetic field data. The terms used in this model correspond to the bond decomposition outlined in Figs. 3.11 and 3.12

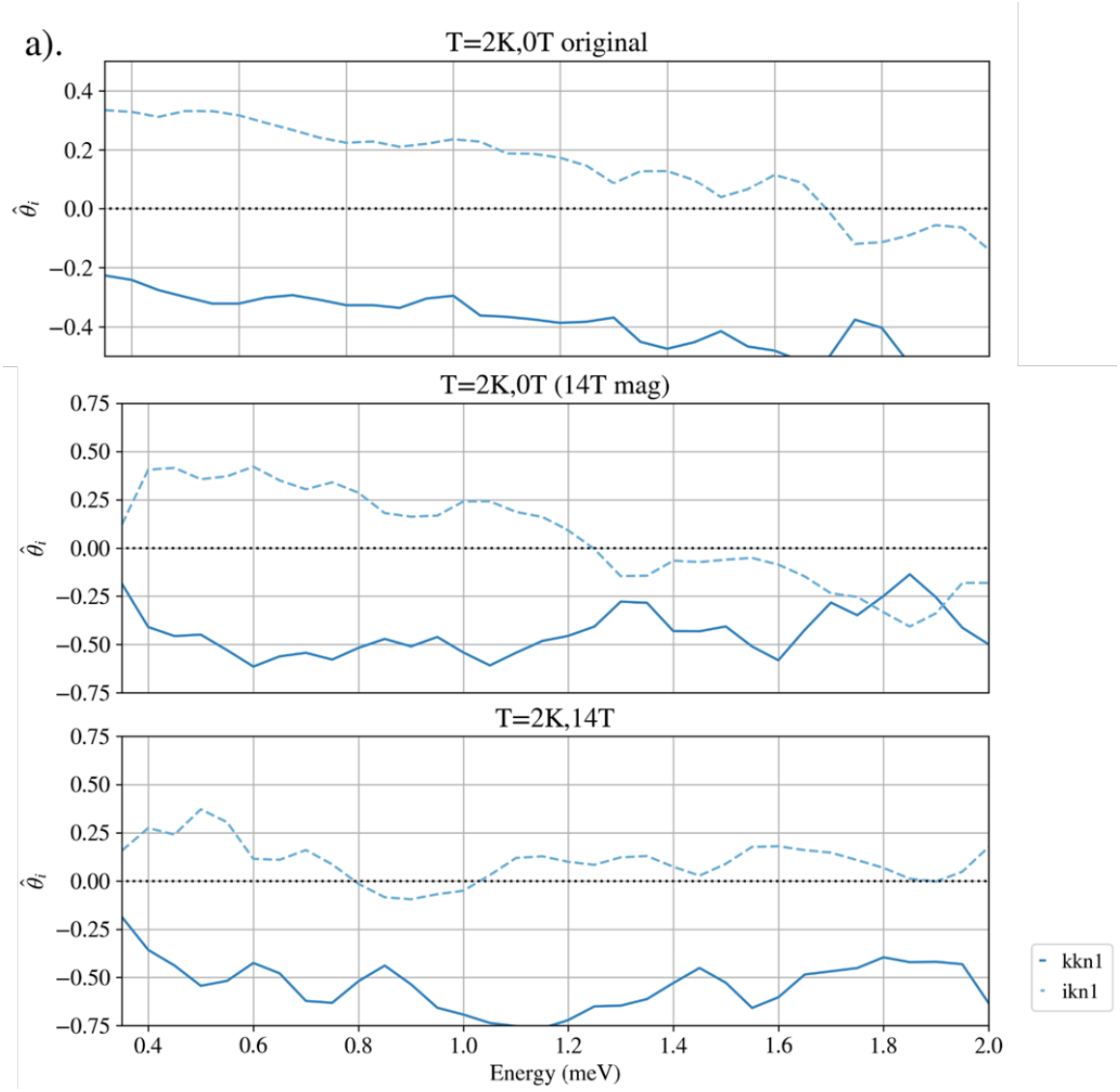

Figure 3.28: Evolution of fitted model parameters for a bare bones two parameter cosine model as a function of energy for the original data, 0T data with a magnet in place, and the 14T applied magnetic field data. The terms used in this model correspond to the bond decomposition outlined in Figs. 3.11 and 3.12. These two terms represent the shortest relevant bonds in this system, and the majority of the spectral weight at low energies.

correlation.

For *uncorrelated* impurities, the magnetic scattering is nearly local in real space, hence broad and featureless in the (H, K) plane, modulated mainly by the Cu form factor $|F(\mathbf{Q})|^2$ and the polarization factor

$$\mathcal{P}(\mathbf{Q}, \hat{\mathbf{M}}) = 1 - (\hat{\mathbf{Q}} \cdot \hat{\mathbf{M}})^2. \tag{3.19}$$

With $\hat{\mathbf{M}} \parallel \hat{z}$ and *in-plane* $\mathbf{Q}$ (our geometry), $\hat{\mathbf{Q}} \cdot \hat{\mathbf{M}} = 0$ so $\mathcal{P} \approx 1$: the intensity is *maximal* for in-plane $\mathbf{Q}$. Thus, at $\hbar\omega \approx 1.5$–1.7 meV one expects a broad, Γ-broadened, Γ-*centered* blob in the (H, K) map, weakly structured by whatever small real-space envelope the impurity wavefunction and site distribution impose. In the absence of inter-impurity correlations this yields rings that are close to Q-independent after ring-averaging.

Our cosine basis treats all spectral weight as sums over *pair* bonds. For dilute, nearly local impurities the dominant contribution is an *on-site/short-range auto term* that is not cleanly captured by any single bond coefficient; without an explicit constant (or narrow Gaussian around Γ) template, that weight can be distributed across multiple short bonds in a way that hides a peak in any one coefficient. Moreover, with in-plane data only, we cannot exploit the characteristic rod-like L-independence expected of local moments.

Practical augmentation (used or for future work). A minimal augmentation that resolves this tension is to add an explicit impurity auto template,

$$S_{\mathrm{mag}}(\mathbf{q}, \omega) \to |F(\mathbf{q})|^2 \left[\underbrace{\alpha_{\mathrm{imp}}(\omega)}_{\mathrm{q}\approx 0\,/\,\text{short-range, DHO at } \omega_0(B)} + \alpha_{\mathrm{kag}}(\omega) + 2 \sum_i \rho_i(\omega) f_i(\mathbf{q}) \right], \tag{3.20}$$

with $\alpha_{\mathrm{imp}}(\omega)$ modeled by Eq. (3.21):

$$\chi_i''(\omega; B) = \chi_0 \, \frac{\Gamma \, \omega}{\left(\omega^2 - \omega_0^2(B)\right)^2 + (\Gamma \, \omega)^2}. \tag{3.21}$$

In our geometry this term should exhibit a broad maximum at $\hbar\omega \approx 1.5$–1.7 meV and a corresponding depletion below $\sim$0.8 meV, while kagome-bond terms change only weakly near $\sim$1 meV. This might coincide with the raised DHO peak at around 1.6 meV. Further investigation with this uncoupled impurity model seems necessary to resolve the mysteries around what happens to the QSL state and the impurities in Zn-Barlowite in an applied magnetic field.

Direct Field Subtractions There is one more direction of future analysis on this data which I would be remiss if I did not mention. As can be seen in Fig. 3.29, the issue of the noise from the magnetic in the sample environment is greatly alleviated if one directly subtracts the 0 field and 14T data sets from each other.This cleanly shows how much scattering has left the low energy data in Fig.

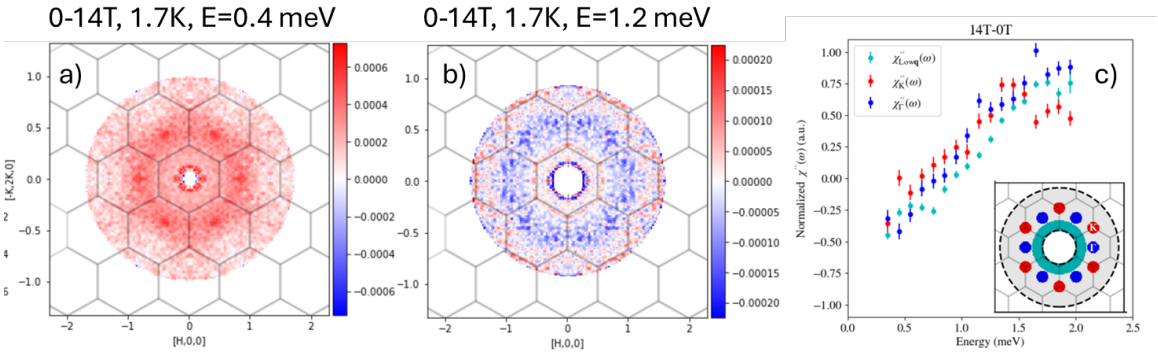

Figure 3.29: Direct subtraction of 14T data from the 0T data. (a), (b), energy slices at E=0.4 meV and E=1.2 meV, respectively. (c) q-cutes across energy for the field subtracted data

3.29 a). Meanwhile, panel b) shows that the higher energies have a more heterogeneous subtraction, meanining that the applied magnetic field seems to affect not only scattering magneitudes, but the q-dependence and specific bond correlations as well. Finally, panel c) is a very direct way of showing how the low energy spectral weight is shifted up in the applied magnetic field. Further analysis can and should be done to try to model the direct subtractions in panels a) and b). However, note that Eq. 3.7 is not a linear equation. Hence trying to model the co-evolution from this subtracted data set is more complicated than it might first appear. Yes, we don't have any noise, but the evolution of the fitting parameters is conflated, meaning that we can't disambiguate if the difference is a result of one correlation going up or another going down; as a compromise for eliminating noise, we are also eliminating unique information. One possibility to work this information back in would be to do some kind of a compromise; maybe we could start with a composite model with both fields disambiguated and seed with the weights fitted in Fig. 3.27. Then, we could let the weights softed into the direct subtracted data with minor perturbations. Unfortunately, I didn't finish exploring this before leaving my PhD.

Conclusion This subsection shows promising inelastic neutron scattering data in an applied magnetic field. The results seem consistent with the theory that low energy magnetic scattering is dominated by impurities, and that the contributions of these impurities are lifted in energy by the applied magnetic field via a Zeeman interaction. More analysis should be done to better resolve how this magnetic field affects the intrinsic QSL kagome lattice physics, but the early results indicate that they aren't perturbed much.

Additional work needs to be done in order to resolve the momentum dependence of the field shifts and perhaps deal with noise in a slightly better way. At the risk of sounding like a broken record, this too is also close to being publishable in a journal like physics review B. This is three articles in total that sit in a state of near completion: out of plane scattering and bond distortion,

high energy scattering, and in-field scattering. I pray that I can lead my successor to finish these projects in the Lee group, and that we can work together collaboratively. This is all great work, and it deserves to see the light of day.

Chapter 4

Natural Crystal Geophysics and Future Research

4.1 From Laboratory to Landscape: The Known Mineralogy of the Herbertsmithite and Barlowite Families

Herbertsmithite, $Cu_3Zn(OH)_6Cl_2$, is a rare copper-zinc hydroxide chloride mineral that forms under secondary hydrothermal conditions in the oxidized zones of copper ore deposits. While most studies of Herbertsmithite have focused on synthetic single crystals grown under carefully controlled laboratory conditions, it is important to recognize that this material also occurs — quite remarkably — in nature. Understanding its mineralogical context not only sheds light on its geological origins, but also raises new questions about how quantum materials might naturally emerge from geochemical processes operating over long time periods.

The mineral forms via the oxidation of primary copper sulfides (e.g., chalcopyrite) and zinc sulfides (e.g., sphalerite) in the presence of chloride-bearing fluids. These reactions occur under oxidative conditions, often associated with volcanic or hydrothermal activity, where acidic chloride-rich waters interact with Cu–Zn sulfide deposits. The result is a suite of secondary basic copper chlorides — including atacamite, clinoatacamite, paratacamite, and, at higher Zn concentrations, Herbertsmithite itself [40, 41].

The transition from the clinoatacamite/paratacamite structure to the rhombohedral Herbertsmithite phase occurs at roughly 25% Zn substitution on the Cu site. This substitution suppresses the Jahn–Teller distortion of the Cu^{2+} octahedra, stabilizing the trigonal $R\bar{3}m$ symmetry that characterizes Herbertsmithite and yields a nearly ideal kagome lattice of Cu^{2+} ions [42] Naturally occurring Herbertsmithite has been reported from several geographically and geochemically distinct localities. The type locality in the Los Tres Presidentes mine near Caracoles in northern Chile, is

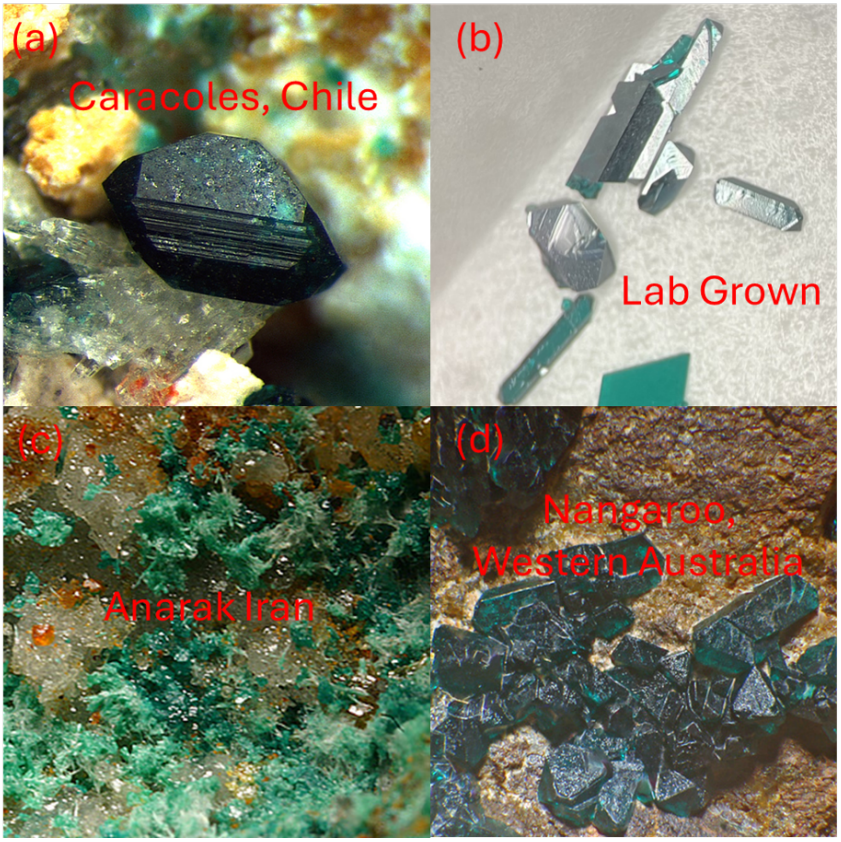

Figure 4.1: Naturally grown Herbertsmithite on a variety of different host matrices found in different locations. (a) from Caracoles Chiles on a quartzite matrix, (b) lab grown (test tube "matrix"), (c) Anarak Iran (Dolomite matrix), and (d) Nangaroo, Western Australia (unknown matrix, but possibly gossan rock). All photos, aside from panel (b) are courtesy of the midat.org mineral repository and database

particularly relevant for this work. Here, Herbertsmithite appears as dark green prismatic crystals on a pale buff quartzite matrix, reflecting formation within a silica-rich, oxidized environment characteristic of high-altitude porphyry copper systems [42]. As shown in Fig. 4.1(a), it forms morphologically into green gem like hexagons, much like the lab-grown Zn-Barlowite, and unlike the lab grown Herbertsmithite, which forms longer needles aligned along their (1,1,0) direction [2], as shown in Fig. 4.1(b). In contrast, Iranian Herbertsmithite samples from Anarak are found on dolomitic matrix, indicating that the conditions for stabilizing the rhombohedral phase may arise in carbonate-hosted systems as well. The morphology is notably different, as shown in 4.1(c). There is no published data on the matrix that the Zn-Barlowite grows on in Western Australia. However, by eye, the image in Fig. 4.1(d) in addition to reports on the related Ni-analogue material Gillardite, suggest that it grows on a Gossan iron rich rock matrix [**?**]. This figure also shows the natural crystals with the most similar morphology to that of lab-grown Herbertsmithite. This mineralogical diversity suggests a surprising robustness to the Zn-doped kagome motif and invites further geochemical study of phase stability across different host rocks and fluid regimes. Studying the magnetism of these different specimens of Herbertsmithtie may prove to be very fruitful. As was demonstrated by Smaha *et al* [21], Barlowite is very sensitive to small perturbations in growth conditions, and this leads to different magnetic ground states at low temperature. It seems feasible then, that these different natural specimen of Herbertsmithite might have different low temperature magnetic properties, based upon their natural synthesis pathways, especially given that they clearly display different bulk morphologies.

The possibility of a continuous Zn-substitution series between the magnetically ordered monoclinic phases and the disordered trigonal phase is especially tantalizing, especially as natural specimens seem to grow with a wide distribution of Zn^{2+} interlayer concentrations. Key open questions include: At what Zn concentration does long-range magnetic order vanish? Is there an intermediate spin-glass-like phase between classical magnetic order and full quantum spin liquid behavior? Do small differences in host mineralogy or crystal habitat correlate with distinct magnetic phases? These are not only materials science questions — they are also geological ones, demanding careful attention to natural phase assemblages and impurity chemistry. A systematic mapping of the Cu–Zn compositional phase space, especially using naturally formed specimens, could illuminate new transitions between classical and quantum regimes.

Along this vein of thought, I recently found one specimen of natural Herbertsmithite that is of particular interest for the quantum spin liquid problem. As has been explored throughout this thesis, one of the principal conflating variables in exploring kagome quantum spin liquid materials is the presence of Cu^{2+} impurities on the inter-kagome-layer sites. These impurities fill in the potential intrinsic kagome QSL gap at low energy with impurity scattering, in addition to muddying relative contributions at higher inelastic energy transfers [6]. To date, the highest purity Herbertsmithite grown still has about 15% Cu^{2+} occupation on the interlayer site [2], and about 13% for Zn-Barlowite

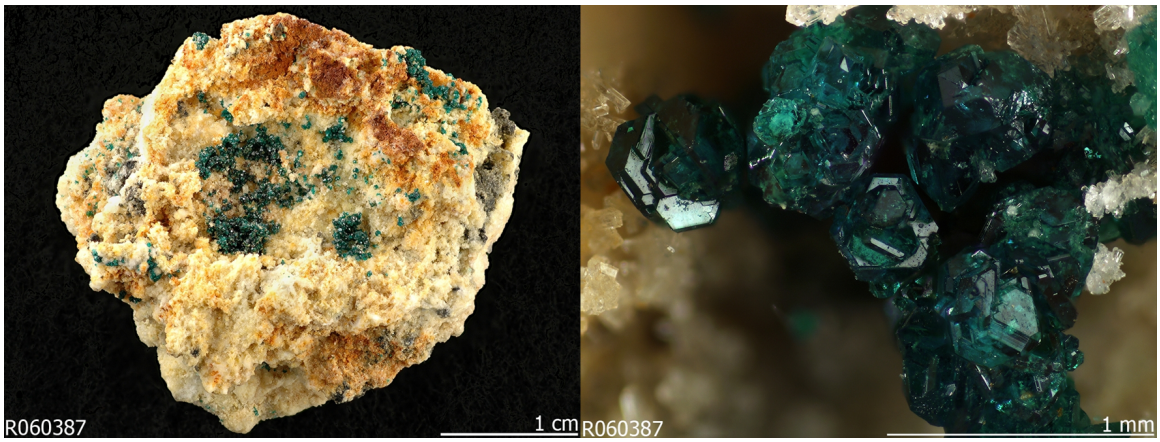

Figure 4.2: A sample of Herbertsmithite that was found by Michael Scott in the San Francisco mine of the Carracoles mining district in Chile. This specimen is likely to have very close to 100% interlayer occupancy of Zn, which would enable new scientific measurements.

[6]. In searching for information on natural specimens of Herbertsmithite, I found a description of one sample of Herbertsmithite with a Zn concentration of **102%** relative of the expectation for the stoichiometric compound [43]; this was verified with electron micro-probe analysis, which can reliable distinguish Copper from Zinc in these samples. This sample was discovered by Michael Scott in the San Francisco mine in the Caracoles mining district of Chile. A picture of this sample is shown below in Fig. 4.2

Given the typical 1% accuracy of such electron micro probe experiments determinations [44], this natural specimen is likely much closer to perfect stoichiometry than any synthetically grown crystal of this material. Intriguingly, this not only suggests a near 100% interlayer occupation of Zn; it also suggests that some Zn ions must find their way on to the kagome layer itself, since there would be no other feasible location for the excess zinc to fo. This hypothesis has been refuted by our group in our own synthetic samples, particularly through X-ray edge techniques (XANES) that can reliably distinguish Copper from Zinc due to resonant effects [45]. Other forms of anomalous x-ray diffraction also suggest that there is no mixing of Zn ions on to the kagome layer in *synthetic* samples with relatively low Zn concentrations [46].

However, other groups have found strong evidence for Zinc mixing onto the kagome layer using single crystal x-ray refinement *this year* [47]. Given that these materials show incredibly diversity in the face of minor fluctuations, I think that it is worth investigating this possibility further, especially in these high-Zn-concentration natural specimens. It remains distinctly possible that the natural samples have 100% interlayer Zn occupation in addition to some Zn ions mixing onto the kagome lattice. This is also a strong possibility for some synthetic samples as well. At the moment, this is an open question within QSL research.

I will add the caveat that electron micro-probe is a surface technique and can sometimes be

sensitive to surface layer coatings; I have gotten artificially high Zn-concentrations due to this effect before. However, when we obtain specimen of these samples, we can double check this by either doing a bulk technique like Inductively Coupled Plasma (ICP), or polishing the surface and re-doing the micro-probe. I will add that the original measurement measured more than 10 surface sites and got a similar Zn-concentration in all cases, so it is likely that the face-value measurement is correct, as surface contamination tends to be inhomogeneous in my experience.

If we trust the work done by our colleagues in geology at the University of Arizona, then this could be a groundbreaking specimen. If we learn more about its natural formation, we might unlock a key to higher Zn-purity synthetic growths. Perhaps the reaction pathway that leads to this supersaturation of Zn is different. Even if we can't replicate this, measuring this natural 100% Zn-interlayer sample could go a long way in ending the QSL debate once and for all. If the intrinsic kagome-QSL state is gapped, as we suspect, then we should get essentially no scattering below the gap energy of $\approx$1 meV in this ultra-pure sample. This would be much more direct evidence than the somewhat ambiguous low-energy impurity fits we did previously on Zn-Barlowite [6]. From Fig. 4.2, it seems that we at least have enough sample to do a powder inelastic neutron scattering measurement, which would be sufficient to directly prove the existence of this gap. I hope to further explore this mine as well, as obtaining more samples with this purity could allow us to to single crystal array measurements; even with this one sample, I suspect we're close to being able to do this. I am excited to explore this thread more in my postdoctoral studies.

In addition to Herbertsmithite, naturally occurring Barlowite, $Cu_4(OH)_6FBr$, has been identified from two localities. The type specimen described by Elliott et al. (2014) [**?**] was recovered from the Great Australia Mine near Cloncurry, Queensland, where Barlowite forms thin blue plate hexagonal crystals up to 0.5 mm in a cuprite–quartz–goethite matrix—a clear signature of supergene oxidation in a copper-rich environment [**?**]. Additional specimens reported from the Southwest Mine in Bisbee, Arizona, also show Barlowite in carbonate-hosted oxidized zones [48]. Notably, natural Zn-substituted Barlowite has not yet been documented, though given Zn's presence in many high-Copper deposits—and the coexistence of Zn-rich Herbertsmithite with it's Cu^{2+} analogues,—it remains an intriguing possibility. Furthermore, it is currently uncertain whether these natural specimens correspond to Barlowite I or II, as structural polymorphism has not been characterized in nature. In particular, this is because distinguishing these magnetic phases of Barlowite requires detailed low temperature crystallography or magnetometery, which has yet to be attempted on natural Barlowite.

That Herbertsmithite and Barlowite— materials of high interest for quantum information science — appear naturally in the Earth's crust is more than a novelty. It re-frames the mineral as not just a lab-grown artifact, but as a geologically emergent structure: one that may have formed slowly, quietly, and under conditions that mirror aspects of our synthetic techniques. I sincerely hope that I have provided sufficient evidence to demonstrate that natural grown Herbertsmithite and Barlowite

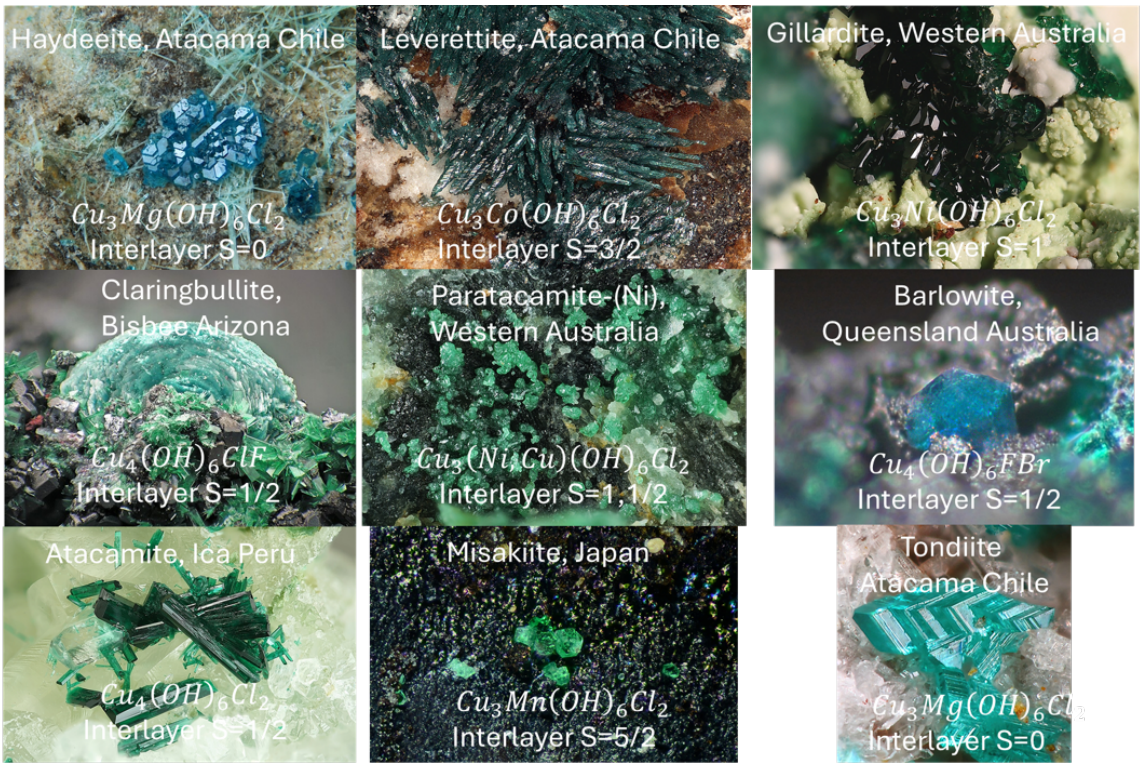

Figure 4.3: Photo showing other naturally occurring crystals in the Atacamite, Barlowite, and Claringbullite groups. Generally, all of these materials have a Cu^{2+} kagome lattice. They vary in their interlayer spacers, and I have labeled each mineral with the associated moment of the interlayer spin. All photos are courtesy of the midat.org mineral repository and database

is worth studying from a geological and physics perspective perspective. At the time of writing, I have a very limited amount of knowledge in geology, and my physics advisors have, unfortunately, not been supportive of research in this direction.

The presence of Herbertsmithite in the Atacama Desert — one of the most spiritually charged and volcanically active regions on Earth — sets the stage for the deeper inquiries that will follow in my postdoctoral research. What is perhaps the most shocking to me is that Herbertsmihtite has been found in the waste tailings of mines in the Atacama. This is shocking, and difficult to understate. Please see the appendix for more thoughts on how we ended up in such a strange and terrible predicament.

4.1.1 Other Natural Atacamite and Barlowite Group Specimen

It is a miracle of the natural world that we are blessed with a material as interesting and unique as Herbertsmithite. What is even more amazing is that there is an entire family of related materials

that also grows in nature, all of which represent minor perturbations from the Herbertsmithite system. I'm exciteed that all of these materials have been perfectly laid out next to each other in the Atacama Desert so I can tease out the fundamentals of exotic kagome magnetism. Several examples of natural specimen along with their type locality are shown in Fig. 4.3.

Generally speaking, these natural crystals are separated into two separate categories: The Kapellasite group and the Atacamite group. The Atacamite group has been described in detail throughout this thesis already. It generally consists of a pristine 2-D kagome lattice of spin $\frac{1}{2}$ Cu^{2+} ions which are separated from each other by a spacing interlayer. In contrast to this, in Kapellasite group materials, this cation situates itself in the center of the in-plane kagome hexagons, which produces a rather distorted kagome lattice and tends to alleviate frustration somewhat. The material stacks their kagome lattices directly on top of each other, with no spacing interlayer, which also tends to alleviate frustration due to higher direct inter-kagome layer coupling. For these reasons, polymorphs like Kapellasite are generally not quite as interesting to study for frustrated magnetism as Herbertsmithite group materials [49], although they remain unique magnetic materials in their own right.

In Herbertsmithite, this interlayer consists of halides and the non-magnetic Zn^{2+}, but this ionic site can generally be substituted with different ions that have a non-zero magnetic moment. In Atacamite, this interlayer spin is antiferromagnetically coupled to the kagome layer. This additional term alleviates frustration, and leads to magnetic order at about $T_N \approx 10K$. Further increasing this interlayer spin induces a transition into a spin-glass phase [**?**]. In figure 4.4, I plot the evolution of the Curie-Weiss fitting parameter and ordering temperature as a function of the interlayer spin size in these related materials [**?**, 50, 51]. Notably, the high-temperature Curie-Weiss fitting temperature monatomically decreases as the interlayer spin approaches 0 in Herbertsmithite. Notably, it would be interesting to see at what doping percentage between Zn and Cu (S=0-1/2) that our system transitions from a QSL to an ordered frustrated phase like in Atacamite. It would also be interesting to see at what percent Ni-doping that Atacamite transitions into a spin-glass phase (between S=1/2 and S=1). Finally, I will note that the S=5/2 relate material Misakiite has not been magnetically characterized yet. It will be interesting to see if it is also a spin-glass, and if it also continues the trend of increasing Curie-Weiss temperatures.

On more small note is that muon spin resonance measurements (μ-SR) on Tondiite (Mg-Herbertsmithite) indicate that a quasi-static magnetic state develops below 5K in which about one-third of the spins are frozen, while the remaining spins continue to fluctuate down to the lowest temperatures measured (20 mK). This implies a partial magnetic order superimposed on a highly frustrated background [52]. The authors suggest that intrinsic QSL physics is present here, although it seems like Zn-Barlowite and Herbertsmithite remain cleaner QSL candidates due to the decreased ferromagnetic interlayer coupling.

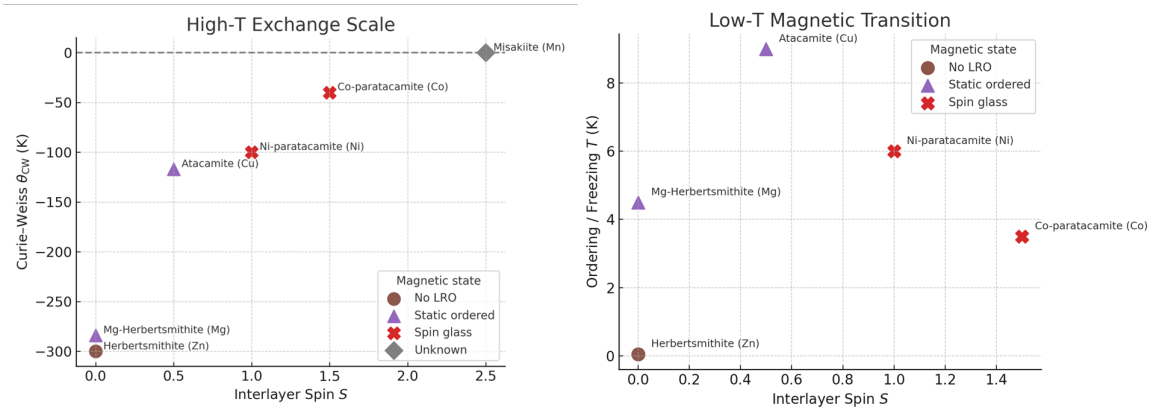

Figure 4.4: Plot of the Curie Weiss parameter (left) and magnetic ordering temperature (right) vs interlayer spin for related kagome materials.

4.1.2 The Mineralogy of Bisbee Arizona

I was fortunate enough to be able to have the personal resources to travel to Bisbee Arizona. While here, I spoke with Bisbee Minerology expert Doug Graeme. He wrote the 4 volume collection on the geology and mineralogy of Bisbee AZ [53] alongside his brother, Richard IV and father, Richard III. He was able to give me very helpful information with respect to his discovery of specimens of Atacamite, Claringbullite, Paratacamite, and Barlowite within the Copper Queen Mine in Bisbee AZ.

The Copper Queen mine is an incredibly magical place; during its heyday in the early 1900s, it was the most productive copper mine in Arizona. [54]. It was also famous for its particularly pure ore-bodies, which were as pure as 23% copper in some regions [55]. This ultra-pure ore consisted primarily of ore-grade malachite, azurite, cuprite and chrysocolla crystals; a sample piece of ore is pictured below in Fig. 4.5. The copper queen mine was famed for even including large deposits of 90% percent pure natural copper that often were the size of an entire room; this will precipitate out of the crystal-forming solutions when copper concentrations are high enough. Ironically, when the 1900's miners encountered such pure deposits, they left them in place [**?**]! The reason for this is that they could not tap into these deposits with their chisels and drills, nor could they blast it into chunks to transport on their rail-lines to the surface since natural copper is so ductile; hence, these deposits weren't profitable to extract, and would be mined around. In contrast to this, these natural copper deposits were often revered by early miners in the Atacama desert, especially before advanced smelting techniques were widespread [56].

In addition to its gorgeous blue ore bodies, the Copper Queen Mine also contained its fair share of extra-special nuggets. One of these was found by none-other than Doug Graeme of Bisbee Arizona. He details exploring the second floor of the Copper Queen Mine in 1987, a little over a decade since

Figure 4.5: A picture of a large specimen of Malachite and Azurite crystaline ore as was harvested from the Copper Queen Mine in Bisbee Arizona.

most copper mining operations around Bisbee had ceased [57]. While exploring, he came across a large boulder, which he said was about the size of a small-kitchen table. He told me that the boulder was out-gassing a lot of chlorine; it was incredibly smelly.

Doug told me that it oozed a deep blue liquid, similar to the color of our natural growth fluid when he cracked open the boulder. Unfortunately, Doug was not as an experienced of a mineral collector back then as he is today, and he did not collect any of the fluid to measure its ionic contents. In spite of this, it still ended up being one of the best discoveries of his career. He told me that over 30 unique crystal specimen were found within the unique and complex chemical environment of this boulder. These are tabulated below in Fig. 4.6. Of particular note for this study, this crystal contained large amnout of specimen from the atacamite group. In Fig. 4.7 below shows an image of *just the Atacamite group crystals* that were found within this boulder. This selection contains Atacamite, Paratacamite, and Clarignbullite.

Within this rock, there are two particular samples that I would like to highlight. The first is a sample containing the largest ever Atacamite I have ever seen. Using my thumb for scale, I think the central crystal is 1.5-2cm long. I forgot to take a formal measurement, but we can get in touch with Doug if we need to know the exact length or to more formally compare to lab specimen.

The second sample of note is an ultra-rare specimen of Claringbullite, Atacamite, and (possibly) Barlowite. This is pictured below in Fig. 4.9. Of note, the long green rods are Atacamite, and the thin blue wafers are Clarignbullite. I believe that the blue hexagonal gems are Barlowite, even Barlowite II given the morphology, color, and known details of the growth environment (other specimen also contained bromine). Notably, the Claringbullite wafers extend to up to 5×5 mm in size, which is far larger than any synthetic sample of Claringbullite I have ever found, which measure only about 1 mm in length for comparison. This could enable new experiments, especially in neutron scattering measurements, where large samples are essential given the characteristically

COMMON	RARE	VERY RARE
goethite	atacamite	claringbullite
hematite	paratacamite	paramelaconite
calcite	clinoatacamite	tolbachite
chrysocolla	connellite	graemite
malachite	bromargyrite	teineite
tenorite	chalcophyllite	nantokite
copper	buttgenbachite	likasite
brochantite	antlerite	botallackite
azurite	spangolite	ralstonite
	miersite	spertiniite
	minium	eugenite
	chalcoalumite	gerhardite
		bandylite

Table 9: Mineral species found in association with cuprite nodules

Figure 4.6: A table on the types of minerals found in Cuprate boulders around Bisbee AZ. Note that most of these specimen were found inside the single large boulder from Doug Graeme's 1987 discovery.

low scattering rates. Notably, the Clarignbullite and Barlowite minerals are secondary minerals, growing on top of the Atacamite which grows on top of the rock. It is especially cool to see how the Barlowite gems seem to stick themselves into the natural gem-like pockets of the natural curves in the geode.

With the natural crystals as inspiration, I have a proposal for an experimental growth that might result in larger synthetic crystals. We might consider seeding our hydrothermal growths by sticking some fully formed Barlowite, Atacamite, or Claringbullite samples at the cold end. We could even consider using natural crystals as the seed crystals, since they can be larger and are more abundantantly available than our lab-grown samples. Then, we could seed the rest of the hydrothermal growth as normal, with Zn-Barlowite, Herbertsmithite, or Zn-Claringbullite powder loaded into the "hot end". Hopefully, then, this powder would dissolve in the solution as normal, without dissolving our seed crystals. Then, we might expect the powder to naturally nucleate on the lattice sites of their sister materials, much like it does in nature. I feel this could work especially well in Zn-Barlowite on Barlowite growths, as the in-plane lattice constants of the kagome layer are identical to three significant figures [1]. Given natural crystals grow much larger in size in this way, I'm very excited to test this out to see if it would work!

4.1.3 Conclusion

I hope that I have demonstrated the value of searching for and measuring natural crystals in this chapter. These natural crystals have deeply inspired me to consider Barlowite and Atacamite analogs

Figure 4.7: A view of all the Atacamite group minerals from Doug Graeme's discovery of a large cuprite boulder in 1987. I will emphasize that all of these rocks and Atacamite crystals were found within the same boulder. Many other crystals were found as well. It was quite the find.

Figure 4.8: The largest Atacamite crystals in the bunch, some of which are greater than a centimeter in length.

Figure 4.9: A Sample of Mixed Claringbullite, Atacamite, and possibly Barlowite from Doug Graeme's collection.

with different interlayer spins, which might enlighten us with respect to how much frustrated kagome lattice magnetism is affected by the interlayer. I also have already located some record-sized crystals of frustrated kagome lattice materials in geology literature and archives, which may enable new measurements. Given I was able to accomplish this searching at abandoned copper mines on my own dime, one might imagine that I will continue to find new scientifically relevant natural specimen as I search for them in conjunction with institutional support and active local mining communities. Finally, I hope I have demonstrated that natural crystal growth occurs under rather different conditions than lab growths, and may very well hold clues with respect to how we can improve our synthetic growths.

The largest potential discovery is of course, the potential 100% Zn-interlayer occupied natural Herbertsmithite sample. I remember being viscerally mocked by my peers in physics for wanting to study natural crystals. Many said that they would assuredly be too "impure" to learn anything useful from. This is of course an anti-scientific worldview, which arrogantly and falsely assumes human superiority in all domains. It also clearly made assumptions about the natural world without any evidence to support them. It seems likely that the natural samples found in waste dumps in Chile are somehow more pure than the scientific specimens grown at Stanford. Perhaps these specimen will ultimately end the debate between the gapped-vs-un-gapped QSL issue. Perhaps these specimen will also contribute to increased scientific and epistemological purity at Stanford in a more general sense as well.

I conclude this thesis with a small prayer of hope and care. There is an important South American prophecy that seems apt here: the Prophecy of the Eagle and the Condor. In its telling, humanity split long ago into two paths. The Eagle took the masculine way of the mind—of reason, technology, and control. The Condor took the way of the heart—of intuition, spirituality, and connection to the earth. For centuries, the Eagle of the West has dominated and colonized, and the Condor of the global South has suffered. But the prophecy says that one day, in a new era, the Eagle and the Condor will fly together again.

I feel that my work with natural crystals in my postdoctoral studies is an answer to this call. My greatest hope is that this research will lead towards ecological restoration in the Atacama, and also help us to build the quantum computers of the future, leaping humanity into a new technological era. Maybe we can do it all. Maybe together, we can combine western wisdom with indigenous love. Maybe we can build higher performing computers without forgetting to give them good morals, so that they help out us and each other.

With love, hope, and care,

Dr. Shaman Aaron Thomas Breidenbach

Bibliography

[1] R. W. Smaha, W. He, J. M. Jiang, J. Wen, Y. F. Jiang, J. P. Sheckelton, C. J. Titus, S. G. Wang, Y. S. Chen, S. J. Teat, A. A. Aczel, Y. Zhao, G. Xu, J. W. Lynn, H. C. Jiang, and Y. S. Lee, "Materializing rival ground states in the barlowite family of kagome magnets: quantum spin liquid, spin ordered, and valence bond crystal states," *npj Quantum Materials*, vol. 5, no. 1, 2020. [Online]. Available: https://doi.org/10.1038/s41535-020-0222-8

[2] T.-H. Han, M. R. Norman, J.-J. Wen, J. A. Rodriguez-Rivera, J. S. Helton, C. Broholm, and Y. S. Lee, "Correlated impurities and intrinsic spin-liquid physics in the kagome material herbertsmithite," *Physical Review B*, vol. 94, no. 6, p. 060409, 2016.

[3] P. W. Anderson, "Resonating valence bonds: A new kind of insulator?" *Materials Research Bulletin*, vol. 8, no. 2, pp. 153–160, 2 1973.

[4] S. Jiang, A. C. Campello, W. He, J. Wen, D. M. Pajerowski, Y. S. Lee, and H.-C. Jiang, "Quantifying the Phase Diagram and Hamiltonian of S = 1/2 Kagome Antiferromagnets: Bridging Theory and Experiment," 2025, arXiv:2504.07387 [cond-mat.str-el]. [Online]. Available: https://arxiv.org/abs/2504.07387

[5] T. H. Han, J. S. Helton, S. Chu, D. G. Nocera, J. A. Rodriguez-Rivera, C. Broholm, and Y. S. Lee, "Fractionalized excitations in the spin-liquid state of a kagome-lattice antiferromagnet," *Nature 2012 492:7429*, vol. 492, no. 7429, pp. 406–410, 12 2012. [Online]. Available: https://www.nature.com/articles/nature11659

[6] A. T. Breidenbach, A. C. Campello, J. Wen, H.-C. Jiang, D. M. Pajerowski, R. W. Smaha, and Y. S. Lee, "Identifying Universal Spin Excitations in Spin-1/2 Kagome Quantum Spin Liquid Materials," 2025, arXiv:2504.06491 [cond-mat.str-el]. [Online]. Available: https://arxiv.org/abs/2504.06491

[7] W. He, "Scattering Studies of Magnetic and Charge Correlations in Two-Dimensional Quantum Magnets," Ph.D. dissertation, Stanford University, Stanford, California, 2024.

[8] M. R. Norman, "Colloquium: Herbertsmithite and the search for the quantum spin liquid," *Reviews of Modern Physics*, vol. 88, no. 4, 2016.

[9] L. B. Ioffe, M. V. Feigel'man, A. Ioselevich, D. Ivanov, M. Troyer, and G. Blatter, "Topologically Protected Quantum Bits Using Josephson Junction Arrays," *Nature*, vol. 415, pp. 503–506, 2002. [Online]. Available: https://doi.org/10.1038/415503a

[10] M. P. Shores, E. A. Nytko, B. M. Bartlett, and D. G. Nocera, "A structurally perfect S = 1/2 Kagomé antiferromagnet," *Journal of the American Chemical Society*, vol. 127, no. 39, pp. 13 462–13 463, 10 2005. [Online]. Available: http://pubs.acs.org.

[11] M. Fu, T. Imai, T. H. Han, and Y. S. Lee, "Evidence for a gapped spin-liquid ground state in a kagome Heisenberg antiferromagnet," *Science*, vol. 350, no. 6261, pp. 655–658, 11 2015. [Online]. Available: https://www.science.org

[12] T. H. Han, J. Singleton, and J. A. Schlueter, "Barlowite: A spin- 1 /2 antiferromagnet with a geometrically perfect kagome motif," *Physical Review Letters*, vol. 113, no. 22, 2014.

[13] H. O. Jeschke, F. Salvat-Pujol, E. Gati, N. H. Hoang, B. Wolf, M. Lang, J. A. Schlueter, and R. Valentí, "Barlowite as a canted antiferromagnet: Theory and experiment," *PHYSICAL REVIEW B*, vol. 92, p. 94417, 2015.

[14] D. Guterding, R. Valentí, and H. O. Jeschke, "Reduction of magnetic interlayer coupling in barlowite through isoelectronic substitution," *PHYSICAL REVIEW B*, vol. 94, p. 125136, 2016.

[15] Z. Liu, X. Zou, J.-W. Mei, and F. Liu, "Selectively doping barlowite for quantum spin liquid: A first-principles study," *RAPID COMMUNICATIONS PHYSICAL REVIEW B*, vol. 92, p. 220102, 2015.

[16] K. Tustain, G. J. Nilsen, C. Ritter, I. Da Silva, and L. Clark, "Nuclear and Magnetic Structures of the Frustrated Quantum Antiferromagnet Barlowite, $Cu_4(OH)_6FBr$," *Physical Review Materials*, vol. 2, p. 111405, 2018. [Online]. Available: https://doi.org/10.1103/PhysRevMaterials.2.111405

[17] J. H. Kim, S. Ji, S. H. Lee, B. Lake, T. Yildirim, H. Nojiri, H. Kikuchi, K. Habicht, Y. Qiu, and K. Kiefer, "External magnetic field effects on a distorted kagome antiferromagnet," *Physical Review Letters*, vol. 101, no. 10, p. 107201, 2008.

[18] S.-H. Lee, H. Kikuchi, Y. Qiu, B. Lake, Q. Huang, K. Habicht, and K. Kiefer, "Quantum Spin-Liquid States in the Two-Dimensional Kagome Antiferromagnets $Zn_xCu_{4-x}(OD)_6Cl_2$," *Nature Materials*, vol. 6, pp. 853–857, 2007. [Online]. Available: https://doi.org/10.1038/nmat1986

[19] S. Chu, P. Müller, D. G. Nocera, and Y. S. Lee, "Hydrothermal growth of single crystals of the quantum magnets: Clinoatacamite, paratacamite, and herbertsmithite," 2011. [Online]. Available: http://apl.aip.org/apl/copyright.jsp

[20] Z. Feng, Z. Li, X. Meng, W. Yi, Y. Wei, J. Zhang, Y.-C. Wang, W. Jiang, Z. Liu, S. Li, F. Liu, J. Luo, S. Li, G.-Q. Zheng, Z. Y. Meng, J.-W. Mei, and Y. Shi, "Gapped Spin-1/2 Spinon Excitations in a New Kagome Quantum Spin Liquid Compound $Cu_3Zn(OH)_6FBr$," *Chinese Physics Letters*, vol. 34, no. 7, p. 077502, July 2017. [Online]. Available: https://doi.org/10.1088/0256-307X/34/7/077502

[21] R. W. Smaha, W. He, M. J. Jiang, J. Wen, Y.-F. Jiang, J. P. Sheckelton, C. J. Titus, S. G. Wang, Y.-S. Chen, S. J. Teat, A. A. Aczel, Y. Zhao, G. Xu, J. W. Lynn, H.-C. Jiang, and Y. S. Lee, "Materializing Rival Ground States in the Barlowite Family of Kagome Magnets: Quantum Spin Liquid, Spin Ordered, and Valence Bond Crystal States," *npj Quantum Materials*, vol. 5, p. 23, 2020. [Online]. Available: https://doi.org/10.1038/s41535-020-0222-8

[22] G. Ehlers, A. A. Podlesnyak, J. L. Niedziela, E. B. Iverson, and P. E. Sokol, "The new cold neutron chopper spectrometer at the Spallation Neutron Source: Design and performance," *Review of Scientific Instruments*, vol. 82, no. 8, 8 2011. [Online]. Available: /aip/rsi/article/82/8/085108/354232/The-new-cold-neutron-chopper-spectrometer-at-the

[23] J. S. Helton, K. Matan, M. P. Shores, E. A. Nytko, B. M. Bartlett, Y. Yoshida, Y. Takano, A. Suslov, Y. Qiu, J. H. Chung, D. G. Nocera, and Y. S. Lee, "Spin dynamics of the spin-1/2 kagome lattice antiferromagnet $ZnCu_3(OH)_6Cl_2$," *Physical Review Letters*, vol. 98, no. 10, p. 107204, 2007. [Online]. Available: https://doi.org/10.1103/PhysRevLett.98.107204

[24] C. Broholm, R. J. Cava, S. A. Kivelson, D. G. Nocera, M. R. Norman, and T. Senthil, "Quantum spin liquids," *Science*, vol. 367, no. 6475, 1 2020. [Online]. Available: /doi/pdf/10.1126/science.aay0668?download=true

[25] L. Savary and L. Balents, "Quantum spin liquids: a review," *Reports on Progress in Physics*, vol. 80, no. 1, p. 016502, 11 2016. [Online]. Available: https://iopscience.iop.org/article/10.1088/0034-4885/80/1/016502https://iopscience.iop.org/article/10.1088/0034-4885/80/1/016502/meta

[26] A. Y. Kitaev, "Fault-tolerant quantum computation by anyons," *Annals of Physics*, vol. 303, no. 1, pp. 2–30, 1 2003. [Online]. Available: https://www.sciencedirect.com/science/article/abs/pii/S0003491602000180?utm_source=chatgpt.com

[27] S. Yan, D. A. Huse, and S. R. White, "Spin-liquid ground state of the S = 1/2 kagome heisenberg antiferromagnet," *Science*, vol. 332, no. 6034, pp. 1173–1176, 6 2011. [Online]. Available: https://www.science.org/doi/10.1126/science.1201080

[28] Y. C. He, M. P. Zaletel, M. Oshikawa, and F. Pollmann, "Signatures of Dirac cones in a DMRG study of the Kagome Heisenberg model," *Physical Review X*, vol. 7, no. 3, p. 031020, 7 2017. [Online]. Available: https://journals.aps.org/prx/abstract/10.1103/PhysRevX.7.031020

[29] R. Suttner, C. Platt, J. Reuther, and R. Thomale, "Renormalization group analysis of competing quantum phases in the $J_1 - J_2$ heisenberg model on the kagome lattice," *Physical Review B*, vol. 89, no. 2, p. 020408, 2014. [Online]. Available: https://doi.org/10.1103/PhysRevB.89.020408

[30] J. Wang, W. Yuan, P. M. Singer, R. W. Smaha, W. He, J. Wen, Y. S. Lee, and T. Imai, "Emergence of spin singlets with inhomogeneous gaps in the kagome lattice Heisenberg antiferromagnets Zn-barlowite and herbertsmithite," *Nature Physics*, vol. 17, no. 10, pp. 1109–1113, 10 2021. [Online]. Available: https://www.nature.com/articles/s41567-021-01310-3

[31] T. H. Han, M. R. Norman, J. J. Wen, J. A. Rodriguez-Rivera, J. S. Helton, C. Broholm, and Y. S. Lee, "Correlated impurities and intrinsic spin-liquid physics in the kagome material herbertsmithite," *Physical Review B*, vol. 94, no. 6, p. 060409, 8 2016. [Online]. Available: https://journals.aps.org/prb/abstract/10.1103/PhysRevB.94.060409

[32] J. Wang, W. Yuan, P. M. Singer, R. W. Smaha, W. He, J. Wen, Y. S. Lee, and T. Imai, "Freezing of the lattice in the kagome lattice heisenberg antiferromagnet ZnBarlowite $ZnCu_3(OD)_6FBr$," *Physical Review Letters*, vol. 128, no. 15, p. 157202, 2022. [Online]. Available: https://doi.org/10.1103/PhysRevLett.128.157202

[33] G. Xu, Z. Xu, and J. M. Tranquada, "Absolute cross-section normalization of magnetic neutron scattering data," *Review of Scientific Instruments*, vol. 84, no. 8, 5 2013. [Online]. Available: http://arxiv.org/abs/1305.5521http://dx.doi.org/10.1063/1.4818323

[34] R. W. Smaha, J. Pelliciari, I. Jarrige, V. Bisogni, A. T. Breidenbach, J. M. Jiang, J. Wen, H. C. Jiang, and Y. S. Lee, "High-energy spin excitations in the quantum spin liquid candidate Zn-substituted barlowite probed by resonant inelastic x-ray scattering," *Physical Review B*, vol. 107, no. 6, p. L060402, 2 2023. [Online]. Available: https://journals.aps.org/prb/abstract/10.1103/PhysRevB.107.L060402

[35] F. Bert, S. Nakamae, F. Ladieu, D. L'Hôte, P. Bonville, F. Duc, J. C. Trombe, and P. Mendels, "Low temperature magnetization of the $S = \frac{1}{2}$ kagome antiferromagnet $ZnCu_3(OH)_6Cl_2$," *Physical Review B*, vol. 76, no. 13, p. 132411, 2007. [Online]. Available: https://doi.org/10.1103/PhysRevB.76.132411

[36] Q. Barthélemy, E. Lefrançois, J. Baglo, P. Bourgeois-Hope, D. Chatterjee, P. Lefloïc, M. Velázquez, V. Balédent, B. Bernu, N. Doiron-Leyraud, F. Bert, P. Mendels, and L. Taillefer, "Heat conduction in herbertsmithite: Field dependence at the onset of the quantum spin

liquid regime," *Physical Review B*, vol. 107, no. 5, p. 054434, 2 2023. [Online]. Available: https://journals.aps.org/prb/abstract/10.1103/PhysRevB.107.054434

[37] J. S. Helton, K. Matan, M. P. Shores, E. A. Nytko, B. M. Bartlett, Y. Qiu, D. G. Nocera, and Y. S. Lee, "Dynamic scaling in the susceptibility of the $S = \frac{1}{2}$ kagome lattice antiferromagnet Herbertsmithite ($ZnCu_3(OH)_6Cl_2$)," *Physical Review Letters*, vol. 104, no. 14, p. 147201, 2010. [Online]. Available: https://doi.org/10.1103/PhysRevLett.104.147201

[38] J. W. Mei, J. Y. Chen, H. He, and X. G. Wen, "Gapped spin liquid with Z2 topological order for the kagome Heisenberg model," *Physical Review B*, vol. 95, no. 23, p. 235107, 6 2017. [Online]. Available: https://journals.aps.org/prb/abstract/10.1103/PhysRevB.95.235107

[39] T. Senthil and M. P. A. Fisher, "Z_2 gauge theory of electron fractionalization in strongly correlated systems," *Physical Review B*, vol. 62, no. 12, pp. 7850–7881, 2000. [Online]. Available: https://doi.org/10.1103/PhysRevB.62.7850

[40] Z. Bao, T. Al, J. Bain, H. K. Shrimpton, Y. Z. Finfrock, C. J. Ptacek, and D. W. Blowes, "Sphalerite weathering and controls on Zn and Cd migration in mine waste rock: An integrated study from the molecular scale to the field scale," *Geochimica et Cosmochimica Acta*, vol. 318, pp. 1–18, 11 2021.

[41] B. Cave, R. Lilly, and K. Barovich, "Textural and geochemical analysis of chalcopyrite, galena and sphalerite across the Mount Isa Cu to Pb-Zn transition: Implications for a zoned Cu-Pb-Zn system," *Ore Geology Reviews*, vol. 124, p. 103647, 9 2020. [Online]. Available: https://www.sciencedirect.com/science/article/pii/S0169136820301086?utm_source=chatgpt.com

[42] R. S. W. Braithwaite, K. Mereiter, W. H. Paar, and A. M. Clark, "Herbertsmithite, $Cu_3Zn(OH)_6Cl_2$, a new species, and the definition of paratacamite," *Mineralogical Magazine*, vol. 68, no. 3, pp. 527–539, 2004. [Online]. Available: https://doi.org/10.1180/0026461046830204

[43] "Herbertsmithite R060387 - RRUFF Database: Raman, X-ray, Infrared, and Chemistry." [Online]. Available: https://rruff.info/herbertsmithite/display=default/R060387

[44] X. Llovet, A. Moy, P. T. Pinard, and J. H. Fournelle, "Electron probe microanalysis: A review of recent developments and applications in materials science and engineering," *Progress in Materials Science*, vol. 116, no. January 2020, p. 100673, 2021. [Online]. Available: https://doi.org/10.1016/j.pmatsci.2020.100673

[45] R. W. Smaha, I. Boukahil, C. J. Titus, J. M. Jiang, J. P. Sheckelton, W. He, J. Wen, J. Vinson, S. G. Wang, Y.-S. Chen, S. J. Teat, T. P. Devereaux, C. Das Pemmaraju, and Y. S. Lee, "Site-specific structure at multiple length scales in kagome quantum spin liquid candidates," *PHYSICAL REVIEW MATERIALS*, vol. 4, no. 12, 12 2020.

[46] D. E. Freedman, T. H. Han, A. Prodi, P. Müller, Q. Z. Huang, Y. S. Chen, S. M. Webb, Y. S. Lee, T. M. McQueen, and D. G. Nocera, "Site-specific x-ray anomalous dispersion of the geometrically frustrated kagome magnet, herbertsmithite, $ZnCu_3(OH)_6Cl_2$," *Journal of the American Chemical Society*, vol. 132, no. 45, pp. 16 185–16 190, 2010. [Online]. Available: https://doi.org/10.1021/ja1070398

[47] R. K. Kremer, S. Bette, J. Nuss, and P. Puphal, "Chemo-structural disorder in the kagome spin $S = \frac{1}{2}$ systems $ZnCu_3(OH)_6Cl_2$ and $YCu_3(OH)_6Br_2[Br_x(OH)_{1-x}]$," *Physical Review B*, vol. 111, no. 2, p. 024424, 2025. [Online]. Available: https://doi.org/10.1103/PhysRevB.111.024424

[48] Mindat.org. (2025) Barlowite: $Cu_4fbr(oh)_6$. Accessed 13 Oct 2025. Southwest Mine, Bisbee, Cochise County, Arizona, USA. [Online]. Available: https://www.mindat.org/min-40276.html

[49] B. Bernu, C. Lhuillier, E. Kermarrec, F. Bert, P. Mendels, R. H. Colman, and A. S. Wills, "Exchange energies of kapellasite from high-temperature series analysis of the kagome lattice $J_1 - J_2 - J_d$ heisenberg model," *Physical Review B*, vol. 87, no. 15, p. 155107, 2013. [Online]. Available: https://doi.org/10.1103/PhysRevB.87.155107

[50] R. H. Colman, A. Sinclair, and A. S. Wills, "Magnetic and crystallographic studies of Mg-Herbertsmithite, γ-$Cu_3Mg(OH)_6Cl_2$: a new $S = \frac{1}{2}$ kagome magnet and candidate spin liquid," *Chemistry of Materials*, vol. 23, no. 7, pp. 1811–1817, 2011. [Online]. Available: https://doi.org/10.1021/cm103160q

[51] Y.-S. Li and Q.-M. Zhang, "Structure and magnetism of $S = \frac{1}{2}$ kagome antiferromagnets $NiCu_3(OH)_6Cl_2$ and $CoCu_3(OH)_6Cl_2$," 2011. [Online]. Available: https://arxiv.org/abs/1112.4117

[52] E. Kermarrec, P. Mendels, F. Bert, R. H. Colman, A. S. Wills, P. Strobel, P. Bonville, A. Hillier, and A. Amato, "Spin-liquid ground state in the frustrated kagome antiferromagnet $MgCu_3(OH)_6Cl_2$," *Physical Review B*, vol. 84, no. 10, p. 100401, 2011. [Online]. Available: https://doi.org/10.1103/PhysRevB.84.100401

[53] R. W. I. Graeme, D. L. Graeme, and R. W. I. Graeme, *The Mineralogy of Bisbee, Arizona: Volume 1 – Geology and Mineralogy.* Bisbee, Arizona, USA: Copper Czar Publishing, 2021, paperback edition, published August 4, 2021.

[54] W. H. W. Horace Jared Stevens, *The Copper handbook*, 1909, vol. 8. [Online]. Available: https://archive.org/details/copperhandbook02weedgoog/page/n7/mode/2up?utm_source=chatgpt.com

[55] PorterGeo Database. (2025) Warren mining district - bisbee, lavender pit, cochise, copper queen. Porter Geo International Ore Deposit Database. Accessed 13 Oct 2025. [Online]. Available: https://portergeo.com.au/database/mineinfo.php?mineid=mn742

[56] V. Figueroa, D. Salazar, H. Salinas, P. Núñez-Regueiro, and G. Manríquez, "Pre-hispanic mining ergology of northern chile: An archaeological perspective," *Chungara*, vol. 45, no. 1, pp. 61–81, 2013.

[57] Douglas Graeme, "Copper Queen Mine Tour." [Online]. Available: https://www.copperqueenmine.com/services-1